Microfabrication of thin-films: from stretchable radio-frequency electronics, biodegradable flexible electronics, to micro-structured scaffolds

By

Yei Hwan Jung

A dissertation submitted in partial fulfillment of

the requirements for the degree of

Doctor of Philosophy

(Electrical Engineering)

at the

UNIVERSITY OF WISCONSIN-MADISON

2017

Date of final oral examination: 08/22/2017

The dissertation is approved by the following members of the Final Oral Committee:

Zhenqiang (Jack) Ma, Professor, Electrical and Computer Engineering

Shaoqin (Sarah) Gong, Professor, Biomedical Engineering

Hongrui Jiang, Professor, Electrical and Computer Engineering

Zongfu Yu, Assistant Professor, Electrical and Computer Engineering

David M. Gamm, Associate Professor, Ophthalmology and Visual Sciences

Dedicated to my parents and my sister.

Acknowledgement

It is a sincere pleasure to express my deepest gratitude to my advisor, Professor Zhenqiang (Jack) Ma, who has supported and guided me throughout my predoctoral years. I am extremely grateful for his expertise, understanding, mentorship, and time he invested in me and my project. I would also like to thank my co-advisor, Professor Shaoqin (Sarah) Gong for insightful comments and guidance. Her creative advice and encouragements have clarified my research directions. I would like to thank all my committee members, Professors David M. Gamm, Hongrui Jiang, and Zongfu Yu, for the conversations and feedback on completing my degree.

To my advisors and mentors who inspired me through-out my time in undergraduate and graduate school, Professors John A. Rogers, Tae-il Kim, Dae-Hyeong Kim, Suk-Won Hwang, Hyun-Joong Chung, Young Min Song, Ki Jun Yu, Sung Hun Jin, Michael Bruchas, Dong-Wook Park, and Tae Wan Kim, and Drs. Rak-Hwan Kim, Hoon-Sik Kim, Bong Hoon Kim, Munho Kim, Minkyu Cho, and Jordan G. McCall, thank you so much for the abundant advice and feedback on my research, career goals, and life.

To all of the Ma lab members I met throughout my time in graduate school, with special thanks to Juhwan Lee, Huilong Zhang, Tong June Kim, Subin Lee, Sang June Cho, Hyungsoo Kim, Jihye Bong, Kwangeun Kim, and Tzu-Hsuan Chang, thank you for helping me mature through countless struggles and obstacles. It’s been a privilege working with you. I am also grateful to my fabulous colleagues at Waisman, especially Dr. M. Joseph Phillips. You have been by far the best collaborator I have ever worked with.

Thanks to all my friends and family who have helped me go through this journey. I must express my deepest gratitude to Chloe S. Kim, for her constant encouragement and enthusiasm, which were the driving forces of my studying period. Life in Madison could not have been better

without her. I would like to thank my MCN buddies, Lim, Heurk, Kihilm, Hyoon, Ilsuksam, Koork, Johnny, Won, Ddui, King kong, and Jemin, for being there for me and energizing me. Thanks to all my best buddies, Louis, Daeho, Jikyeong Lee, Heetae, Jung Il, Woochan, Jeongho, Mincheol, Seungjin, Ohyong, Johnathan, Stanley, Seungoh, Jiho, Yeonjun, Songwhi, Hanho, Suro, HT, and Mehdi, for the support and love.

I would like to thank the generous funding support of Howard Hughes Medical Institute for the prestigious predoctoral fellowship (grant number: 59108335). My doctoral research was also supported the following funding agencies: Air Force Office of Scientific Research/Air Force Research Lab (grant numbers: FA9550-08-1-0337, FA9550-09-1-0482, FA9550-11-C-0026 and AF10-BT14 II), Office of Naval Research (grant numbers: N00014-12-1-0884 , N00014-13-1-0226 and N00014-12-1-0077), Army Research Office (grant number: W911NF-09-1-0505), National Institute of Health (grant number: R01 HG000225) and Wisconsin Alumni Research Foundation. I appreciate their support for my research assistantships over the years.

Finally, and always, I am thankful for everything my mother, So Jin Kim, my father, Doo Suk Jung, and my little sister, Hye Soo Jung, have given me. I could not have done it without them.

Abstract

Thin films are layers of materials with thicknesses ranging from sub-nanometers to several micrometers. Like a mirror which is made using thin film silver coatings on glass or plastic to form reflective interface, thin films are widely incorporated in daily used products. In engineering, thin films are attractive because of their exceptional materials properties that are ideal for a wide range of applications. Thin films can also change the intrinsic properties of bulk materials. For instance, multiferroic materials and superlattices create two dimensional states and can form quantum confinement. At micro-scale, thin films are extremely difficult to handle because of the delicacy of the films that can easily break or tear apart with slight mechanical deformations. Therefore, microfabrication of thin films has long been a challenge in most fields. In this thesis report, conventional microfabrication techniques are modified to fabricate high-performance thin film electronics devices on flexible and stretchable substrate. Moreover, the techniques used for fabricating such devices are implemented to create thin film scaffolds that can benefit stem cell replacement therapy.

Thin film transistors used in printed electronics are often beneficial for applications where spatially arrayed format of devices is required or for flexible and stretchable electronics where devices can withstand deformations. They occupy less space, and their fabrication requires less materials, hence inexpensive. However, microfabrication of thin-film electronic devices was limited to materials with low-temperature processes, such as organic semiconductors and amorphous/polycrystalline inorganic films, which possess low intrinsic mobility and are only usable for certain low-speed applications. For typical electronics applications, single-crystalline inorganic semiconductors are utilized, owing to their excellent intrinsic properties that enable high-speed operations like digital computing and high-frequency operations like wireless

communication. Thus, flexible and stretchable electronics that need such advanced operations would require single-crystalline materials in thin film formats; however, such advanced materials are rigid in nature and are often manufactured in bulk wafers. Conventional microfabrication does not allow the processing of inorganic materials in thin film format due to many harsh conditions associated with the processes. Furthermore, the mechanical properties and processing conditions of other electronic components, such as the metal interconnects, inductors, and capacitors must match to those of active thin film electronic devices for the fabrication of fully functioning integrated circuit in thin formats. Numerous challenges arise especially for electronics that need high-frequency operation as the surrounding environment comes into effect as electromagnetic interference. Chapter 2 summarizes the challenges addressed and new strategies developed for fabricating high-frequency active and passive components on flexible or stretchable substrates, followed by reports on fabricating high-frequency stretchable transmission lines and flexible antenna on Chapters 3 and 4, respectively. These newly developed flexible and stretchable electronic components possess state-of-the-art performance and the combined efforts would lead to flexible and stretchable electronics capable of wireless communications using purely thin film components.

Thin film electronics are not only advantageous for creating flexible and stretchable electronics, but also for tremendously reducing the amount of inorganic materials used for electronics manufacture. Because the process involves the removal of the bulk semiconductor substrate, the substrate may be substituted with ecofriendly materials. The removed bulk semiconductor can be used for regrowth of active layers, which reduces the materials usage again. In Chapter 5, a complete set of novel materials, designs, and strategies for high-performance green electronics using modified microfabrication techniques and thin film components is reviewed,

followed by the demonstration of paper-based thin-film electronics with state-of-the-art performance in Chapter 6.

Thin films are also widely incorporated in biological devices as scaffolds or drug delivery films for minimally invasive transplant therapy or optimal control of drug delivery. Advances in biomaterials gave promising therapeutic options for many diseases that could not be cured with existing medical techniques. For instance, the development of hydrogels has paved the way for transplantable scaffolds with 3-D growth of cells and tissues. Development of dissolvable polymers has also played important role for delivering drugs and as substrates for bioresorbable medical electronics. While materials science in thin films has evolved immensely, manipulating the structures on such films for scaffolding has been limited as most manufacturing tools do not offer resolutions that are required for cell templates. Advanced fabrication tools that can pattern complex structures in micro-scale are generally incompatible with soft materials like elastomers and films. Nevertheless, following similar approaches to fabricate flexible and stretchable electronics with thin films, conventional microfabrication methods can be modified to allow incorporation of microstructures on soft materials. In chapter 7, a micro-structured scaffold that is manufactured using microfabrication technology is presented. Oriented growth of retinal stem cells that could not be achieved with existing scaffolds demonstrated in the chapter shows promising technology for fabricating scaffolds for various parts of the body.

Table of Contents

List of Figures

CHAPTER 1
Introduction

1.1. Towards high-speed wireless communication with flexible and stretchable electronics

The evolution of electronics from large industrial computers to light-weight portable devices has incredibly facilitated our daily pursuits and comforted our lives with multifunctional capabilities offered in lightweight, durable, and comfortable designs. Next generation designs of such electronics are leaning toward flexible and stretchable formats, which have already been successful in a wide variety of applications, such as medical devices, displays, solar cells, and biodegradable electronics [1-6]. A task left in transitioning such unusual format electronics into commercial products is to develop sophisticated wireless and high-speed communication systems in these ultrathin forms, which are crucial and often required for most applications. As an example, wireless capability in medical devices adds a great benefit of being able to monitor and treat remotely, eliminating threats to patients from tangled electrical wires and allowing cost-effective, continuous monitoring for medical practitioners. Since high-speed systems require electronic components with relatively high-performance, it is unavoidable to use hard inorganic semiconductors with exceptional intrinsic electrical properties.

Recent progress in flexible or stretchable electronics presents a route to creating high performance semiconductor electronics in forms that enable conformal contact to curvilinear surfaces, such as skin. Utilizing the fact that any material becomes flexible if it is thin enough, like a flexible sheet of paper made out of bulky wood, bending of high performance inorganic materials, such as silicon (Si), became realizable by thinning them down to the nanometer scale [7], thus called a nanomembrane (NM). Moreover, due to their excellent biocompatibility, many inorganic

materials can be used to make implantable electronics to cure and sense diseases [8]. To create such electronics, a new class of electronics manufacturing technique called the ‘transfer printing’ process is utilized, which transfers an exfoliated sheet of ultrathin inorganic material to a different substrate. This method enables placement of electronics on nearly any type of substrate, including but not limited to rubber, plastic, fabric, and glass [9]. The most appealing feature about this approach is that the majority of the manufacturing processes involves conventional fabrication technology, which already has a mature, established commercial infrastructure, thereby accelerating time towards commercialization and practical applications. This not only preserves the high-performance characteristics, but also makes the chip flexible or stretchable, depending on the material of the target substrate.

Introduction of such technology has already reshaped the rigid and conventional electronics into thin flexible devices that can stretch, bend, and twist seamlessly with the human body [10]. One of the promising applications of such electronics that could not be addressed with conventional technology includes advanced thin film biomedical devices, especially implantable and wearable medical electronics. As the ability to provide wireless powering or data transfer capabilities is highly desirable for many clinical applications, efforts have been made to overcome the challenges that constrain the development of implantable or wearable wireless electronics. Because high-performance components are generally required for radio frequency (RF) electronics that enable wireless transmission, challenges such as the difficulty of designing a RF circuit in a time dynamic media of organs and the limitation of high-temperature manufacturing processes required to fabricate high-performance devices have been solved using ‘transfer printing’ technology. These combined efforts of fabricating flexible active and passive RF components are presented in Chapter 2.

The materials and processes for fabricating high-performance stretchable electronics generally share similar schemes used for flexible electronics. Flexible electronics are easily transformed into stretchable electronics, as stretchable electronics are formed with a mesh of flexible thin film components interconnected with serpentine traces of metal on a rubber sheet like polydimethylsiloxane (PDMS) and Ecoflex®. These metal traces are stretched whereas the thin film devices are minimally affected by strain. Different from low frequency or direct current (DC) electronics, however, the dimensions of metal traces in microwave electronics must be carefully considered and treated as transmission lines to reduce RF loss. An effort to achieve such a stretchable transmission line is introduced in Chapter 3, which may be used to connect the microwave flexible components presented in Chapter 2 for circuit completion.

The last essential component of wireless circuitry is the antenna. Antennas for far-field wireless communication differ from those used for near-field systems in that they achieve longer ranges, where the working distance is much greater than the diameter of the device. Once the radiated RF energy from the transmitting antenna reaches the electronic devices, it must be received by the receiving antenna for powering. Among all other components for far-field systems, the antenna is the most difficult component to design as it is always application- and situation-specific due to the diverse types of surrounding media in the body. In wearable applications, the design criteria become less complex as the direction of the incoming electromagnetic (EM) waves do not have to go through any biological media, so any antenna in the flexible or stretchable format maybe suitable. Implantable antennas also follow similar rules, but are far more complicated in terms of its design. To make things even more challenging, the area for the antenna is extremely limited for implanted antennas. For instance, the thickness of the antenna must be kept ultrathin and confined in a small area for it to have no adverse effects on the surrounding tissues. While

designers have the choice to minimize the antenna size by increasing the operating frequency, the penetration depth of EM waves in biological tissues decreases with increasing frequency [11]. There are also restrictions on using certain frequency bands for bioelectronics, like the ISM bands set by the Federal Communications Commission (FCC), which poses another challenge for designers [12]. In Chapter 4, a simple and cost-effective design approach for fabricating WLAN frequency compatible flexible antenna for implantable application is presented.

1.2. High-performance green flexible electronics

Another major advantage of utilizing the 'transfer printing' technology into fabricating high-performance inorganic semiconductor thin film devices is the ability to re-use the growth substrate, which can solve significant environmental pollution from electronic-waste. Rapid technological advances and mass proliferation have shortened the lifetime of electronics and have led to faster electronic waste accumulation as users discard relatively new electronics that are only a couple of years old for even newer versions [13]. Since the fabrication processes have not changed much, the speed of accumulation will continue to increase if no changes are made at the manufacturing level. Sometimes, the electronic devices also contain large amounts of hazardous materials that are capable of seeping into the environment, causing damage that can cost millions of dollars to reverse. New materials and manufacturing processes to reduce the amount of accumulated e-waste by inventing so called 'green' electronics were proposed to minimize such a serious environmental threat [6, 14-16]. These combined efforts reduced the use of non-biodegradable plastics or toxic materials like lead, mercury, and arsenic that may be present in cases, batteries, electronic circuits, and displays. For electronic circuits, there have been efforts to replace the printed circuit boards (PCB), which provide support for the integrated circuits and electrical interconnects, with

biodegradable materials such as paper and organic boards [16]. Novel pure additive technologies to process such biodegradable PCBs, such as 3-D printing, inkjet printing, and screen printing, have been developed to eliminate any wet processes that might damage the biodegradable PCBs. These extensive efforts have contributed to saving the environment for future electronics; however, at the electronic chip (i.e., integrated circuit) level, conventional components wer still being utilized.

Although it is difficult to replace the conventional materials used to make electronic chips because they already have mature commercial infrastructures, many types of biodegradable semiconductors and substrates based on organic materials have been introduced to replace current wafer-based inorganic chips [14, 15, 17, 18]. However, for such new findings to be practical, the performances of new green electronic devices must be comparable to the state-of-the-art devices currently used in consumer electronics. Since most organic materials are biodegradable in nature, organic semiconductors have been printed on biodegradable substrates for potential green electronic chips. Proposed organic-based green electronics have shown promising and outstanding results suitable for many low speed and DC applications. However, for high-speed integrated circuits and microwave/RF applications, the low carrier mobilities of organic materials indicate their inadequacy in replacing conventional inorganic semiconductors, which are generally considered non-biodegradable [19].

It should be mentioned that in a conventional semiconductor chip, the active region comprises the very top thin layer, whereas the rest of the material on the bottom is merely a substrate that supports the active layer, typically comprising less than 1% of the entire semiconductor wafer [6, 20]. Novel techniques to shave off the top active layer from the wafer to transfer it to more ecofriendly and cost-effective foreign substrates have been progressively developed. This has

allowed bottom host wafers to be used for possible active layer re-growth. Furthermore, common semiconductor materials such as Si were found to dissolve, enabling fully degradable electronic chips. These combined efforts for fabricating such high-performance green electronic devices, are reviewed and discussed in Chapter 5. The fundamental inorganic materials, such as semiconductors, metals, and insulators, which together can form high-performance components, are also summarized. In addition, numerous types of green substrates suitable for integrating thin film semiconductor devices are reviewed. Finally, an introduction to high-performance green flexible electronics on biodegradable cellulose nanofibril paper is presented in Chapter 6, which demonstrates a full set of electronic components, including digital and analog circuits in an ecofriendly design.

1.3. Micro-structured thin film scaffolds

Polymer thin films made using synthetic materials are used to evaluate, treat, or replace any tissue or organs of the body and range widely in biomedical applications from tissue engineering to drug delivery [21]. Although various techniques to design and fabricate scaffolds with microstructures for cell replacement therapy have been introduced in the past, most were developed to produce randomized array or simple structures with relatively low resolution [22-24]. In microfabrication of electronics, desired patterns can precisely be structured on processing wafers via numerous types of etching techniques. This similar process can be combined with soft lithography which allows molding in nanoscale resolution to manufacture scaffolds with complex 3-D micro-structures [25]. Cell replacement therapy that requires specific alignment of cells, such as the photoreceptor cell, a type of cell that captures light inside the retina, would largely benefit from this thin film scaffolds with microstructures. Death of photoreceptor cells as a result of retinal

degenerative diseases is the leading cause of blindness and treatment options are highly limited as these cells do not regenerate. There are many retinal diseases and injuries that would benefit from cell replacements. Numerous studies have demonstrated that bolus injection of photoreceptor (PR) cells can partially restore vision in animals with retinal disease. Nevertheless, bolus injection of cells lacks organized delivery of cells due to random alignments of the photoreceptors upon injection. Because retina is a thin membrane consisting of sophisticated light detection system attached to the back of the inner eye, biocompatible scaffolds with ultrathin structure are only allowed for transplants to allow seamless contact with the curvilinear sub-retinal surface.

Latest developments such as the ultrathin implantable microfluidic neural systems are enabled by the development of unconventional techniques to create polymer-based complex structures in ultrathin format which can be implanted inside the body without adverse clinical effects [26]. In addition, materials science developments associated with biocompatible materials with stable mechanical properties that are suitable for long-term implantations have created a myriad of opportunities in the field. Nevertheless, combining such technology with stem cell research is in its early stage, especially in understanding or developing the human retinal systems. To better mimic native retinal tissues for investigating clinically translatable techniques, a uniquely designed polymer membrane is developed to study the growth behavior of photoreceptors. Using mixtures of reactive ion etch, precisely patterned microstructures are formed on the scaffold that can capture and guide photoreceptor cells to grow with perfect alignment, which is demonstrated in Chapter 7.

1.4. Reference

[1] D.-H. Kim, N. Lu, R. Ma, Y.-S. Kim, R.-H. Kim, S. Wang, *et al.*, "Epidermal Electronics," *Science*, vol. 333, pp. 838-843, Aug 2011.

[2] G. H. Gelinck, H. E. A. Huitema, E. Van Veenendaal, E. Cantatore, L. Schrijnemakers, J. B. P. H. Van der Putten, *et al.*, "Flexible active-matrix displays and shift registers based on solution-processed organic transistors," *Nature Materials*, vol. 3, pp. 106-110, Feb 2004.

[3] C. J. Brabec, N. S. Sariciftci, and J. C. Hummelen, "Plastic solar cells," *Advanced Functional Materials*, vol. 11, pp. 15-26, Feb 2001.

[4] D.-H. Kim, R. Ghaffari, N. Lu, and J. A. Rogers, "Flexible and Stretchable Electronics for Biointegrated Devices," *Annual Review of Biomedical Engineering, Vol 14*, vol. 14, pp. 113-128, 2012.

[5] T.-I. Kim, J. G. McCall, Y. H. Jung, X. Huang, E. R. Siuda, Y. Li, *et al.*, "Injectable, Cellular-Scale Optoelectronics with Applications for Wireless Optogenetics," *Science*, vol. 340, pp. 211-216, Apr 2013.

[6] Y. H. Jung, T.-H. Chang, H. Zhang, C.Yao, Q. Zheng, V. W. Yang, *et al.*, "High-performance green flexible electronics based on biodegradable cellulose nanofibril paper," *Nature Communications*, vol. 6, p. 7170, May 2015.

[7] J. A. Rogers, M. G. Lagally, and R. G. Nuzzo, "Synthesis, assembly and applications of semiconductor nanomembranes," *Nature*, vol. 477, pp. 45-53, Sep 2011.

[8] G. Park, H.-J. Chung, K. Kim, S. A. Lim, J. Kim, Y.-S. Kim, *et al.*, "Immunologic and tissue biocompatibility of flexible/stretchable electronics and optoelectronics," *Advanced Healthcare Materials*, vol. 3, pp. 515-25, Apr 2014.

[9] D.-Y. Khang, H. Jiang, Y. Huang, and J. A. Rogers, "A stretchable form of single-crystal silicon for high-performance electronics on rubber substrates," *Science*, vol. 311, pp. 208-212, Jan 2006.

[10] D.-H. Kim, J. Viventi, J. J. Amsden, J. Xiao, L. Vigeland, Y.-S. Kim, *et al.*, "Dissolvable

films of silk fibroin for ultrathin conformal bio-integrated electronics," *Nature Materials,* vol. 9, pp. 511-7, Jun 2010.

[11] H. Bizri, F. Toameh, W. Hassan, A. Hage-Diab, and L. Mustapha, "Simulation of RF biological tissues response towards remote sensing ECG device," in *Advances in Biomedical Engineering (ICABME), 2013 2nd International Conference on*, 2013, pp. 9-13.

[12] R. E. Fields, "Evaluating Compliance with FCC Guidelines for Human Exposure to Radiofrequency Electromagnetic Fields," 1997.

[13] R. Geyer and V. D. Blass, "The economics of cell phone reuse and recycling," *International Journal of Advanced Manufacturing Technology,* vol. 47, pp. 515-525, Mar 2010.

[14] M. Irimia-Vladu, E. D. Glowacki, G. Voss, S. Bauer, and N. S. Sariciftci, "Green and biodegradable electronics," *Materials Today,* vol. 15, pp. 340-346, Jul-Aug 2012.

[15] M. Irimia-Vladu, ""Green" electronics: biodegradable and biocompatible materials and devices for sustainable future," *Chemical Society Reviews,* vol. 43, pp. 588-610, 2014.

[16] J. Liu, C. Yang, H. Wu, Z. Lin, Z. Zhang, R. Wang, *et al.*, "Future paper based printed circuit boards for green electronics: fabrication and life cycle assessment," *Energy & Environmental Science,* vol. 7, pp. 3674-3682, Nov 2014.

[17] M. Irimia-Vladu, P. A. Troshin, M. Reisinger, L. Shmygleva, Y. Kanbur, G. Schwabegger, *et al.*, "Biocompatible and Biodegradable Materials for Organic Field-Effect Transistors," *Advanced Functional Materials,* vol. 20, pp. 4069-4076, Dec 8 2010.

[18] C. J. Bettinger and Z. Bao, "Organic Thin-Film Transistors Fabricated on Resorbable Biomaterial Substrates," *Advanced Materials,* vol. 22, p. 651, Feb 2010.

[19] K. Zhang, J.-H. Seo, W. Zhou, and Z. Ma, "Fast flexible electronics using transferrable

silicon nanomembranes," *Journal of Physics D-Applied Physics,* vol. 45, Apr 2012.

[20] J.-P. Colinge, *Silicon-on-Insulator Technology: Materials to VLSI*, 3rd ed.: Springer, 2004.

[21] V. K. Vendra, L. Wu, and S. Krishnan, "Polymer thin films for biomedical applications," *Nanotechnologies for the Life Sciences,* 2007.

[22] S. Shah, P. T. Yin, T. M. Uehara, S. T. D. Chueng, L. T. Yang, and K.-B. Lee, "Guiding Stem Cell Differentiation into Oligodendrocytes Using Graphene-Nanofiber Hybrid Scaffolds," *Advanced Materials,* vol. 26, pp. 3673-3680, Jun 2014.

[23] S.-W. Choi, J. Xie, and Y. Xia, "Chitosan-Based Inverse Opals: Three-Dimensional Scaffolds with Uniform Pore Structures for Cell Culture," *Advanced Materials,* vol. 21, p. 2997, Aug 2009.

[24] J. G. Torres-Rendon, T. Femmer, L. De Laporte, T. Tigges, K. Rahimi, F. Gremse, *et al.*, "Bioactive Gyroid Scaffolds Formed by Sacrificial Templating of Nanocellulose and Nanochitin Hydrogels as Instructive Platforms for Biomimetic Tissue Engineering," *Advanced Materials,* vol. 27, pp. 2989-2995, May 2015.

[25] S. Kim and M. Sitti, "Biologically inspired polymer microfibers with spatulate tips as repeatable fibrillar adhesives," *Applied Physics Letters,* vol. 89, Dec 2006.

[26] I. R. Minev, P. Musienko, A. Hirsch, Q. Barraud, N. Wenger, E. M. Moraud, *et al.*, "Electronic dura mater for long-term multimodal neural interfaces," *Science,* vol. 347, pp. 159-163, Jan 2015.

CHAPTER 2
High-speed flexible electronic active and passive devices

Electronic systems built on flexible plastic films and stretchable rubber sheets have attracted new applications in many emerging fields. Integration of high-speed electronics such as microwave power amplifiers and switches can extend the applications even further with wireless capabilities. As such, flexible and stretchable microwave electronics represent opportunities for future electronics where remote capabilities are desired. Here, advances in numerous types of microelectronic devices used for fast, flexible and stretchable electronic devices, as well as flexible and stretchable passive elements and circuitries are reviewed. Key components, such as the thin-film transistor, inductors and capacitors, are fabricated and analyzed as well.

2.1. Introduction

With near-field systems, powering a biomedical device via remote power transfer can be achieved by either inductive or capacitive coupling. Because near-field systems utilize non-radiative fields (magnetic fields in inductive components and electric fields in capacitive components), where the energy stays within a short distance of the transmitter, the fields will not be able to couple to the receiver if it is not within the range [1-3]. The range of the fields depends on the size and shape of the transmitter; moreover, the fields also decrease exponentially with distance. In applications that require wireless power transfer over a long distance, inductive or capacitive coupling mechanism cannot be utilized, as the coils must greatly exceed in size. Therefore, far-field systems that utilize radiative fields must be used. In order for the power to be

transmitted over a long distance, integrated circuits operating at microwave frequencies, together with far-field antenna, must be used for amplification and transmission. Difficulties and numerous challenges arise when trying to design a microwave circuit in an ultrathin format and also on or inside a time-dynamic media. There are two major challenges that must be overcome for the successful operation of far-field wireless systems. First, the environment must be composed of invariable, solid materials. The far-field wireless system is based on electromagnetic (EM) wave propagation, where the EM waves travel between two transceivers in a medium or many media to transfer electric power or data. Propagation of EM waves depends on the dielectric properties of the medium. Thus, RF engineers design wireless circuits with consideration of the dielectric properties of every surrounding material. Organs, tissues, and blood are dynamic and do not have fixed material properties; instead, it varies by conditions such as temperature and age. Therefore, this proposes a primary design challenge in making a biomedical device with wireless system. Second, wireless systems must operate at high power since the far-field transmitted power decreases rapidly with increasing distance. In a radio frequency (RF) system, highly performing active and passive devices, such as transistors, diodes, capacitors, and inductors are needed to operate at a certain allowed frequency like the Industrial Scientific Medical (ISM) bands. Nevertheless, fabrication of high-performance devices is especially challenging on biocompatible polymers, due to the constraints in using high-temperature processes generally required for fabricating high-performance electronics. Finally, all the individual key components (active devices, passive devices, and antennas) required for building the wireless system must be combined carefully in order to transmit wireless signals efficiently. To effectively transmit and receive signals over a long distance, a microwave power amplifier is necessary at the transmitting end in order to amplify the power to compensate for energy loss over the long distance. At the

receiving end, a microwave rectifier is typically connected to the receiving antenna to convert the incoming high-frequency alternating signal into direct currents. On either side, individual components such as the transistor, diode, capacitor and inductor, must be able to perform at relatively high, yet allowed frequencies.

2.2. High-speed active devices

New materials and processes to create high-speed electronic devices and circuits using thin-film materials have developed continuously to enable microwave applications such as wireless communication for flexible and stretchable electronics [4, 5]. Building the ultrathin radio-frequency (RF) active components requires advanced engineering and careful design procedures, since they must impose specific requirements: (i) possess high carrier mobility, (ii) integrable on foreign substrates, and (iii) mechanically flexible with minimum performance changes [6]. In addition, there are requirements to build microwave integrated circuits, such as amplifiers and switches, which are (1) high power/unit width for compact and ease of matching, (2) high voltage operation for reduction in step down, (3) high linearity for optimum band allocation, (4) high frequency for large band width, (5) high efficiency for low power consumption, (6) low noise for high dynamic range receiver, (7) low temperature operation for reliable and reduced cooling, and (8) technology leverage for low cost. While every known semiconductor material can be a candidate and has its own uniqueness and tradeoffs with another, engineering the fabrication process and structure of the device is the key to a successful RF active component, especially for flexible and stretchable electronics. For instance, microwave devices are principally difficult to fabricate on foreign substrates, due to the small feature sizes and high-temperature processes

required for high-performance, compared with devices operating at low frequencies or direct-current (DC) levels. Moreover, RF passive components, such as inductors, capacitors and transmission lines are as equally important as the active ones, which together form a complete microwave integrated circuit [7].

It should be noted that both the cut-off frequency (f_T) and maximum oscillation frequency (f_{max}) are important characteristics of figure of merits in an RF transistor. f_T is the frequency where the short-circuit current gain ($|h_{21}|$) of RF transistors goes to unity when it is biased as a common-emitter or common-source configuration. f_{max} is the frequency where the unilateral gain (U) of RF transistors goes to unity. For high-speed analog and digital circuits, the cut-off frequency is used to evaluate the switching speeds of the devices. Maximum oscillation frequency is more significant for microwave integrated circuits that are typically used as amplifiers. As an example, equations that are used to estimate the relationship between power consumption and f_{max} of a metal-oxide-semiconductor field-effect transistor (MOSFET), is provided below:

$$g_m = I_0 \cdot \left(\frac{q}{nkT}\right) \cdot \exp\left(\frac{q(V_{GS} - V_{th})}{nkT}\right) \text{ where, } I_D = \left(\frac{W}{L} \cdot C_{ox} \cdot \mu_n\right) \cdot (V_{GS} - V_{th}) \cdot V_{DS}$$

Therefore, $g_m \propto \ln(I_D)$

$$f_T = \frac{g_m}{2\pi(C_{gs} + C_{gd})} \rightarrow f_T \propto \ln(I_D)$$

$$f_{max} = \frac{f_T}{2\sqrt{(R_g + R_s) \cdot g_o + 2\pi \cdot R_g \cdot C_{gd} \cdot f_T}} \approx \frac{f_T}{2\sqrt{(R_g + R_s) \cdot g_o}} \rightarrow f_{max} \propto \ln(I_D)$$

By plotting g_m versus ln (I_D), power consumption at lower f_{max} can be estimated. In general, simultaneously achieving both high f_T and f_{max} is important for RF electronics. In addition, f_T and f_{max} should be approximately greater than the desired operating circuit frequency by 5 fold.

The key development history of the microwave electronic components on flexible or

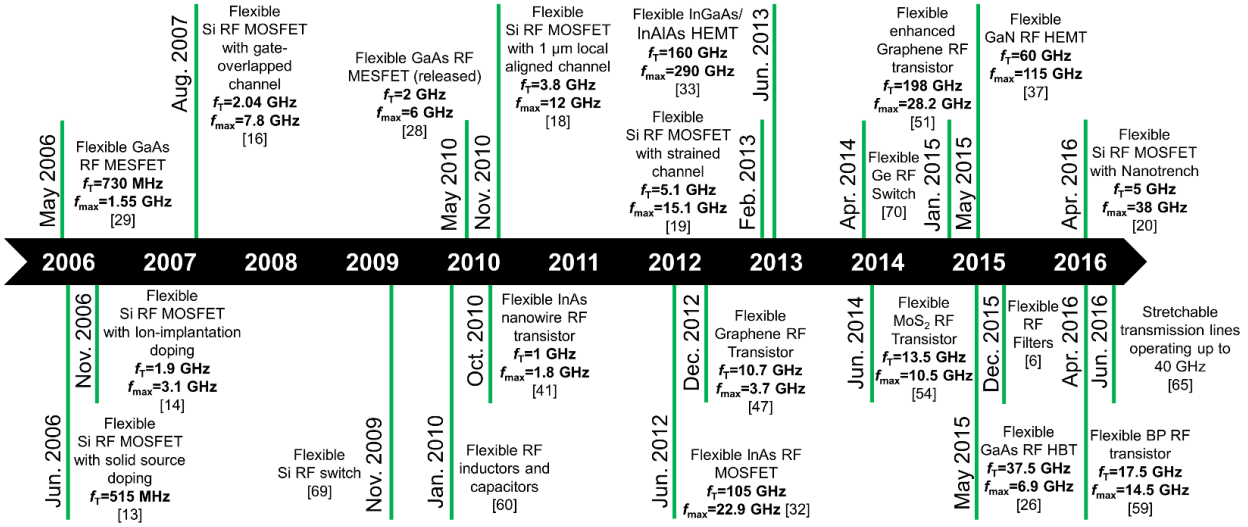

Figure 2.1. *Development history of high-frequency flexible and stretchable microelectronics. In each development, the choice of material, technical difference, and the RF figure of merits are described, as well as the corresponding reference.*

stretchable substrates are summarized in Figure 2.1. Important components, such as transistors, diodes, inductors, capacitors and transmission lines, required to form microwave integrated circuits are summarized in the timeline. In each development, the choice of material, technical difference, and the RF figure of merits are described. Organic electronics were among the earliest developments for flexible electronics [8]. The ease of fabrication, mechanical flexibility, and low cost make organic semiconductors a decent choice for active devices. Nevertheless, the poor intrinsic mobility of the organic materials is generally inadequate for high-frequency electronics. Single-crystalline inorganic semiconductors are the most favorable options that satisfy the high mobility criteria. With the development of transferrable silicon (Si) nanomembranes, the highly abundant material with decent mobility that is widely incorporated into modern complementary metal–oxide–semiconductor (CMOS) chips [9] was utilized to create flexible transistors operating

at high-frequencies [10-17]. Followed by this first development, advanced fabrication techniques and engineering, such as strain-sharing channels and high-performance doping, were implemented to manipulate the mobility of the material, maximize the performance and enhance the high-frequency responses of the transistors [13, 15]. High-frequency devices using materials with superior mobility, such as compound materials, 1-dimensional (1-D) or 2-dimensional (2-D) materials in thin-film formats, were introduced later to overcome limitations of Si. Record speeds were achieved using these materials as shown in Figure 2.1; however, the techniques used to fabricate many of these compound devices are relatively expensive and difficult to manufacture, and the development stage for 2-D materials fabrication is still young and immature to be utilized in a microwave circuit. As there exists more difficult challenges in designing a microwave integrated circuit, it is important to develop devices that can be reproduced with uniform performance parameters using materials that already have a mature fabrication infrastructure.

A high-speed transistor made using Si is by far the most cost-effective and easily reproducible

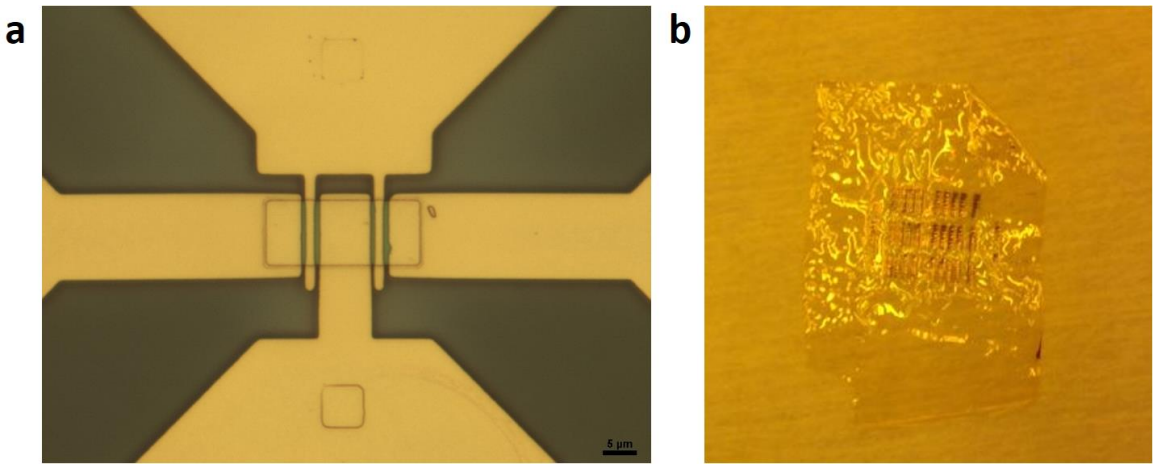

Figure 2.2. *(a) Optical microscopy image of high-frequency flexible MOSFET with 500 nm gate length. (b) Photograph of the ultrathin flexible MOSFET.*

method to obtain a device with high frequency response. Using standard microfabrication approach combined with transfer printing method, a high-speed Si-based MOSFET on ultrathin polyimide film was demonstrated. The fabrication of ultrathin Si MOSFET began by growing screen oxide on a p-type (260 nm) silicon-on-insulator (SOI) wafer, followed by photolithography to expose ion-implantation sites. A Phosphorous based ion implantation was conducted with 25 eV energy, 5×10^{15} dose, and 7° tilt, which was activated at 900 °C in N_2 ambient. The ion implanted Si NM was released from the SOI wafer by etching micro-holes to expose the buried oxide layer and expedite the release process. Meanwhile, a handling substrate was prepared by coating and curing of poly(methyl methacrylate) (PMMA) and polyimide PI on a clean Si wafer, where the released Si NM was transfer printed onto. On this carrying wafer, standard MOSFET fabrication was carried out using 30 nm of Al_2O_3 as gate insulator on a 500 nm channel. An optical image of the completed transistor is shown in Figure 2.2a. Finally, another PI layer was coated and patterned on the MOSFET to passivate the device and the substrate was immersed in boiling acetone to remove PMMA and release the entire flexible film. Figure 2.2b shows a photograph of the released device. Figure 2.3 shows the transfer curve and current versus voltage of the measured transistor. Figure

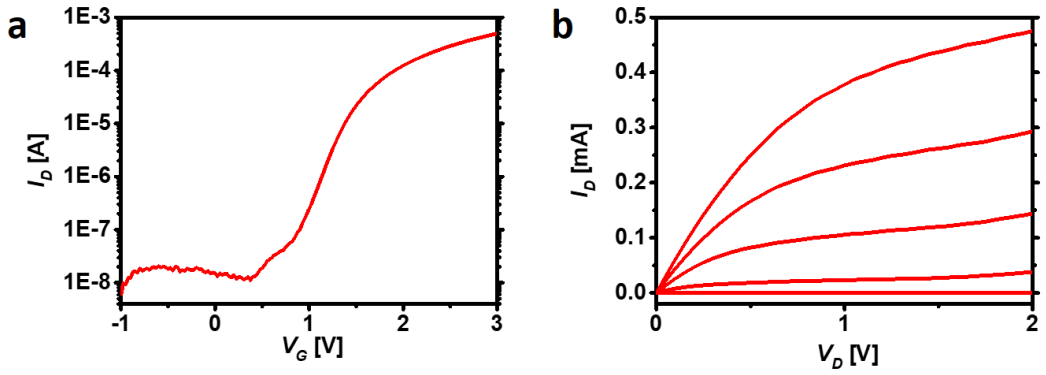

Figure 2.3. *(a) Measured transfer curve and (b) current-voltage curve of the high-frequency flexible MOSFET.*

2.4 shows the measured current gain (H_{21}) and power gain (G_{max}) of the MOSFET, where the f_T was 2.38 GHz and the f_{max} was 12.47 GHz. Despite using deposited gate oxide, the frequency responses of the device were exceptional, compared to devices presented in the past. This is attributed to the reduced gate channel length and carefully controlled ion implantation. We expect that these figure-of-merits will further improve by utilizing high-quality insulators with advanced deposition techniques, such as atomic layer deposition.

2.3. High-Speed Passive Devices

Together with the active devices, passive devices, such as inductors and capacitors are essential components for fast, flexible, and stretchable electronics. In conventional microwave circuits like the monolithic microwave integrated circuit (MMIC), the metal layers for all the components, such as spiral patterns for inductors, plates for the capacitors, matching lines for transmission lines etc. are simultaneously deposited on a single substrate, which minimizes design and fabrication process errors. To mimic this MMIC technique, every component must be designed, fabricated, and analyzed individually on the target substrate, since microwave components tend to

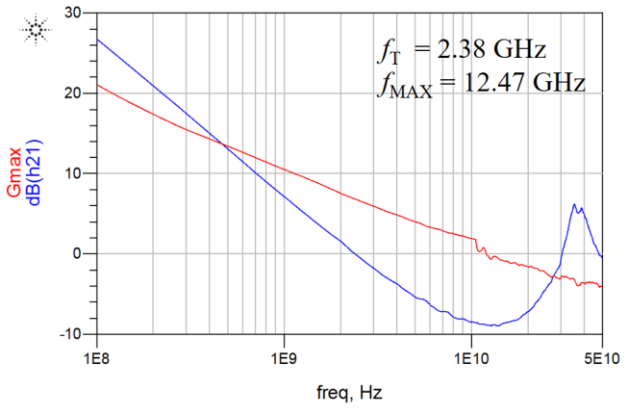

Figure 2.4. *Measured frequency response characteristics of the high-frequency flexible MOSFET.*

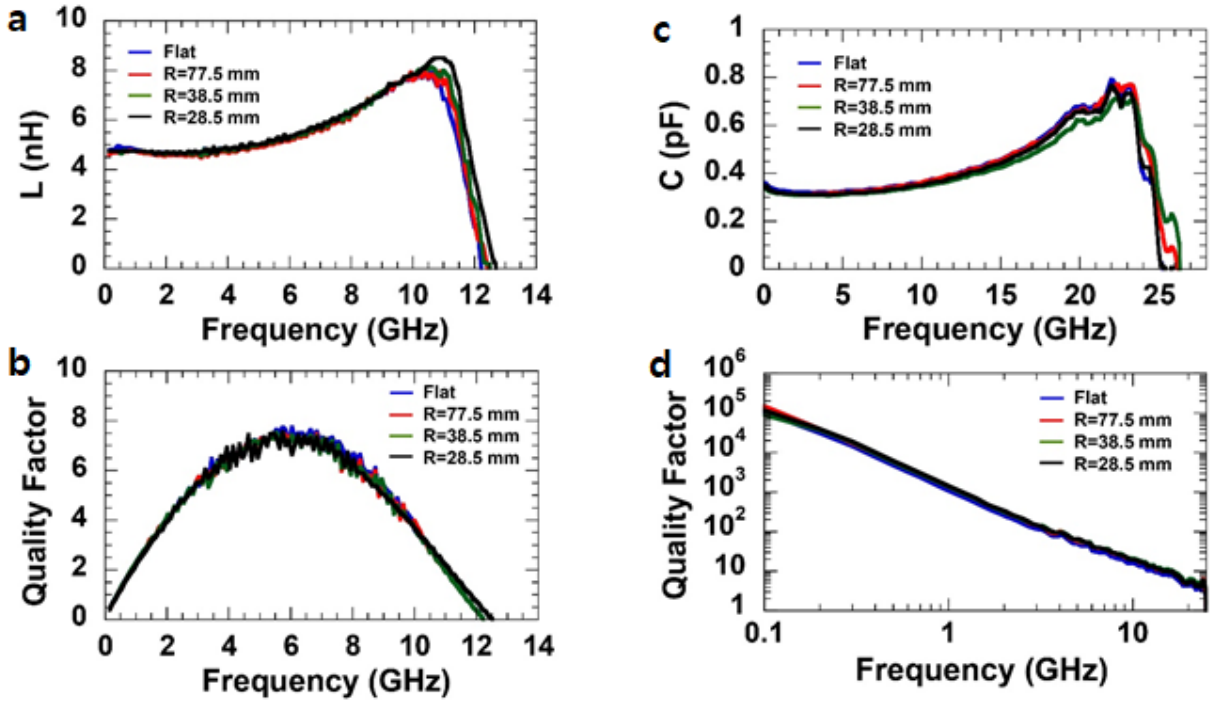

Figure 2.5. *Measured 4.5 turns spiral inductors with 4.5 turns, 20 μm line width, and 4 μm line space (a) L values and (b) Q values as a function of frequency under flat and various bending states. Measured (c) capacitance values and (d) Q values of an 88 × 88 μm² MIM capacitor as a function of frequency under flat and bending conditions.*

be heavily affected by the dielectric, electrical, and mechanical properties of the underlying substrate. For instance, a capacitor with a capacitance of 10 pF at 2 GHz operating on a silicon substrate will likely have different capacitance at 2 GHz on a PI substrate. This is the same for every microwave component, posing a substantial challenge for high-frequency flexible electronics. Several important factors must be optimized to design a spiral inductor that has large inductance with a high quality (Q) factor, such as the type of substrate, the number of turns, the spacing between the conducting lines, and the width of the lines. By calculating the self-inductance

and mutual inductance, the inductance value and the Q factor of an inductor can be obtained. In addition, because the capacitance of a parallel plate capacitor is reliant on the overlap area of two plates, the dielectric properties, and the dielectric thickness, these parameters should be optimized for a reasonable size, required capacitance, and enough Q factor. With careful selection of materials and design, we have fabricated high-performance flexible inductor and capacitor on plastic substrates [18].

Spiral inductors require precise photolithography for determined spacing in between the metal lines. Capacitors are generally implemented between interconnected metal layers using dielectrics deposited at high-temperatures. To demonstrate these on a flexible substrate, mechanically robust inductors and capacitors were fabricated on a polyethylene terephthalate (PET) film, which is one of the most commonly used plastic substrate in flexible electronics [19]. The first high-speed flexible inductors and capacitors showed a high-frequency response with mechanical robustness under the bending test. However, the self-resonance frequency (f_{res}) of these inductors and capacitors were limited to 8 GHz. Optimizing the design and utilizing high-K dielectrics, we have improved the same components that are compatible up to X-band (8 to 12 GHz) operation with a good flexibility [18]. The f_{res} of inductors showed 12.3 GHz and the of the capacitors showed 25.1 GHz using TiO_2 as the dielectric material between the capacitor plates, as presented in Figure 2.5.

In the process of developing a thin-film polymer adhesive that would allow easy bonding of electronic devices onto plastic substrates, we have analyzed the dielectric properties of the polymer to investigate its potential as high-K dielectrics for flexible electronics [20]. This ultraviolet (UV) curable adhesive can be coated in ultrathin films that are as thin as 150 nm. To define the dielectric properties of the adhesive in the radio frequency (RF) range, a simple metal-insulator-metal (MIM) capacitor (40 × 200 μm) was fabricated. The processing of MIM capacitor began with uniform

deposition of bottom metal plate (Cr/Au = 10/400 nm) on a high-resistivity (~8000 Ω) (111) bulk wafer with 830 nm of thermally grown SiO_2 for reduction of substrate coupling and RF losses. Adhesive was then spin-coated at 1500 rpm for 30 seconds (820 nm), followed by UV beam exposure and hard baking for complete curing. Top metal plate (Cr/Au = 10/ 500 nm) was deposited on top of the cured adhesive followed by a photolithography process to pattern and etch-back the top metal plate. This top metal pattern was further used as a hard mask to define the adhesive insulator using reactive ion etching procedure (Unaxis 790). The bottom plate was also photo-defined using etch-back procedure. A thick layer of SU-8 resist was then patterned to form via holes and isolation for the top and bottom electrodes followed by metal interconnect deposition with lift off technique to form ground-signal-ground (GSG) probing pads for RF probing. Figure 2.6 shows an image of the completed MIM capacitor and the lumped element circuit model consisting of the main capacitance of the MIM capacitor (C_{MIM}), parasitic substrate capacitance (C_{AD}), the series resistances (R_{VIA}) which describe the dielectric losses, and the lead inductances

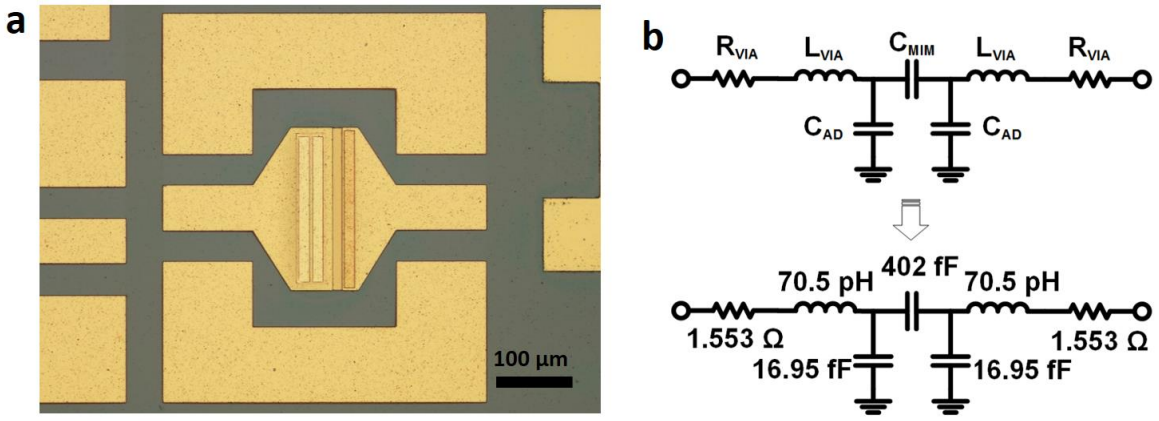

Figure 2.6. *(a) Optical microscope image of MIM capacitor with Au electrodes and Adhesive dielectric. (b) Equivalent circuit model and its de-embedded circuit. The lumped elements are matched and de-embedded from measured S-parameters of the capacitor using ADS.*

(L_{VIA}) associated with the equivalent circuit.

Figure 2.7 shows the extracted properties from measured parameters. The RF characteristics of the fabricated MIM capacitor were measured using Agilent E8364A performance network analyzer. Capacitance and the dielectric properties were analyzed from the extraction of scattering (S) parameters of the capacitor. The de-embedded values of the capacitor's equivalent circuits were optimized against the measured two-port S-parameters in Agilent Advanced Design System (ADS) software. Here, the simulated result yield a good agreement with the measured values, as shown in Figure 2.7a. Using simple relationship between the capacitance and the dielectric constant of the insulator,

$$C_{MIM} = \frac{\varepsilon_0 \varepsilon_r A}{t}$$

where, $\varepsilon_0 = 8.8542 \times 10^{-12} F \cdot m^{-1}$, the relative permittivity (ε_r) was extracted. Figure 2.7b shows that the ε_r averaged around ~5 in frequencies between 0 and 8 GHz, where the frequency

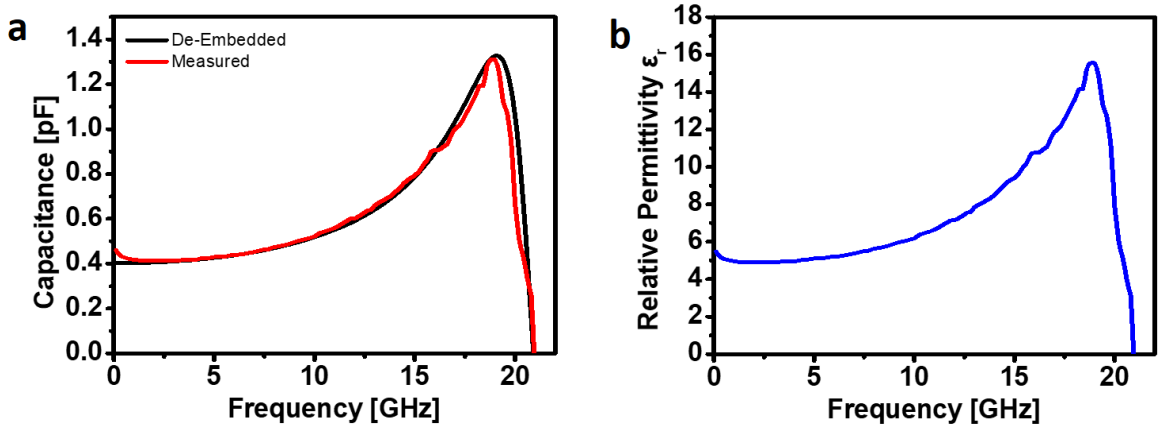

Figure 2.7. *(a) Capacitance as a function of frequency. De-embedded and measured results are shown in black and red lines, respectively. (b) Measured relative permittivity (ε_r) of adhesive as a function of frequency. Linear $\varepsilon_r \sim 5$ is observed in the 0 to 8 GHz frequency range.*

range had linear capacitance. Compared to the dielectric constants of most polymer based dielectric materials that typically range between 2 and 3, the results obtained here shows its superior advantages over others for use in polymer based RF circuits, where passive elements utilizing this material may be designed much smaller to obtain high capacitance and inductance.

2.4. Conclusion

The flexible active and passive devices presented in this section share common fabrication techniques that make their processes compatible with each other. Thus, such devices can be integrated together into a circuit to create various microwave electronics such as power amplifiers, low noise amplifiers and mixers in flexible and stretchable forms. The choice for semiconductor materials is important because the intrinsic electrical properties directly contribute to the output performances of the fabricated transistors. At the same time, process and design parameters determine the operating frequency and power level. Scaling of microwave transistors and reducing the gate length to sub-micrometers can greatly improve f_T, whereas parasitic components, such as short-channel effects and parasitic resistances must be carefully controlled and reduced in order to maximize f_{max}. Thus, the techniques used to fabricate the transistors can further be optimized to improve f_T and f_{max} on flexible substrates. The substrate is another component of RF electronics that affects its performance. As an example, the flexible InAs transistor introduced in [21] resulted in degraded RF performances on PI substrate with f_T of 105 GHz and f_{max} of 22.9 GHz compared to the transistor fabricated on a SiO_2 substrate with f_T of 165.5 GHz and f_{max} of 45.4 GHz. Characteristics such as dielectric and thermal properties of the substrate affect the device performance. An ideal substrate is highly resistive and possess low loss tangent and high dielectric constant. Moreover, the substrate's high thermal conductivity prevents device overheating and low

loss tangent ensures suppressed RF loss. Such effects are often misanalysed during the design and RF circuits go through subsequent matchings and redesigns. Common substrates used for flexible and stretchable electronics in this summary were PI, PET, PEN, and Ecoflex®. These substrates, whether it is flexible or stretchable, possess low dielectric constant, low thermal conductivity, and high loss tangent compared to state-of-the-art substrates found in conventional RF chips. Although such poor conditions negatively affect the RF electronics performance, the sacrifice must be made as this is typically true for flexible and stretchable materials. Continuous efforts are being made to improve each of these characteristics in plastic or rubber materials to offer a more suitable substrate. Meanwhile, the device aspect of flexible and stretchable microwave electronics is rapidly improving.

Another important passive component is the transmission line which will be used to connect the abovementioned components. In a typical monolithic microwave integrated circuit, high speed signals flow via transmission lines that are in the form of micro-strips. Because micro-strips cannot be utilized in flexible or stretchable electronics due to the thickness of the substrate, different types of transmission lines must be adapted to make the circuit flexible and/or stretchable. In the following section, a novel type of stretchable transmission line that minimizes RF loss is presented.

2.5. Reference

[1] A. Umenei, "Understanding Low Frequency Non-Radiative Power Transfer," *Wireless Power Consortium contribution by Fulton Innovation LLC,* vol. 7575, 2011.

[2] J. I. Agbinya, "Wireless Power Transfer," *Principles of Inductive near Field Communications for Internet of Things,* vol. 18, pp. 281-300, 2011.

[3] N. Shinohara, "Wireless Power Transfer via Radiowaves," *Wireless Power Transfer Via Radiowaves*, pp. 1-237, 2014.

[4] Z. Ma, Y. H. Jung, J.-H. Seo, T.-H. Chang, S. J. Cho, J. Lee, *et al.*, "Materials and Design Considerations for Fast Flexible and Stretchable Electronics," *2015 Ieee International Electron Devices Meeting (IEDM)*, 2015.

[5] Y. H. Jung, H. Zhang, and Z. Ma, "Wireless Applications of Conformal Bioelectronics," in *Stretchable Bioelectronics for Medical Devices and Systems*, J. A. Rogers, R. Ghaffari, and D.-H. Kim, Eds., ed Cham: Springer International Publishing, 2016, pp. 83-114.

[6] Y. H. Jung, J.-H. Seo, W. Zhou, and Z. Ma, "High-Speed, Flexible Electronics by Use of Si Nanomembranes," in *Silicon Nanomembranes*, ed: Wiley-VCH Verlag GmbH & Co. KGaA, 2016, pp. 113-142.

[7] S. March, "Practical MMIC Design.–Artech House," ed: Inc, 2006.

[8] B. Crone, A. Dodabalapur, Y.-Y. Lin, R. W. Filas, Z. Bao, A. LaDuca, *et al.*, "Large-scale complementary integrated circuits based on organic transistors," *Nature*, vol. 403, pp. 521-523, Feb 2000.

[9] L. Venema, "Silicon electronics and beyond," *Nature*, vol. 479, pp. 309-309, Nov 17 2011.

[10] E. Menard, R. G. Nuzzo, and J. A. Rogers, "Bendable single crystal silicon thin film transistors formed by printing on plastic substrates," *Applied Physics Letters*, vol. 86, p. 093507, Feb 2005.

[11] J.-H. Ahn, H.-S. Kim, K. J. Lee, Z. Zhu, E. Menard, R. G. Nuzzo, *et al.*, "High-speed mechanically flexible single-crystal silicon thin-film transistors on plastic substrates," *IEEE Electron Device Letters*, vol. 27, pp. 460-462, Jun 2006.

[12] H.-C. Yuan and Z. Ma, "Microwave thin-film transistors using Si nanomembranes on

flexible polymer substrate," *Applied Physics Letters,* vol. 89, p. 212105, Nov2006.

[13] H.-C. Yuan, Z. Ma, M. M. Roberts, D. E. Savage, and M. G. Lagally, "High-speed strained-single-crystal-silicon thin-film transistors on flexible polymers," *Journal of Applied Physics,* vol. 100, p. 013708, Jul 1 2006.

[14] H.-C. Yuan, G. K. Celler, and Z. Ma, "7.8-GHz flexible thin-film transistors on a low-temperature plastic substrate," *Journal of Applied Physics,* vol. 102, p. 034501, Aug 1 2007.

[15] H.-C. Yuan, M. M. Kelly, D. E. Savage, M. G. Lagally, G. K. Celler, and Z. Ma, "Thermally processed high-mobility MOS thin-film transistors on transferable single-crystal elastically strain-sharing Si/SiGe/Si nanomembranes," *IEEE Transactions on Electron Devices,* vol. 55, pp. 810-815, Mar 2008.

[16] L. Sun, G. Qin, J.-H. Seo, G. K. Celler, W. Zhou, and Z. Ma, "12-GHz Thin-Film Transistors on Transferrable Silicon Nanomembranes for High-Performance Flexible Electronics," *Small,* vol. 6, pp. 2553-2557, Nov 22 2010.

[17] H. Zhou, J.-H. Seo, D. M. Paskiewicz, Y. Zhu, G. K. Celler, P. M. Voyles, *et al.*, "Fast flexible electronics with strained silicon nanomembranes," *Scientific Reports,* vol. 3, p. 1291, Feb 2013.

[18] S. J. Cho, Y. H. Jung, and Z. Ma, "X-Band Compatible Flexible Microwave Inductors and Capacitors on Plastic Substrate," *Ieee Journal of the Electron Devices Society,* vol. 3, pp. 435-439, Sep 2015.

[19] L. Sun, G. Qin, H. Huang, H. Zhou, N. Behdad, W. Zhou, *et al.*, "Flexible high-frequency microwave inductors and capacitors integrated on a polyethylene terephthalate substrate," *Applied Physics Letters,* vol. 96, p. 013509, Jan 4 2010.

[20] T.-I. Kim, M. J. Kim, Y. H. Jung, H. Jang, C. Dagdeviren, H. A. Pao, *et al.*, "Thin film

receiver materials for deterministic assembly by transfer printing, " *Chemistry of Materials,* vol. 26, no. 11, pp. 3502-3507, May 2014.

[21] C. A. Wang, J. C. Chien, H. Fang, K. Takei, J. Nah, E. Plis, *et al.*, "Self-Aligned, Extremely High Frequency III-V Metal-Oxide-Semiconductor Field-Effect Transistors on Rigid and Flexible Substrates," *Nano Letters,* vol. 12, pp. 4140-4145, Aug 2012.

CHAPTER 3
Stretchable twisted-pair transmission lines for microwave frequency wearable electronics

Stretchable electrical interconnects based on serpentines combined with elastic materials are utilized in various classes of wearable electronics. However, such interconnects are primarily for direct current or low-frequency signals and incompatible with microwave electronics that enable wireless communication. In this paper, design and fabrication procedures are described for stretchable transmission line capable of delivering microwave signals. The stretchable transmission line has twisted-pair design integrated into thin-film serpentine microstructure to minimize electromagnetic interference, such that the line's performance is minimally affected by the environment in close proximity, allowing its use in thin-film bioelectronics, such as the epidermal electronic system. Detailed analysis, simulations, and experimental results show that the stretchable transmission line has negligible changes in performance when stretched and is operable on skin through suppressed radiated emission achieved with the twisted-pair geometry. Furthermore, stretchable microwave low-pass filter and band-stop filter are demonstrated using the twisted-pair structure to show the feasibility of the transmission lines as stretchable passive components. These concepts form the basic elements used in the design of stretchable microwave components, circuits, and subsystems performing important radio frequency functionalities, which can apply to many types of stretchable bioelectronics for radio transmitters and receivers.

3.1. Introduction

The remarkable mechanical properties of stretchable electrical interconnects in serpentine

shapes have enabled the integration of high-performance electronic devices in a myriad of applications [1]. In particular, the unique design and integration have led to the most advanced type of wearable electronics, the so-called "epidermal electronic system" (EES) that match the physical properties to the epidermis for conformal relief on its surface [2]. Together with state-of-the-art performance inorganic semiconductor devices, serpentine type interconnects have transformed rigid- and flat-based electronics into highly stretchable EES, ranging from various types of epidermal sensors to photonic devices [3-8]. Further developments for low modulus responses to large deformations and high durability of stretchable interconnects utilized different types of serpentine designs such as the self-similar serpentines [9, 10], fractal-inspired designs [11], nanomesh structures [12], and bio-inspired triangular and spiral designs [13, 14]. Moreover, materials and techniques have evolved to enhance the stretchability and conformality of the interconnects and to ease the fabrication steps of integrating the electronics onto skin [15-21]. However, studies on the stretchable interconnects were limited to designs primarily for electrical operation at direct current (DC) signals or alternating current (AC) signals at very low frequency, where the interconnects only utilize a single conductor line. As the frequency of the operating AC signals rises to radio frequency (RF) level (i.e. multi-gigahertz), electromagnetic waves of the signals must be considered in the design to prevent the loss along the conductor distance. It should be noted that in most mobile electronics, including cell phones and wearable gadgets that use wireless communication systems, high-frequency integrated circuits are essential to perform various RF functionalities, such as microwave mixing, power amplification, low-noise amplification, and high-frequency switching [22, 23]. As the next 5th generation (i.e. 5G) mobile network, which is expected to launch in 2020, reportedly aiming at millimeter wave bands (3 to 300 GHz) and as wearable electronics market rapidly increases, transmission lines operating at

microwave frequencies practical for future EES are highly desired [24, 25].

This report presents design and fabrication of high-frequency interconnects with low RF and radiation losses for EES. Because high-frequency signals also carry electromagnetic wave with short wavelengths, transmission lines that use two conductors, where one is considered a ground become necessary. Two important RF characteristics of the scattering (S-) parameters define the performance of the transmission lines: insertion loss is the loss of power that results from an inserted device; return loss is the loss of power in the signal returned or reflected. To create near-lossless transmission lines, lower insertion loss and higher return loss in magnitude are desired. A few groups have presented on the high-frequency stretchable interconnects in the past: Huyghe *et al*. utilized the coplanar waveguide (CPW) design, where two ground conductors run in parallel on both sides of the signal conductor that has serpentine shape [26]; Jeon *et al*. utilized the differential design, where the two conductors, signal and ground, run in parallel that has zigzag shape [27]. Nonetheless, these CPW and differential lines are not suitable for EES at microwave frequencies, due to the large sizes (400 μm and 640 μm in line width, respectively) and RF performances that are only operable up to 3 GHz and 1 GHz, respectively. Here, we demonstrate stretchable transmission lines using novel designs having superior high-frequency lossless characteristics and that are sufficiently small (25 μm in line width) to be integrated with active components, such as the high-frequency flexible transistors and diodes [28-32].

3.2. Design and fabrication of stretchable twisted-pair transmission line

The ultrathin structure of EES requires designs for RF transmission lines that are immune to external noise for minimal interference with the skin. In Figure 3.1, we present a unique type of wearable stretchable transmission line that can operate at microwave frequencies with extremely

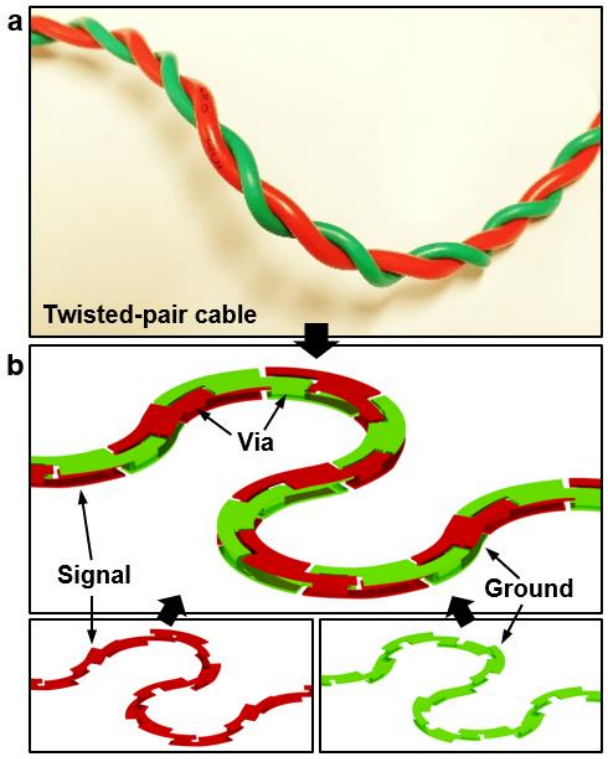

Figure 3.1. *The concept of twisted-pair-based stretchable transmission line. (a) Photograph of a twisted-pair electrical cable, where signal and ground wires are intertwined. (b) Schematic illustration of the twisted-pair-based stretchable transmission line. The twisted-pair geometry for signal and ground is formed by utilizing two-segmented metal blocks in dual-layer construct, crisscrossing each other with multiple via-holes.*

low level of loss by integrating twisted-pair geometry into the "horseshoe" shaped serpentine structures. Inspired by the twisted-pair cabling from the telephone cables where the two conducting wires are twisted together (Figure 3.1a), this balanced pair is well-known to cancel out electromagnetic interference (EMI) from external sources [33]. The twisted-pair geometry for signal and ground is mimicked into thin-film format by utilizing two-segmented metal blocks in dual-layer construct, crisscrossing each other with multiple via-holes as shown in Figure 3.1b.

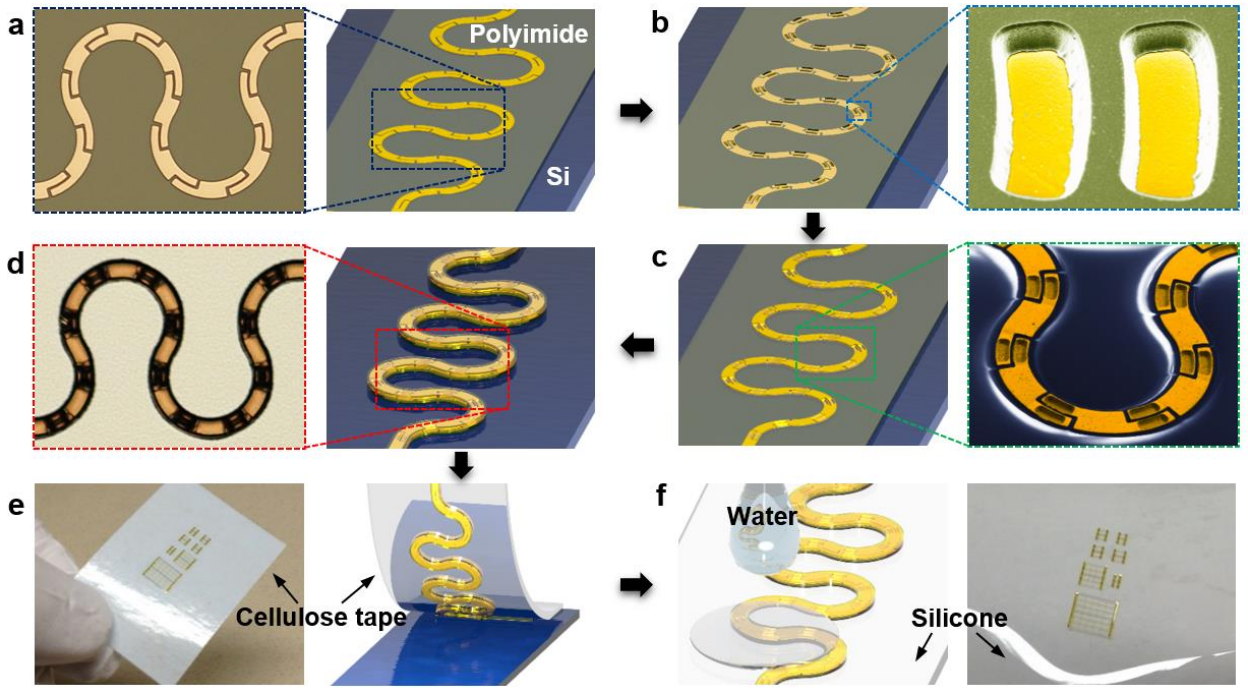

Figure 3.2. *The fabrication process and photograph images of the twisted-pair-based stretchable transmission line. (a)-(f) Schematic illustration of the fabrication process along with optical microscopy (OM), scanning electron microscopy (SEM), or photograph images. (a) Blocks of gold microstructure with fingers on both sides are deposited on a polyimide-coated Si (OM image shown on the left), (b) followed by coating a layer of polyimide and opening via-holes with 60° sidewall slope on the fingers (false-colored SEM image of the via-holes shown on the right). (c) Blocks of gold microstructure with fingers on opposite side to those of the first layer are deposited (false-colored SEM image shown on the right), (d) and encapsulated with polyimide and defined into serpentine shape (OM image shown on the left). (e) The transmission line is delaminated from the Si substrate using a water-soluble cellulose tape (photograph shown on the left), (f) and transfer printed onto a silicone elastomer substrate. It is soaked in water to dissolve the tape (photograph shown on the right).*

Figure 3.2 shows the schematic illustration, along with scanning electron microscopy (SEM) or optical microscopy (OM) images, of the fabrication process for twisted-pair-based stretchable transmission line. On a polyimide-coated Si substrate, multiple blocks of metal (Au) structure with fingers on each side were deposited along the serpentine shape (Figure 3.2a), followed by opening polyimide-based via-holes on all the fingers (Figure 3.2b). Slanted side wall of the via-holes was created by isotropic etching to ensure perfect connection between the two layers and to minimize resistance. Another layer of metal structures with fingers on opposite side of that of the first metal blocks was deposited to create twisted-pair geometry (Figure 3.2c). The transmission line was defined by etching into serpentine shapes (Figure 3.2d) and was delaminated from the Si substrate using water-soluble cellulose tape (Figure 3.2e), followed by transfer printing the line onto a modified silicone (Ecoflex) substrate and dissolving the tape with water (Figure 3.2f). The twisted-pair stretchable transmission line was designed to have characteristic impedance of 50 ohms for compatible integration with other RF components. Polyimide was used as the encapsulating and dielectric spacer material due to enhanced mechanical stability of the line and favorable RF characteristics, featuring low RF loss tangent ($\tan \delta = 0.006$) with a dielectric constant of 3 at microwave frequencies [34, 35]. Furthermore, modified silicone (Ecoflex) was used as the substrate, which is a suitable biocompatible elastomer for many EES, as it can be casted in ultrathin sheets and can conformally attach to the skin [2, 16]. It is also a suitable elastomer for RF electronics as it features relatively low RF loss tangent ($\tan \delta = 0.01$) with a dielectric constant of 2.5 at microwave frequencies [36]. Figure 3.3a shows the camera image of the stretchable transmission line array laminated on the back of hand. The transmission line can withstand the strain and stress due to the deformations of the skin as shown in the stretched, compressed, and pressed images in Figure 3.3b, 3.3c, and 3.3d, respectively.

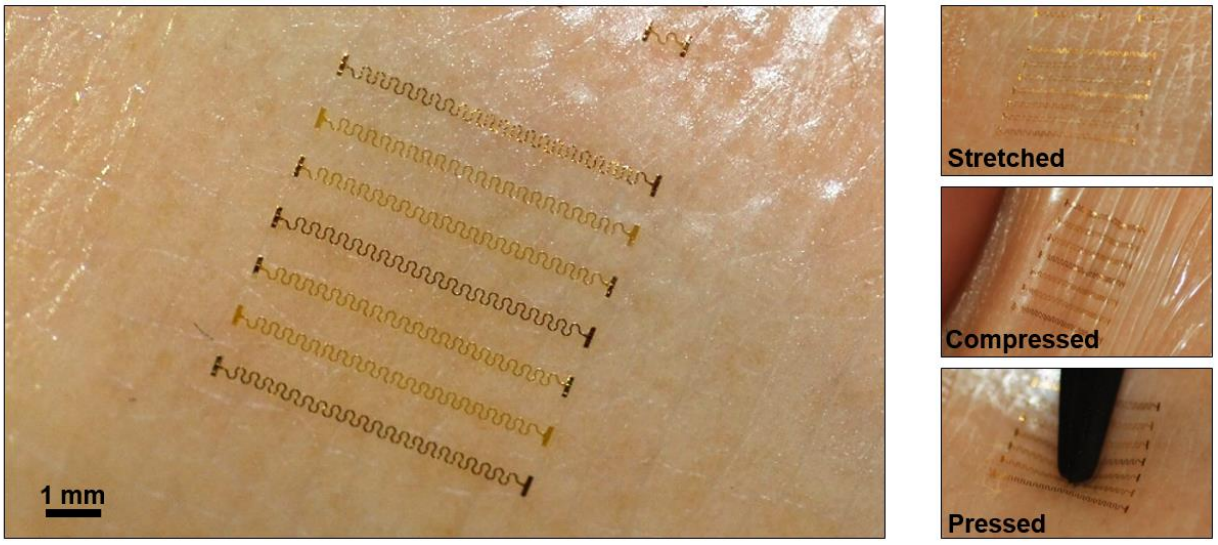

Figure 3.3. *(a) Photograph image of the stretchable transmission line array laminated on the back of hand. Images of the array (b) stretched, (c) compressed, (d) and pressed on the back of hand.*

3.3. Properties of stretchable twisted-pair transmission line

To demonstrate the advantages of our twisted-pair-based stretchable transmission line, it is compared with conventional single layer transmission line, in terms of RF loss, radiation confinement and mechanical stability via simulations, as presented in Figure 3.4, where the top and bottom rows show the results of the single layer line and the twisted-pair-based line, respectively. For each line, the total length was fixed to 960 μm and all other dimensions were optimized for RF loss characteristics. For the twisted-pair-based line, the width was fixed to 25 μm and the conductor thickness, via-hole size, and dielectric spacer thickness were optimized to be 1 μm, 150 μm^2, and 5 μm, respectively. Detailed simulation comparisons against variants of the addressed optimization parameters for twisted-pair-based line are presented in Figure 3.5. In Figure 3.4a, schematic illustrations presenting the structures of the single layer line and twisted-

pair-based line used for each simulation are shown. Figure 3.4b shows simulated S-parameters from 0 to 40 GHz for each transmission line. Because RF transmission line must be accompanied

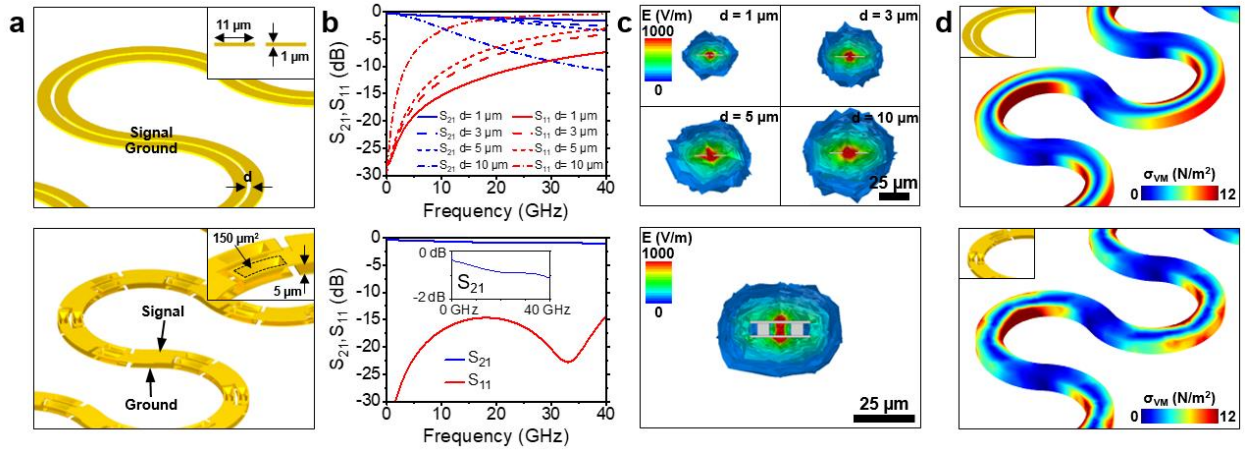

Figure 3.4 *Comparisons of the twisted-pair-based transmission line against single layer line via scattering (S-) parameters, radiation confinement, and mechanical simulations. Top and bottom rows show calculated results of the single layer and twisted-pair, respectively. (a) Schematic illustration of the single layer line (top) and twisted-pair-based line (bottom). Inset images show the dimension details of the lines. (b) Simulated high-frequency S-parameters for single layer line (top) and twisted-pair-based line (bottom). Single layer line is simulated with a ground conductor parallel to the signal conductor for separation distances of 1, 3, 5, and 10 μm. Magnified plots of* S_{21} *as a function of frequency are shown in the insets for the twisted-pair-based line. (c) Radiation confinement calculations showing electric field distribution at 40 GHz for single layer line (top) and twisted-pair-based line (bottom). Single layer line is simulated with a ground conductor parallel to the signal conductor for separation distances of 1, 3, 5, and 10 μm. (d) Finite element analysis showing equivalent von Mises stress distribution in the serpentine structures with 1 N of tensile force applied on single layer line (d = 3 μm) (top) and twisted-pair-based line (bottom). Inset images show the metal structures embedded in the polyimide.*

with a ground conductor, the conventional single conductor line is not capable of transmitting signals, but is simply a radiator (antenna) at high-frequencies, as demonstrated by Hussain *et al* [37]. The simplest way to remedy the high RF loss (radiation) of the single line wires for possible RF signal transmission is to parallel it with another conductor at a small distance. Such paralleled conductors can be considered as differential transmission lines (i.e. ground running parallel to the signal). Simulations were performed on the simple transmission lines in terms of separation distance variants (d = 1, 3, 5, and 10 μm) between signal and ground that have 11 μm in width. As presented, the insertion loss and return loss showed acceptable performance at high-frequencies only when the two conductors were as close as 1 μm, whereas the lines became too lossy with over 3 μm of separation distance. The twisted-pair-based transmission lines showed superior performance with low insertion loss (only -1.14 dB at 40 GHz) and high return loss up to 40 GHz, which are attributed to the excellent confinement of the high-frequency waves in the structures. Figure 3.4c shows the cross-section view of electric field calculations at 40 GHz for each line type. Unlike microwave transmission lines in conventional chips, the radiation confinement can be especially critical for EES as the electronics are in close proximity with the skin that may induce interference. Therefore, structures with low level of radiation with minimal EMI is desired. For a differential line, the fields are well-confined for a 1 μm separation (note: the conductor thickness is also 1 μm), but the fields deviate out severely as the separation distance increases. In contrast, the fields in the twisted-pair-based line were well-confined within the structure with smooth deviation around the line. This well-confined behavior of the electric fields is attributed to the suppressed radiated emission from the reduced loop area formed between signal and ground conductors in the balanced twisted-pair structure [33]. Furthermore, to demonstrate the mechanical stability, a finite element method was used to calculate the von Mises stress of each structure

encapsulated with polyimide as shown in Figure 3.4d. With equivalent tensile force applied in each line, more stress was observed at the edge of the serpentine in the single layer line than those of

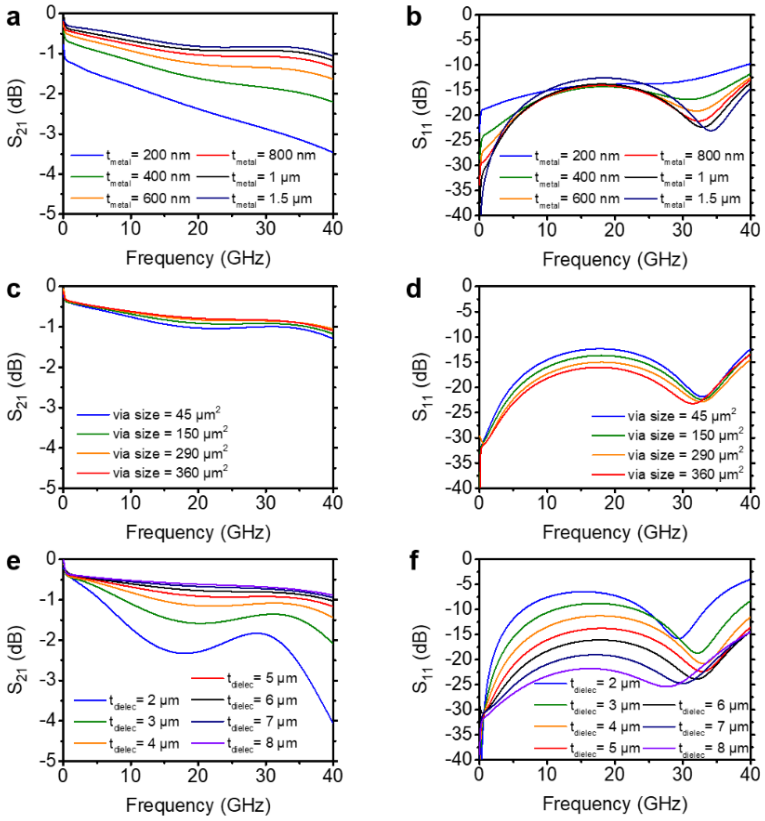

Figure 3.5. *Comparisons of simulated scattering (S-) parameters against variants of optimization parameters for twisted-pair-based stretchable transmission line. (a) Simulated S_{21} and (b) simulated S_{11} against frequency for conductor (signal and ground) thickness variation. Both losses are enhanced with increasing thickness and saturate at 1 µm. Optimal signal thickness is 1 µm. (c) Simulated S_{21} and (d) simulated S_{11} against frequency for via-hole size variation. Both losses are enhanced with increasing size and saturate at 150 µm^2. Optimal via-hole size is 150 µm^2. (e) Simulated S_{21} and (f) simulated S_{11} against frequency for dielectric spacing thickness variation. Both losses are enhanced with increasing thickness. Optimal spacing thickness is 5 µm, as thicker lines are incompatible with thin-film fabrication process.*

twisted-pair-based line. In fact, mechanical studies on stretchable interconnects suggest multi-layer over multiple interconnects in a single layer [38, 39]. For instance, previous studies demonstrated that dual-layer stretchable interconnects exhibited less changes in electrical performance than dual in-plane stretchable interconnects in responding to elongations. Moreover, the dual-layer stretchable interconnects had three orders of magnitude longer elongation life cycles than the in-plane ones [38]. Thus, for a transmission line that always require two conductors (signal and ground), use of single layered structure would be unfavorable in terms of mechanical stability.

Experimental results of the fabricated twisted-pair-based stretchable transmission line are presented in Figure 3.6. Precise conductor dimensions and spacings that carry signals with minimal reflections and power losses implemented into fabrication process achieved the best possible performance of the lines and matched results with simulation as presented in Figure 3.6a. Electrical characterization on the transmission lines with four different lengths demonstrates the feasibility of short and long transmission lines at high-frequencies. They were defined by the number of serpentine turns within the line as optically shown in Figure 3.6b; for instance, the line with two turns has two “horseshoe” shaped serpentine structures. Clearly, the DC resistance increases with line length (Figure 3.6c) and more insertion loss (Figure 3.6d), due to resistive and dielectric loss, was present in longer lines. The resistive loss of the conductor must be kept as low as possible since it attributes to RF insertion loss. Therefore, with a fixed total line width of 25 μm, the twisted-pair-based line generally has a lower resistive loss than single layer line since the twisted-pair line has a larger conductor area resulting from its dual layer construct. The maximum line width of each (signal or ground) conductor in a single layer transmission line was 12 μm (1 μm spacing). Figure 3.7 shows the measured DC resistance of single layer lines with three different widths (i.e., 10, 11, and 12 μm) were higher than the resistance of the twisted-pair-based line for all four line

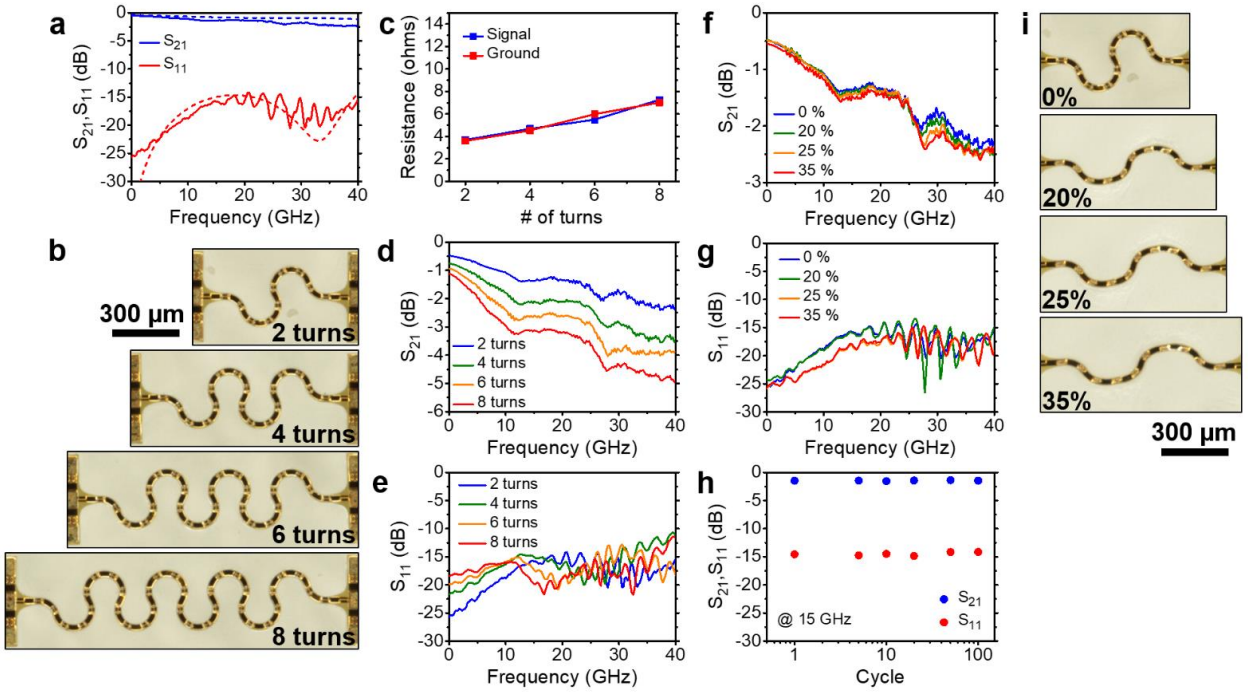

Figure 3.6. *Electrical characterization of the twisted-pair-based stretchable transmission line. (a) Simulated (dotted) and measured (solid) scattering (S-) parameters of the transmission line with two turns of serpentine shape plotted against frequency. (b) Optical microscopy (OM) images of the stretchable transmission lines with different lengths. Four lines with 2, 4, 6, and 8 turns of serpentine are shown from top to bottom. (c) DC resistance measured for signal and ground conductors plotted for the four lines with different number of turns. (d) Measured S_{21} and (e) S_{11} of the four lines with different number of turns plotted against frequency. (f) Measured S_{21} and (g) S_{11} of the stretchable transmission line with two turns of serpentine at 0%, 20%, 25%, and 35% elongation plotted against frequency. (h) S_{21} and S_{11} at 15 GHz for different cycles of stretching to 35% elongation. (i) OM images of the stretchable transmission line with two turns of serpentine at 0%, 20%, 25%, and 35% elongation.*

lengths measured. Changes in return loss (Figure 3.6e) followed a similar trend of increasing loss with increasing length up to ~10 GHz, but started to lose trend as the frequency rises, due to the

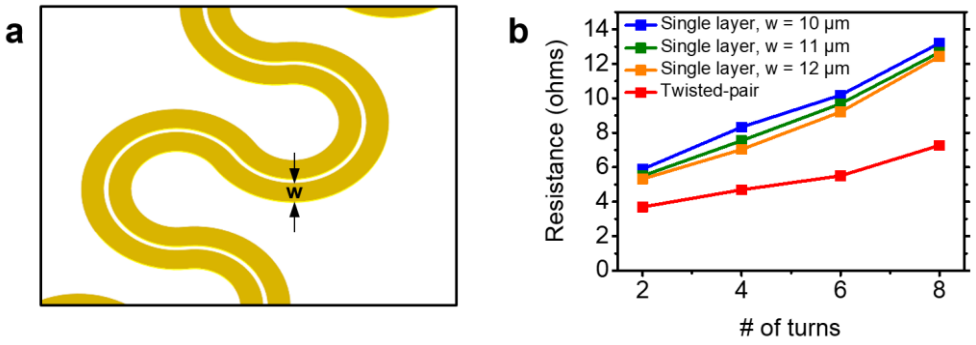

Figure 3.7. *Comparisons between the DC resistance for single layer lines with different widths and twisted-pair-based line. (a) Schematic illustration of a single layer line showing the width of a conductor that was measured. (b) The DC resistance measured for single layer lines with different widths (i.e., 10, 11, and 12 μm), and twisted-pair-based line as a function of the number of turns.*

mismatch losses at high-frequencies. Regardless of the trend, all of the twisted-pair-based transmission lines exhibited good lossless characteristics at high-frequencies. Measurement pads designed to minimize radiation loss and to fit with ground-signal-ground (G-S-G) RF probes induced negligible loss to the transmission lines, as presented in Figure 3.8. In order to investigate the effects during elongation, the twisted-pair-based line with two turns were measured at different points of elongation (0%, 20%, 25%, and 35%) as presented in Figure 3.6f-i. RF measurements under stretched conditions were performed on a modified probe station with the stretcher mounted, as shown in Figure 3.9. Negligible increases in insertion loss were observed, as shown in Figure 3.6f, which are attributed to the slight increase in the electrical resistance due to strain. Also, negligible performance change in return loss (Figure 3.6g) characteristics were observed during elongation. The S-parameters of the transmission line were invariant even after 100 cycles of 35% elongation (Figure 3.6h). OM images of the measured transmission line at different points of

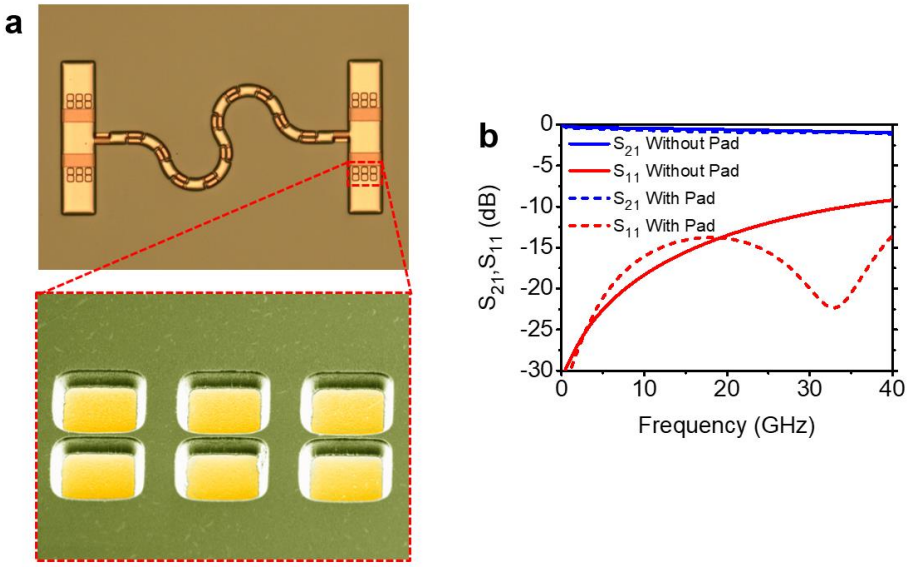

Figure 3.8. *Effects of the measurement pad on the performance of twisted-pair-based stretchable transmission line. (a) Optical microscopy image (top) showing the stretchable transmission line with ground-signal-ground measurement pads on both sides. Scanning electron microscopy image (bottom) of the via-holes in the pads connecting the grounds. (b) Scattering parameters simulation of the line shown in (a) compared against the line without the pads.*

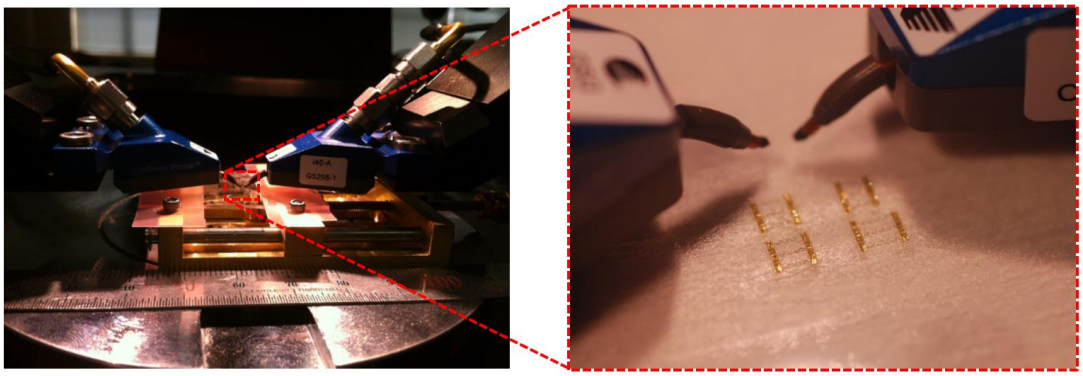

Figure 3.9. *RF measurement setup of the stretchable transmission line, with stretcher mounted on a modified RF probe station.*

elongation are presented in Figure 3.6i. At 40% elongation, a physical breaking occurred as presented in Figure 3.10.

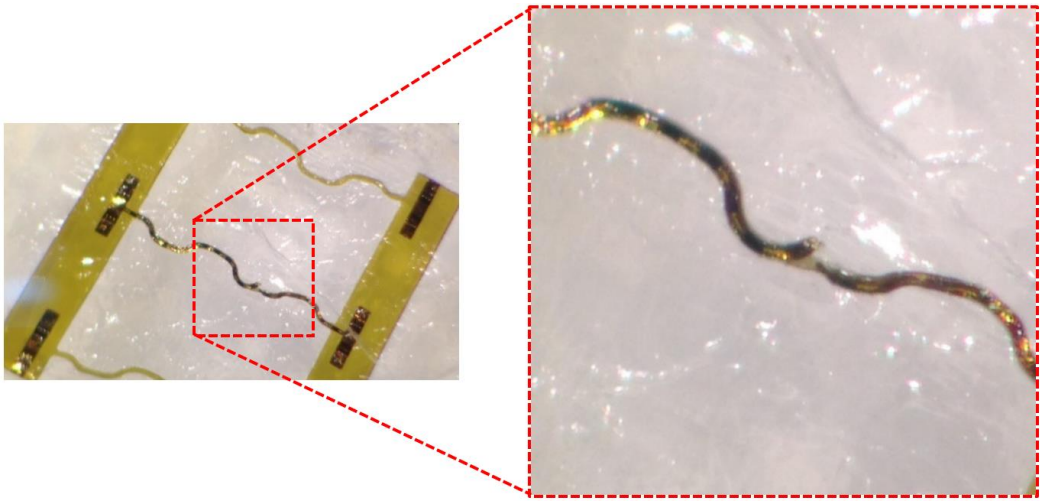

Figure 3.10. *Optical microscopy image showing physical breakdown of the twisted-pair-based stretchable transmission line at 40% elongation.*

3.4. Stretchable twisted-pair microwave filters

In most microwave circuits, RF filters are used to attenuate or transmit signals at certain frequency bands. To demonstrate the practicality of the twisted-pair-based stretchable transmission line as such passive components, microwave filters are demonstrated and presented in Figure 3.11. Despite the complex geometry of the twisted-pair, filters can be created by treating the transmission line as distributed element component, which allows relatively straightforward approach of fabricating filters. Instead of adding short lengths of matching stubs as in conventional microstrip-based filters, blocks of twisted-pairs in serpentine form were added to the sides of the transmission line to generate resonance at stop or pass frequencies. As a result, two commonly used filters, the low-pass filter and the band-stop filter, were achieved as tapped edge-couple filter structure. For the low-pass filter shown in Figure 3.11a, each stub length was 575 µm. As presented in Figure 3.11b, it exhibited a wide band low-pass characteristic where the 3 dB cut-off frequency

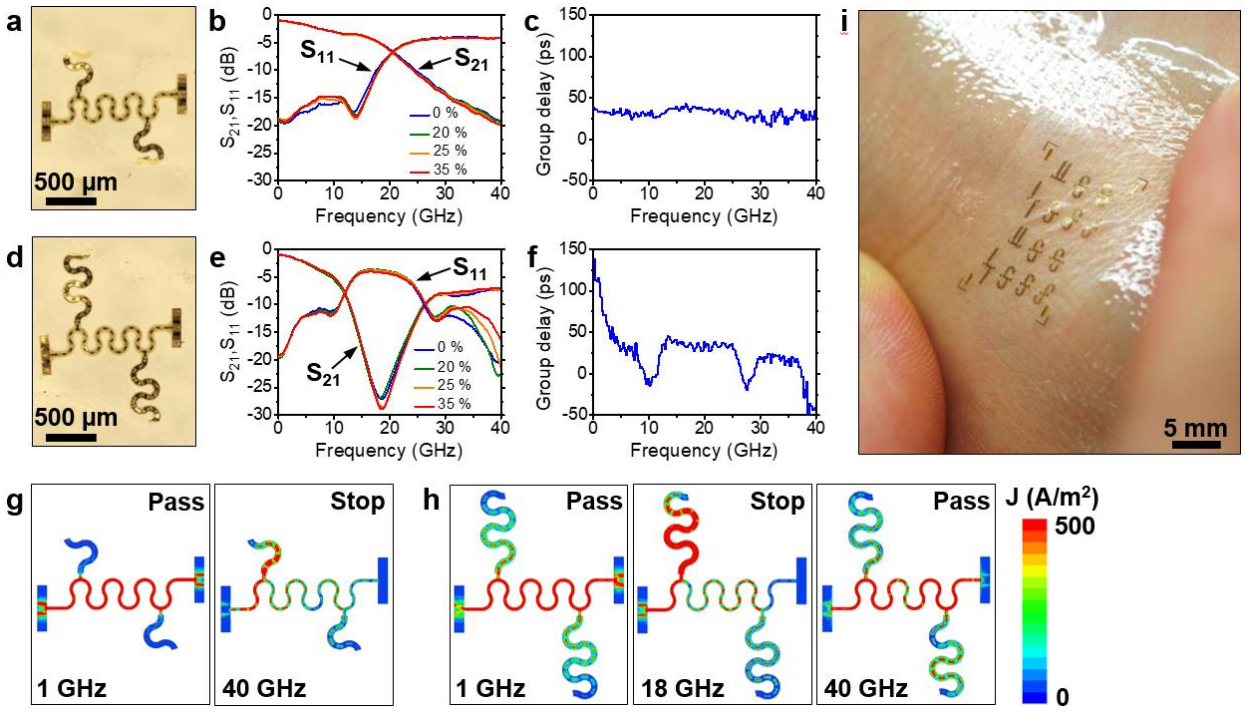

Figure 3.11. *Stretchable high-frequency filters based on twisted-pair structure. (a) Optical microscopy (OM) image of the twisted-pair-based stretchable low-pass filter. (b) Scattering (S-) parameters of the stretchable low-pass filter at 0%, 20%, 25%, and 35% elongation plotted against frequency. (c) Group delay of the stretchable low-pass filter plotted against frequency. (d) OM image of the twisted-pair-based stretchable band-stop filter. (e) S-parameters of the stretchable band-stop filter at 0%, 20%, 25%, and 35% elongation plotted against frequency. (f) Group delay of the stretchable band-stop filter plotted against frequency. (g) Simulated surface current density distribution in the stretchable low-pass filter at 1 GHz (pass) and 40 GHz (stop). (h) Simulated surface current density distribution in the stretchable band-stop filter at 1 GHz (pass), 18 GHz (stop), and 40 GHz (pass). Color bar on the right is for both (g) and (h). (i) Photograph image of the stretchable filters laminated and stretched on the back of hand.*

was 9.9 GHz, with a relatively flat band and low insertion loss between 11.6 GHz (-3.5 dB) and

15 GHz (-3.74 dB). Relatively consistent group delay responses were observed in the flat pass-band, as presented in Figure 3.11c. The center frequency of the band-stop filter with 1.45 mm in stub length (Figure 3.11d) was 18.2 GHz and its return loss was -3.59 dB, as presented in Figure 3.11e. The stop bandwidth was between 12.5 GHz (-6.61 dB) and 25 GHz (-6.57 dB). The group delay in Figure 3.11f exhibited a uniform and flat response of approximately 27.5 ps in the stop band, which represents good robustness against signal distortion. Both filters exhibited slight performance changes under stretched (0%, 20%, 25%, and 35% elongations) conditions, as presented in Figure 3.11b and 3.11e. Surface current density distributions in the low-pass filter and the band-stop filter at pass- and stop-band frequencies provide clear view of the current

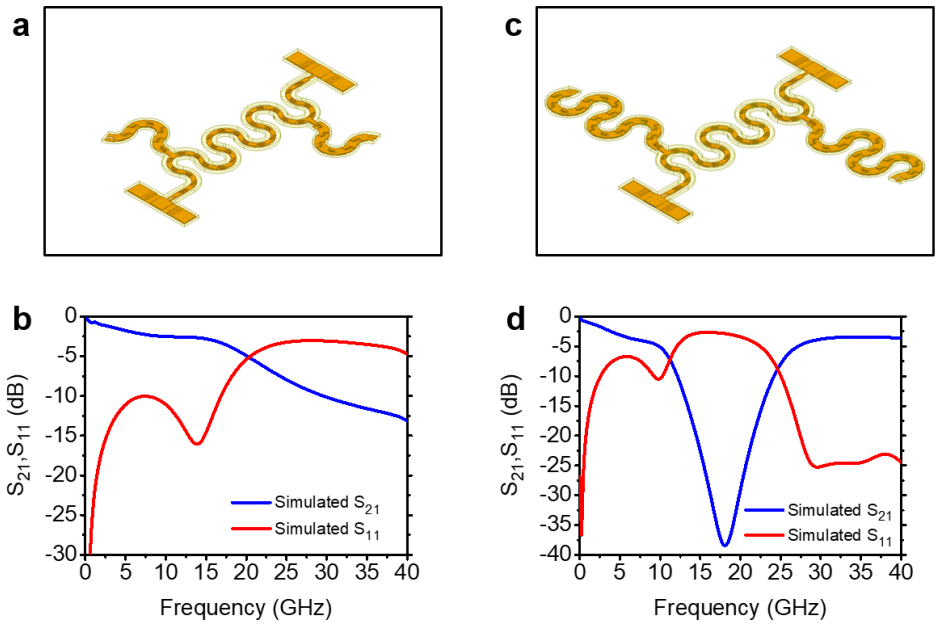

Figure 3.12. *(a) Computer-aided design (CAD) showing the equivalent structure of the low-pass filter used for surface current density calculation in Figure 3.11g. (b) Simulated scattering (S-) parameters of the low-pass filter shown in (a). (c) CAD showing the equivalent structure of the band-stop filter used for surface current density calculation in Figure 3.11h. (b) Simulated S-parameters of the band-stop filter shown in (c).*

concentrations as presented in Figure 3.11g and 3.11h, respectively. The calculated S-parameters of the equivalent designs used for the current distribution calculations are presented in Figure 3.12. The ability to create stretchable filters which operate at high-frequencies demonstrate the

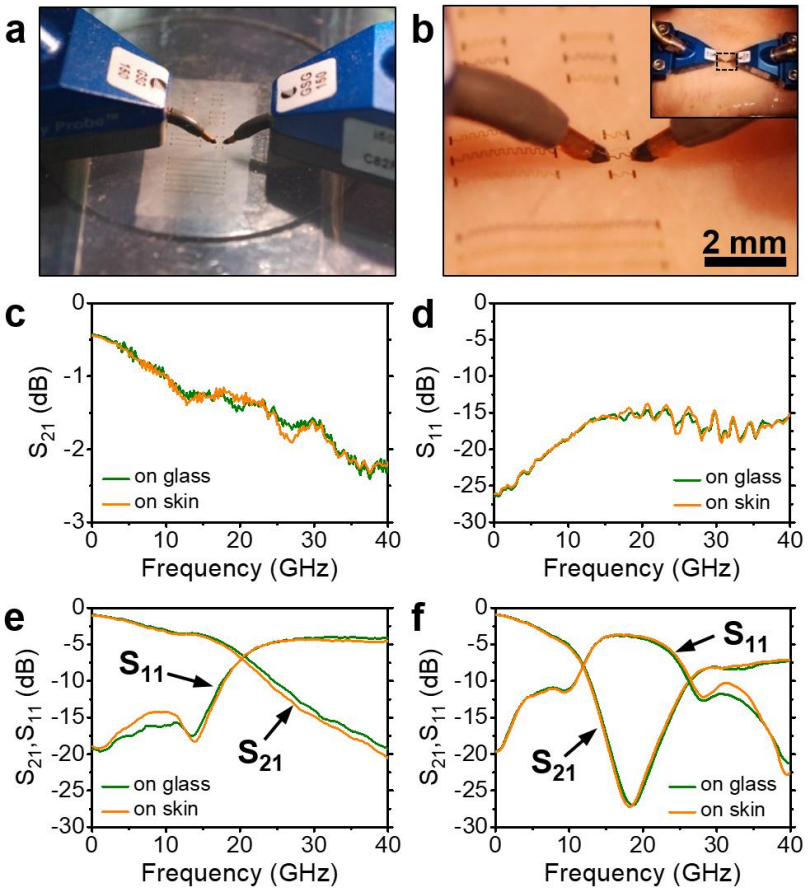

Figure 3.13. *Stretchable twisted-pair-based transmission line and filters tested on glass and skin. (a) Photograph image showing the measurement setup of stretchable transmission line on a glass slide and (b) on skin. (c) Measured S_{21} and (d) S_{11} of the stretchable transmission line with two turns on glass substrate and porcine skin plotted against frequency. (e) Measured scattering (S-) parameters of the stretchable low-pass filter on glass substrate and porcine skin plotted against frequency. (f) Measured S-parameters of the stretchable band-stop filter on glass substrate and porcine skin plotted against frequency.*

feasibility of the twisted-pair-based stretchable transmission lines in microwave integrated circuits for wearable electronics. Figure 3.11i shows a set of twisted-pair-based stretchable filters laminated and stretched on the back of hand.

3.5. Stretchable twisted-pair transmission line and filters on skin

As presented in Figure 3.6 and 3.11, stretchable high-frequency transmission line and filters were built and tested successfully by utilizing the twisted-pair geometry. The negligible performance changes due to physical elongations have shown the practicality of such interconnects in potential high-frequency stretchable electronic systems. Furthermore, the twisted-pair geometry should also suppress radiated emission and minimize interference with external noise, which would allow its operation without significant performance changes on unusual surfaces, such as the skin. To prove that the transmission line and filters can perform the same on skin, they were measured on a porcine skin sample mounted onto the RF probe station, as shown in Figure 3.13. Porcine tissues were examined to best mimic the electrical properties of the human tissues at microwave frequencies. For instance, the permittivity, ε_r and the conductivity, σ of the porcine skin at 2.4 GHz are 38 and 1.46 S/m, respectively, which match closely to that of the human skin where ε_r and σ are 40 and 1.6 S/m, respectively [40]. For comparison, the devices were measured on a glass slide, as shown in Figure 3.13a and re-measured on a porcine skin, as shown in Figure 3.13b. The measured S-parameters on skin were compared with the measured results on a glass substrate. As presented in Figure 3.13c and 3.13d, there were no significant changes in terms of insertion and return losses for a line with two turns measured on glass and skin. The stretchable low-pass filter and band-stop filter also showed negligible performance changes when measured on porcine skin, as shown in Figure 3.13e and 3.13f, respectively.

3.6. Experimental section

Fabrication of wearable twisted-pair-based stretchable transmission line: On a temporary Si substrate, a thin layer of polymethyl methacrylate (950 PMMA A2, Microchem, 60 nm) was spin casted as a sacrificial polymer, followed by hard baking at 180 °C for 3 min. A layer of polyimide (PI, Sigma-Aldrich, 5 μm) was spin casted two times at 2,500 rpm for 60 s, followed by soft baking at 150 °C for 4 min and hard baking at 350 °C under N_2 (4 Torr) ambient for 3 h. Blocks of metals with fingers that form the lower signal and ground conductors were deposited (Ti/Au = 10/1,000 nm) using an electron-beam evaporator via a photoresist (AZ5214E) lift-off process, followed by spin casting and baking another layer of PI (5 μm) on top, to form the dielectric spacer. A hard mask (Cu = 100 nm) was deposited to expose the via-holes, using a positive resist (S1813) based lift-off process for precision alignment of the holes. Isotropic reactive ion plasma etching (RIE, CF_4/O_2 = 2/80 sccm, pressure = 75 mTorr, power = 100 W) of the PI for 2 min opens the via-holes with side wall angle of 60°. Second metal layer (Ti/Au = 10/1,000 nm) of blocks with fingers on opposite sides to that of the first, was deposited using a lift-off process, followed by final passivation with PI (5 μm). Hard mask was formed with Cu (100 nm) by electron-beam evaporator via a lift-off process, followed by anisotropic reactive ion plasma etching (RIE, O_2 = 80 sccm, pressure = 150 mTorr, power = 200 W) of PI (total 15 μm) for 4 h, to define the serpentine shape of the line. The twisted-pair-based stretchable transmission lines on the temporary substrate were boiled in acetone at 200 °C for 30 min to remove the underlying sacrificial layer (PMMA). A water-soluble cellulose tape (3M) was laminated on the dried transmission lines and carefully picked up from the temporary substrate. A thin layer of oxide (Ti/SiO_2 = 5/50 nm) was deposited on the backside of the transmission line. Stretchable modified silicone (Ecoflex 00-30, Smooth-On Inc.) for the substrate was prepared by mixing (part A:part B = 1:1) and spin casting on Si

substrate at 500 rpm for 60 s, followed by curing at room temperature for 6 h. The fully cured Ecoflex was exposed with UV/ozone (UV-1, Samco, O_2 = 0.5 L/min) for 1 min, followed by immediate lamination of the cellulose tape with stretchable transmission line on the Ecoflex substrate. 1 h after the lamination, a strong covalent bond formed between the Ecoflex and oxide, which was immersed in water for 30 min to dissolve the tape.

Measurement and analysis: DC resistance of the stretchable transmission lines were measured using HP 4155B Semiconductor Parameter Analyzer. An Agilent E8364A PNA Series Network Analyzer was used to measure the S-parameter of the stretchable transmission lines with the measurement set-up calibrated to the Infinity G-S-G probe tips with 150 μm pitch using a standard Short-Open-Load-Thru (SOLT) calibration kit. The S-parameters obtained from the RF measurements were analyzed using the Advanced Design System (ADS) software. The RF characteristics and the radiation characteristics of the stretchable transmission lines were simulated using the Ansys High Frequency Structural Simulator (HFSS) software and the mechanical finite element method (FEM) simulations were performed using the COMSOL multiphysics modeling software.

3.7. Conclusion

In summary, the results presented here establish the design and fabrication techniques for stretchable transmission lines that operate at microwave frequencies, which are suitable as interconnects in EES requiring high-speed wireless communication capabilities. Miniaturized stretchable transmission line utilizing twisted-pair designs that has low RF and radiation loss were demonstrated and analyzed. Furthermore, stretchable microwave low-pass filter and band-stop filter were demonstrated using twisted-pair structures to show the feasibility of the twisted-pair-

based transmission lines as passive components. While not demonstrated in this work, this type of line is also applicable for high-speed digital circuits where the data rate is extremely high that require minimized interference from external noise. Integration of such transmission lines with active devices, such as transistors and diodes to build microwave integrated circuits in the form of EES remains one of the future challenges. Together with already-developed EES that can perform various types of clinical sensing, such high-performance transmission lines in stretchable format will provide opportunities for safe and remote monitoring of patients, through the development of high-speed wireless communication systems. It is expected that the wireless capabilities represented by such transmission lines would make their biomedical and many other applications fully compatible with the need of the forthcoming internet of things. A complete RF electronic device for wireless communication would also consist of antennas to transmit or receive signals. Numerous types of flexible and stretchable antennas incorporating interesting designs and materials have been demonstrated. Antenna designs are highly application-based as the factors from the surrounding environment are considered for maximized antenna gain. Interconnecting the antenna with proper conductor design in flexible or stretchable format will be critical for a successful integration with the devices and circuits. In the following section, a simple technique to fabricate flexible antenna is presented.

3.8. Reference

[1] D. S. Gray, J. Tien, and C. S. Chen, "High-conductivity elastomeric electronics," *Advanced Materials,* vol. 16, p. 393, Mar 2004.

[2] D.-H. Kim, N. Lu, R. Ma, Y.-S. Kim, R.-H. Kim, S. Wang, *et al.*, "Epidermal electronics,"

Science, vol. 333, pp. 838-43, Aug 2011.

[3] D. Son, J. Lee, S. Qiao, R. Ghaffari, J. Kim, J. E. Lee, *et al.*, "Multifunctional wearable devices for diagnosis and therapy of movement disorders," *Nature Nanotechnology,* vol. 9, pp. 397-404, May 2014.

[4] J. Kim, M. Lee, H. J. Shim, R. Ghaffari, H. R. Cho, D. Son, *et al.*, "Stretchable silicon nanoribbon electronics for skin prosthesis," *Nature Communications,* vol. 5, p. 5747, Dec 2014.

[5] R. C. Webb, Y. Ma, S. Krishnan, Y. H. Li, S. Yoon, X. Guo, *et al.*, "Epidermal devices for noninvasive, precise, and continuous mapping of macrovascular and microvascular blood flow," *Science Advances,* vol. 1, p. e1500701, 2015.

[6] X. Huang, Y. H. Liu, K. L. Chen, W.-J. Shin, C. J. Lu, G.-W. Kong, *et al.*, "Stretchable, Wireless Sensors and Functional Substrates for Epidermal Characterization of Sweat," *Small,* vol. 10, pp. 3083-3090, Aug 2014.

[7] B. Xu, A. Akhtar, Y. Liu, H. Chen, W.-H. Yeo, S. I. Park, *et al.*, "An Epidermal Stimulation and Sensing Platform for Sensorimotor Prosthetic Control, Management of Lower Back Exertion, and Electrical Muscle Activation," *Advanced Materials,* vol. 28, no. 22, pp. 4462-4471, Oct 2015.

[8] L. Gao, Y. Zhang, V. Malyarchuk, L. Jia, K.-I. Jang, R. C. Webb, *et al.*, "Epidermal photonic devices for quantitative imaging of temperature and thermal transport characteristics of the skin," *Nature Communications,* vol. 5, p. 4938, Sep 2014.

[9] S. Xu, Y. Zhang, J. Cho, J. Lee, X. Huang, L. Jia, *et al.*, "Stretchable batteries with self-similar serpentine interconnects and integrated wireless recharging systems," *Nature Communications,* vol. 4, p. 1543, Feb 2013.

[10] Y. Zhang, S. Xu, H. Fu, J. Lee, J. Su, K.-C. Hwang, *et al.*, "Buckling in serpentine microstructures and applications in elastomer-supported ultra-stretchable electronics with high areal coverage," *Soft Matter,* vol. 9, pp. 8062-8070, 2013.

[11] J. A. Fan, W.-H. Yeo, Y. Su, Y. Hattori, W. Lee, S.-Y. Jung, *et al.*, "Fractal design concepts for stretchable electronics," *Nature Communications,* vol. 5, p. 3266, Feb 2014.

[12] C. F. Guo, T. Sun, Q. Liu, Z. Suo, and Z. Ren, "Highly stretchable and transparent nanomesh electrodes made by grain boundary lithography," *Nature Communications,* vol. 5, p. 3121, Jan 2014.

[13] K.-I. Jang, H. U. Chung, S. Xu, C. H. Lee, H. Luan, J. Jeong, *et al.*, "Soft network composite materials with deterministic and bio-inspired designs," *Nature Communications,* vol. 6, p. 6566, Mar 2015.

[14] C. Lv, H. Yu, and H. Jiang, "Archimedean spiral design for extremely stretchable interconnects," *Extreme Mechanics Letters,* vol. 1, pp. 29-34, 2014.

[15] S. Yang, Y. C. Chen, L. Nicolini, P. Pasupathy, J. Sacks, S. Becky, *et al.*, ""Cut-and-Paste" Manufacture of Multiparametric Epidermal Sensor Systems," *Adv Mater,* vol. 27, pp. 6423-6430, Sep 2015.

[16] W.-H. Yeo, Y.-S. Kim, J. Lee, A. Ameen, L. Shi, M. Li, *et al.*, "Multifunctional Epidermal Electronics Printed Directly Onto the Skin," *Advanced Materials,* vol. 25, pp. 2773-2778, May 2013.

[17] C. Zhou, S. Bette, and U. Schnakenberg, "Flexible and Stretchable Gold Microstructures on Extra Soft Poly(dimethylsiloxane) Substrates," *Adv Mater,* vol. 27, pp. 6664-6669, Sep 28 2015.

[18] J.-W. Jeong, W.-H. Yeo, A. Akhtar, J. J. S. Norton, Y.-J. Kwack, S. Li, *et al.*, "Materials

and Optimized Designs for Human-Machine Interfaces Via Epidermal Electronics," *Advanced Materials,* vol. 25, pp. 6839-6846, Dec 2013.

[19] T. Someya. (2012). *Stretchable Electronics*.

[20] T. Cheng, Y. Zhang, W.-Y. Lai, and W. Huang, "Stretchable Thin-Film Electrodes for Flexible Electronics with High Deformability and Stretchability," *Advanced Materials,* vol. 27, pp. 3349-3376, Jun 2015.

[21] A. M. Hussain, E. B. Lizardo, G. A. Torres Sevilla, J. M. Nassar, and M. M. Hussain, "Ultrastretchable and Flexible Copper Interconnect-Based Smart Patch for Adaptive Thermotherapy," *Advanced Healthcare Materials,* vol. 4, pp. 665-673, Apr 2015.

[22] S. Marsh, *Practical MMIC design*. Norwood, MA: Artech House, Inc., 2006.

[23] I. D. Robertson and S. Lucyszyn, *RFIC and MMIC design and technology*, 2nd ed. London: Institution of Electrical Engineers, 2001.

[24] T. S. Rappaport, S. Sun, R. Mayzus, H. Zhao, Y. Azar, K. Wang, *et al.*, "Millimeter Wave Mobile Communications for 5G Cellular: It Will Work!," *IEEE Access,* vol. 1, pp. 335-349, 2013.

[25] W. Roh, J.-Y. Seol, J. Park, B. Lee, J. Lee, Y. Kim, *et al.*, "Millimeter-Wave Beamforming as an Enabling Technology for 5G Cellular Communications: Theoretical Feasibility and Prototype Results," *IEEE Communications Magazine,* vol. 52, pp. 106-113, Feb 2014.

[26] B. Huyghe, H. Rogier, J. Vanfleteren, and F. Axisa, "Design and Manufacturing of Stretchable High-Frequency Interconnects," *IEEE Transactions on Advanced Packaging,* vol. 31, pp. 802-808, Nov 2008.

[27] J.-W. Jeon, S.-K. Kim, J.-M. Koo, S.-M. Hong, Y.-J. Moon, S.-B. Jung, *et al.*, "Electrical characterization of differential stretchable transmission line," in *Microwave Symposium*

Digest (MTT), 2011 IEEE MTT-S International, 2011, pp. 1-4.

[28] L. Sun, G. Qin, J.-H. Seo, G. K. Celler, W. Zhou, and Z. Ma, "12-GHz Thin-Film Transistors on Transferrable Silicon Nanomembranes for High-Performance Flexible Electronics," *Small,* vol. 6, pp. 2553-2557, Nov 2010.

[29] Y. H. Jung, T.-H. Chang, H. Zhang, C. Yao, Q. Zheng, V. W. Yang, *et al.*, "High-performance green flexible electronics based on biodegradable cellulose nanofibril paper," *Nature Communications,* vol. 6, p. 7170, May 2015.

[30] C. Wang, J.-C. Chien, H. Fang, K. Takei, J. Nah, E. Plis, *et al.*, "Self-Aligned, Extremely High Frequency III-V Metal-Oxide-Semiconductor Field-Effect Transistors on Rigid and Flexible Substrates," *Nano Letters,* vol. 12, pp. 4140-4145, Aug 2012.

[31] G. Qin, H.-C. Yuan, G. K. Celler, W. Zhou, and Z. Ma, "Flexible microwave PIN diodes and switches employing transferrable single-crystal Si nanomembranes on plastic substrates," *Journal of Physics D-Applied Physics,* vol. 42, p. 234006, Dec 2009.

[32] H. Zhou, J.-H. Seo, D. M. Paskiewicz, Y. Zhu, G. K. Celler, P. M. Voyles, *et al.*, "Fast flexible electronics with strained silicon nanomembranes," *Scientific Reports,* vol. 3, p. 1291, Feb 2013.

[33] D. G. Kam, H. Lee, and J. Kim, "Twisted differential line structure on high-speed printed circuit boards to reduce crosstalk and radiated emission," *IEEE Transactions on Advanced Packaging,* vol. 27, pp. 590-596, Nov 2004.

[34] Y.-Y. Hsu, M. Gonzalez, F. Bossuyt, J. Vanfleteren, and I. De Wolf, "Polyimide-Enhanced Stretchable Interconnects: Design, Fabrication, and Characterization," *Ieee Transactions on Electron Devices,* vol. 58, pp. 2680-2688, Aug 2011.

[35] G. E. Ponchak and A. N. Downey, "Characterization of thin film microstrip lines on

polyimide," *Ieee Transactions on Components Packaging and Manufacturing Technology Part B-Advanced Packaging,* vol. 21, pp. 171-176, May 1998.

[36] P. Liu, S. Yang, A. Jain, Q. Wang, H. Jiang, J. Song, *et al.*, "Tunable meta-atom using liquid metal embedded in stretchable polymer," *Journal of Applied Physics,* vol. 118, p. 014504, Jul 7 2015.

[37] A. M. Hussain, F. A. Ghaffar, S. I. Park, J. A. Rogers, A. Shamim, and M. M. Hussain, "Metal/Polymer Based Stretchable Antenna for Constant Frequency Far-Field Communication in Wearable Electronics," *Advanced Functional Materials,* vol. 25, pp. 6565-6575, 2015.

[38] Y. Y. Hsu, C. Papakyrikos, D. Liu, X. Y. Wang, M. Raj, B. S. Zhang, *et al.*, "Design for reliability of multi-layer stretchable interconnects," *Journal of Micromechanics and Microengineering,* vol. 24, Sep 2014.

[39] Y. Y. Hsu, K. Lucas, D. Davis, B. Elolampi, R. Ghaffari, C. Rafferty, *et al.*, "Novel Strain Relief Design for Multilayer Thin Film Stretchable Interconnects," *Ieee Transactions on Electron Devices,* vol. 60, pp. 2338-2345, Jul 2013.

[40] Y. H. Jung, Y. J. Qiu, S. Lee, T. Y. Shih, Y. H. Xu, R. M. Xu, *et al.*, "A Compact Parylene-Coated WLAN Flexible Antenna for Implantable Electronics," *Ieee Antennas and Wireless Propagation Letters,* vol. 15, pp. 1382-1385, 2016.

CHAPTER 4
A compact parylene-coated WLAN flexible antenna for implantable electronics

This chapter presents a compact planar flexible antenna designed for wireless local area network (WLAN) using simple microfabrication techniques that are compatible with existing state-of-the-art flexible electronic devices. The antenna is fully insulated with biocompatible Parylene C film, which shows a cost-effective and highly feasible approach to making flexible antennas for implantable applications. Coating of ultrathin Parylene C film has shown negligible effects on the return loss and the radiation patterns of the antennas. The characteristics of the proposed antenna have also shown negligible change under different bending conditions. The original WLAN antenna working in air was successfully tuned to operate under implanted condition at 2.4 GHz by tuning the length of the radiator. The measured results showed that the tuned implantable antenna is suitable for integration with flexible and implantable electronics.

4.1. Introduction

Recent advancements in flexible electronics have been seeking towards bio-integrated electronics which match with curvilinear surfaces of skin, organs, and tissues for accurate measurements and safe use in patients [1]. However, many of the existing approaches either lack the ability to communicate wirelessly or use near field communication systems (NFC) to power the devices from a very short distance, which limits fully implantable systems to certain clinical applications [2].

Flexible antennas operating in wireless local area network (WLAN) can provide a route to creating high speed wireless data transmission systems that can be combined with other flexible

devices to transmit and receive signals in a myriad of applications. Antenna designs utilizing novel materials and techniques have been demonstrated in flexible forms [3-7]. Also, several kinds of implantable antennas, which are operating in the Medical Implant Communications Service (MICS) or the Industrial, Scientific, and Medical (ISM) bands have been proposed in [8]. However, many of the antennas were incompatible with existing flexible electronic devices, or limited by rigid substrates that were too thick to be integrated in the body. Moreover, most of the reports use tissue mimicking gels as their design parameters, but such approach does not prove that the antennas may be used in practical applications, as different types of tissues have large range in their electrical properties. In this paper, we present a simple approach to make implantable, yet compact and flexible monopole antenna consisting of meandered strips and a coupling patch, fabricated on a thin polyimide substrate. The antenna was first designed to operate in air and tuned at later stage after studying the effects when implanted under a porcine skin. The variations of the S_{11} and the radiation gains of the flexible dual band (2.4 and 5.8 GHz) WLAN antenna were investigated and used to tune the antenna that can operate under implanted conditions at 2.4 GHz. 2.4 GHz was targeted due to the ability to create compact antennas and long-range capability out of many license-free frequency bands. Thus, an implantable antenna operating at such frequency will be attractive to many researchers and industries.

4.2. Antenna design

The geometry and dimensions of our proposed antenna in air are shown in Figure 4.1. The flexible antenna was composed of polyimide sandwiched between two metal layers (top and bottom layers). The two metal ground strips were connected via six metallized holes with a diameter of 0.6 mm, which is shown in Figure 4.1a and 4.1b. A 50 Ohms microstrip line with the

width of 0.28 mm was used as the feeding structure on the polyimide substrate which has the dielectric constant of 3.5, loss tangent of 0.003, and substrate thickness of 127 μm [9].

As shown in Figure 4.1, the presented antenna consisted of a U-shape strip and an open strip. The U-shape strip controls the lower WLAN operating band 2.4–2.484 GHz, while the open strip controls the upper WLAN operating band 5.15–5.875 GHz. The width of the low impedance line connected between the microstrip feed line and the monopole antenna (560 μm) and the distance

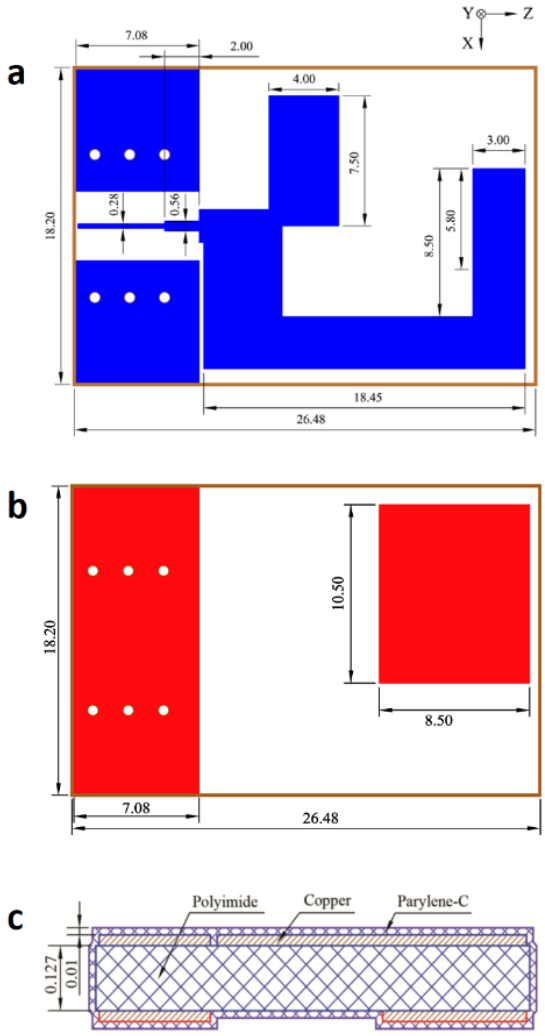

Figure 4.1. *Geometry and dimensions of designed antenna (dimensions in mm) (a) top layer, (b) bottom layer and (c) cross view.*

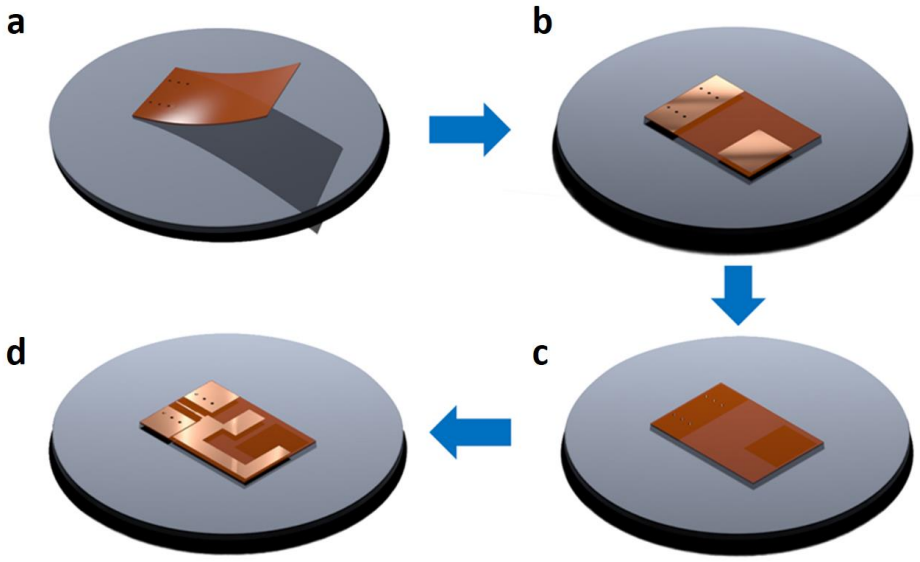

Figure 4.2. *Fabrication process of the antenna. (a) Laminate pre-cut Kapton film on temporary substrate, (b) deposit and etch-back copper for coupling patch, (c) de-laminate and flip transfer on to different temporary substrate and (d) deposit and etch-back copper to complete fabrication.*

between the U-shape and the ground strip (250 μm) were tuned to get better voltage standing wave ratio (VSWR).

The dimensions of the antenna can be significantly reduced through adding a capacitive load to the antenna [10], which can be accomplished by utilizing the thin polyimide substrate. The overlaid part of the backside rectangular coupling patch and the top rectangular patch was used as a loaded capacitor to reduce the size of the antenna. The capacitance between the metal strip on the top layer and the rectangular patch on the bottom layer was calculated to be 4.2 pF.

4.3. Antenna fabrication

Figure 4.2 describes the fabrication steps for building flexible WLAN antenna with schematic illustrations. The 127 μm thick polyimide film (Dupont Kapton HN) was cut using ultra-violet

laser (A-laser, FCT Assembly Inc.) to define the rectangular device shape and via-holes with accurate dimensions. Figure 4.2a shows the lamination of pre-cut polyimide film on a temporary polydimethylsiloxane (PDMS) coated glass substrate, which allowed utilization of the flat wafer based conventional micro-fabrication processing. 1 µm thick layer of copper was sputtered (Denton Discovery 24 RF/DC Sputter) thoroughly on the oxygen-plasma treated film, followed by copper etch-back process to form the square patch and ground plane of the antenna [Figure 4.2b]. The plasma treatment enhanced the adhesion between copper and the film. The isotropic sputtering of copper also coated the via-holes thoroughly. The patterned film was then delaminated and flipped transferred onto a different PDMS coated glass substrate for antenna patterning [Figure 4.2c]. Finally, the circuit pattern on the top layer of the antenna was formed with another sputtered copper etch-back process via photolithography [Figure 4.2d]. The completed antenna was then delaminated from the temporary glass substrate and an SMA connector (132255 end launch jack, Amphenol Connex) was soldered on to the device for measurement, as shown in Figure 4.3. With the SMA connector protected, a 10 µm thick Parylene C was coated using a chemical vapor deposition (CVD) process. Parylene C is a good biocompatible material to be used to isolate the

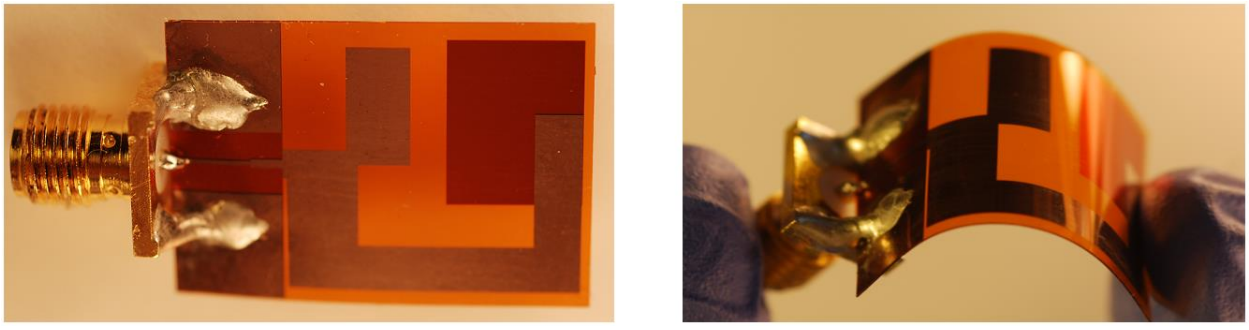

Figure 4.3. *Photographs of the fabricated antenna after Parylene C coating (left) and under bending condition (right).*

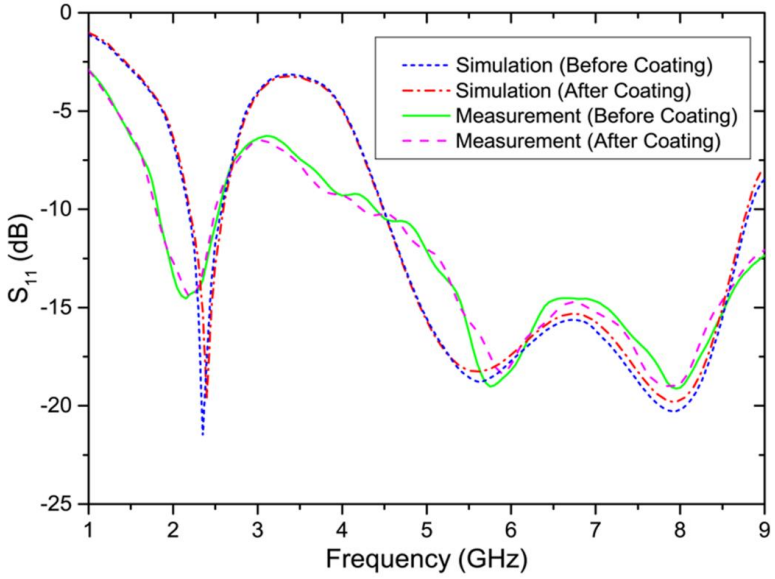

Figure 4.4. *Simulated and measured S_{11} of the antenna in air (free space) before coating and the same antenna coated with Parylene C.*

component from air or body fluid. The Parylene C coated antenna can be used as a promising implantable antenna which has a barrier layer to minimize oxygen contamination [11].

4.4. Antenna performance

The return loss, radiation patterns and gains of the antenna were measured in the Satimo spherical near field measurement system. Additionally, measured return loss and bandwidth of the antenna were compared with those of the simulated results. The effect of 10 µm Parylene C coating on the return loss of the proposed antenna is shown in Figure 4.4. There was little change of return loss when the antenna was coated with 10 µm of Parylene C layer as the dielectric constant of Parylene C (2.95) is close to the dielectric constant of polyimide (3.5) and the thickness of the Parylene C coating layer was very small compared to the thickness of the polyimide substrate. Figure 4.5 shows the measured radiation patterns for the operation bands of the coated antenna in

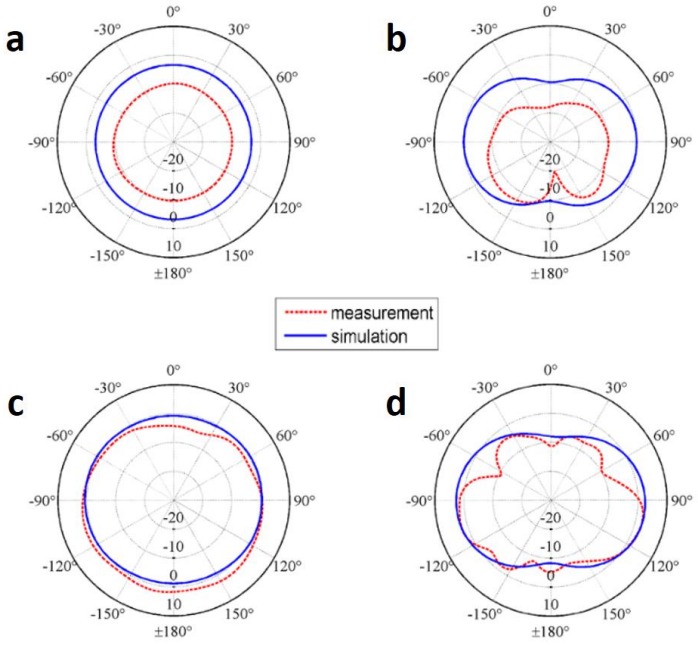

Figure 4.5. *Measured and simulated radiation patterns in air (free space) in XY- and YZ-planes at 2.4 and 5.8 GHz: (a) XY-plane at 2.4 GHz. (b) YZ-plane at 2.4 GHz. (c) XY-plane at 5.8 GHz. (d) YZ-plane at 5.8 GHz.*

the Satimo spherical near field measurement system. Omnidirectional properties of the patterns observed in the XY-plane confirm the monopole-like behavior of the antenna. The 2.4 and 5.8 GHz associated measured maximum radiation gains were -5.4 and 3.8 dBi, respectively.

The effects of bending on the return loss and the radiation performance of the antenna are also shown by measuring the antenna bent over polystyrene foam cylinders with diameters of 40 mm, 33 mm, and 25 mm. While the resonance frequency shift and return loss as a result of the bending was negligible as shown in Figure 4.6, noticeable change in the radiation patterns was observed as shown in Figure 4.7, which is attributed to the slight directional change of the antennas.

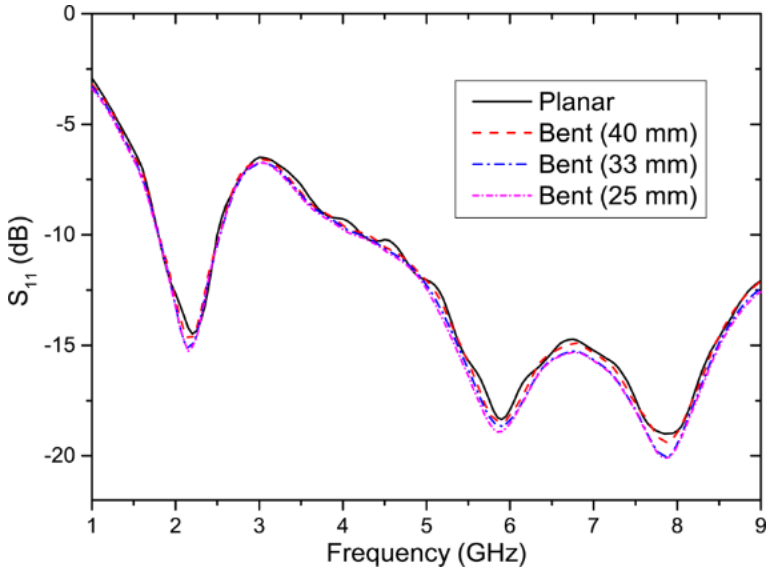

Figure 4.6. *Comparison of the S_{11} of the flat antenna and the same antenna bent on foam cylinders with different diameters.*

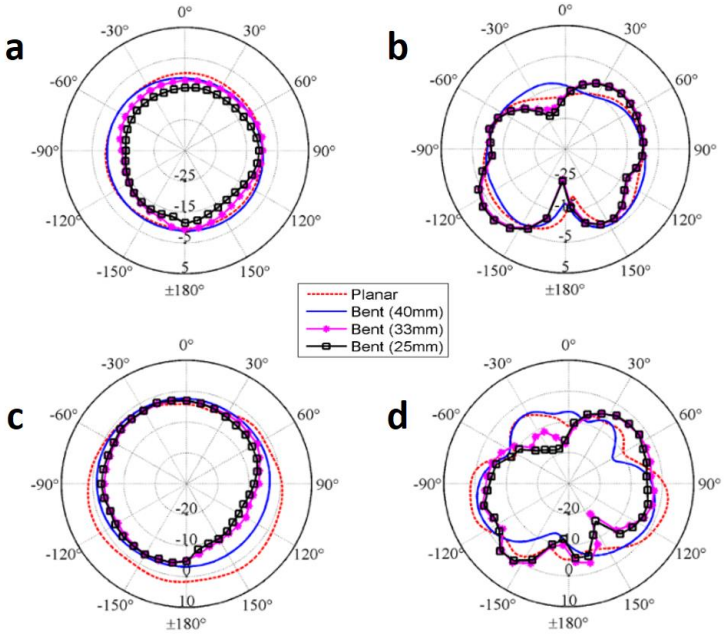

Figure 4.7. *Comparison of the radiation pattern of the flat antenna and the same antenna bent on the different cylinders at 2.4 GHz and 5.8 GHz (a) XY-plane at 2.4 GHz. (b) YZ-plane at 2.4 GHz. (c) XY-plane at 5.8 GHz. (d) YZ-plane at 5.8 GHz.*

4.5. Implantable antenna

Numerous measurement environments such as skin mimicking gel were developed in recent years. However the properties of the gel did not match well with the permittivity and conductivity of the real skin. Recently, porcine tissues were confirmed to best mimic the electrical properties of the human tissues at microwave frequencies. The permittivity, ε_r and the conductivity, σ of the porcine skin at 2.4 GHz are 38 and 1.46 S/m, respectively, which match closely to that of the human skin where ε_r and σ are 40 and 1.6 S/m, respectively [12].

To effectively tune our implantable antenna, we first studied the effects of the antenna performance when it was implanted as-is, as shown in Figure 4.8, where it was embedded under the porcine skin with a thickness of 1.4 mm, width of 63 mm, and length of 56 mm. Then, the S-parameters and the radiation patterns were measured to investigate the effects. As presented in Figure 4.9, we observed shifting of the operating frequency as well as significant drop in the radiation gains. The reasons for the operating frequency shift to lower frequency under the skin before tuning are attributed to the higher dielectric constant and the electrical conductivity of the pork tissue than that of the air [13]. Without tuning, the measured maximum radiation gains of the

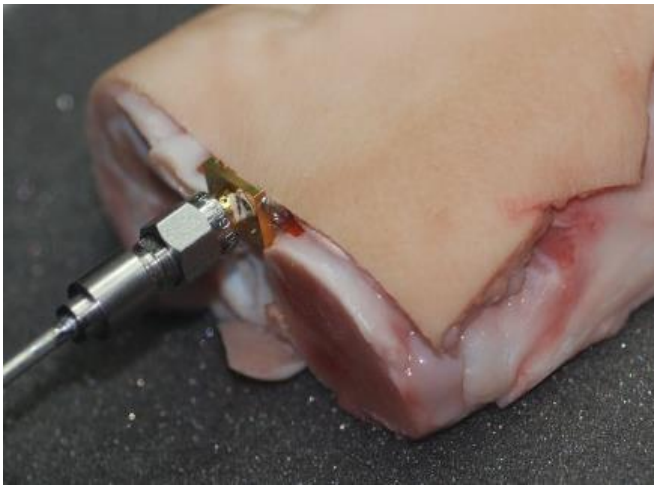

Figure 4.8. *Measurement setup for the antenna under the skin.*

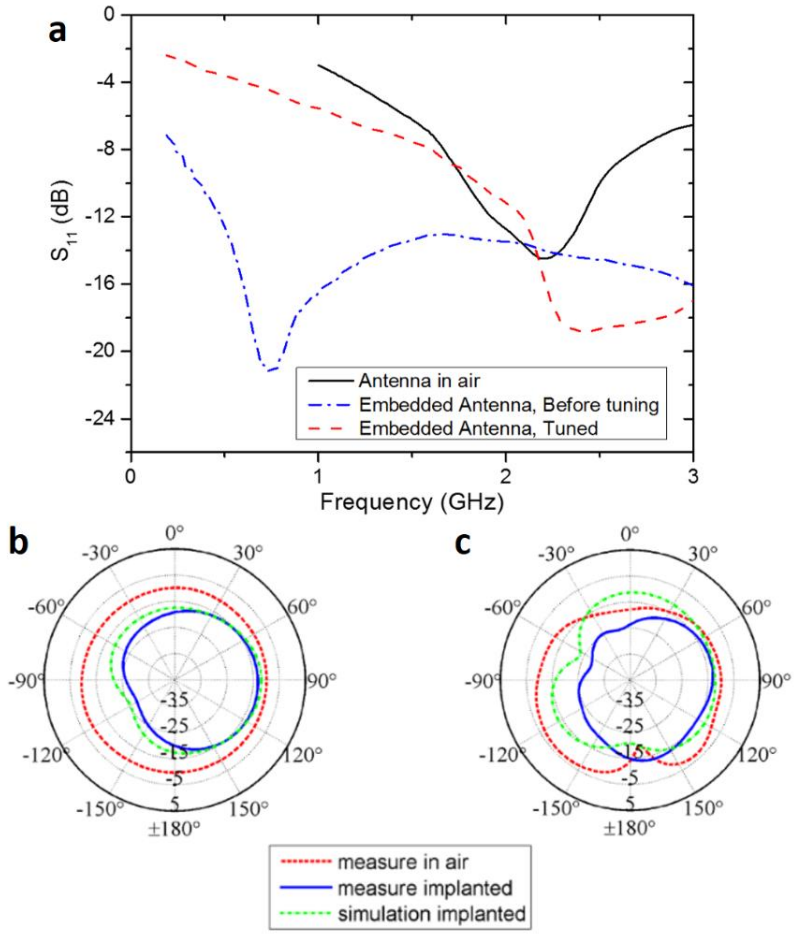

Figure 4.9. *Comparison of S_{11} of the antenna in air, and embedded in skin before and after tuning. Comparison of the radiation patterns measured in air, implanted under skin and simulated under skin before tuning at 2.4 GHz in (b) XY-plane and (c) YZ-plane.*

antenna under the skin was -12.9 dBi. Such poor maximum gain of the antenna under the skin is attributed to the high electrical conductivity which has adverse effect on the gain of the antenna. Finally, combined with the properties of the skin obtained from [12] and measurement analysis of the antenna under skin, the antenna was tuned via simulation. As a result, to increase the gain and shift the operating frequency back to WLAN frequency, the U-shape radiator which controls the lower frequency band was shortened as shown in Figure 4.10. The newly tuned antenna was

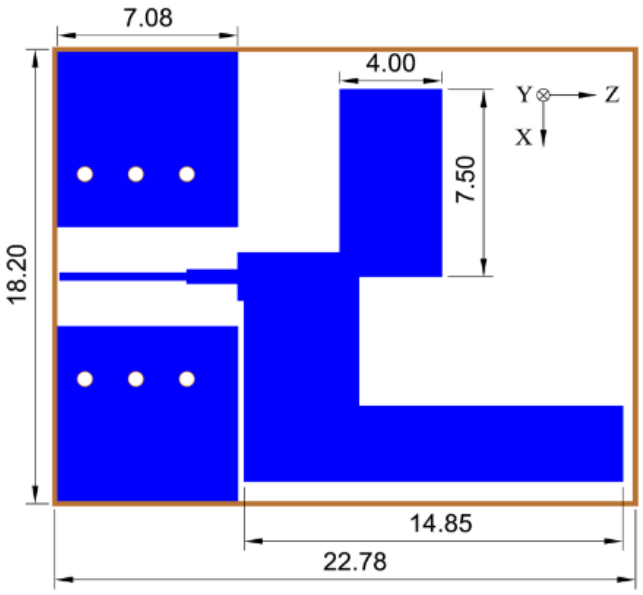

Figure 4.10. *Geometry and dimensions of tuned antenna (dimensions in mm).*

fabricated utilizing same approach presented in Figure 4.2. Figure 4.11 compares the measured and simulated results of the antenna before and after tuning. The measured S_{11} and maximum radiation gain of the tuned antenna under the skin has improved to -18.8 dB and 0.8 dBi, respectively at 2.4 GHz. While not demonstrated here, similar approach may also be used to tune the upper 5.8 GHz frequency, which shifted to lower frequency under implanted condition.

4.6. Conclusion

In this paper, a flexible Parylene C coated antenna with good electrical performance in WLAN frequency has been presented. The measured results have shown that the Parylene C coating and bending have negligible effects in the antenna performance. Furthermore, we have demonstrated fine tuning of the WLAN antenna for implantable applications. As the electrical parameters that vary among different types of tissues and animals propose challenges to designing antennas in

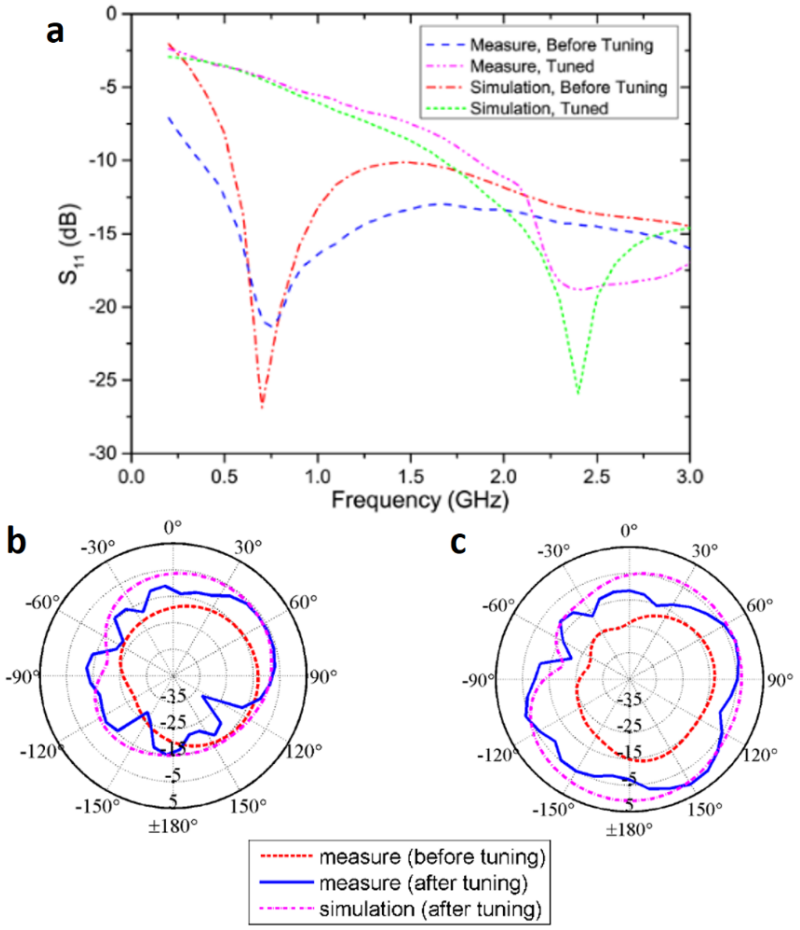

Figure 4.11. *(a) Comparison of measured and simulated S_{11} of the antenna embedded in skin before and after tuning. Comparison of the radiation patterns of the antenna measured implanted under skin before and after tuning and simulated after tuning at 2.4 GHz in (b) XY-plane and (c) YZ-plane.*

such media, this technique presents a simple approach in fabricating an implantable antenna. Study of the effect and impact from radiation and specific absorption rate (SAR) on the body remains one of the future tasks. The successful design migration from an antenna originally designed for operating in air to an implantable antenna can give some instructive hints for designing implantable antennas which could be transformed from numerous kinds of existing antennas which were

designed to operate in air.

4.7. Reference

[1] D.-H. Kim *et al*., "Dissolvable films of silk fibroin for ultrathin conformal bio-integrated electronics," *Nat. Mater.*, vol. 9, no. 6 pp. 511-517, June 2010.

[2] R.-H. Kim *et al*., "Materials and designs for wirelessly powered implantable light-emitting systems," *Small*, vol. 8, no. 18, pp. 2812-2818, Sept. 2012.

[3] G. J. Hayes, J.-H. So, A. Qusba, M. D. Dickey, and G. Lazzi, "Flexible liquid metal alloy (EGaIn) microstrip patch antenna," *IEEE Trans. Antennas Propag.*, vol. 60, no. 5, pp. 2151-2156, May 2012.

[4] C.-P. Lin, C.-H. Chang, Y. T. Cheng, and C. F. Jou, "Development of a flexible SU-8/PDMS-based antenna," *IEEE Antennas Wireless Propag. Lett.*, vol. 10, pp. 1108-1111, 2011.

[5] H. R. Khaleel, H. M. Al-Rizzo, D. G. Rucker, and S. Mohan, "A compact polyimide-based UWB antenna for flexible electronics," *IEEE Antennas Wireless Propag. Lett.*, vol. 11, pp. 564-567, 2012.

[6] T. Kellomäki and W. G. Whittow, "Bendable plaster antenna for 2.45 GHz applications," in *Proc. LAPC*, 2009, pp. 453-456.

[7] Y. Qiu *et al*., "Compact parylene-c-coated flexible antenna for WLAN and upper-band UWB applications," *Electron. Lett.*, vol. 50, no. 24, pp. 1782-1784, Nov. 2014.

[8] A. Kiourti, and K. S. Nikita, "A Review of implantable patch antennas for biomedical

telemetry: challenges and solutions," *IEEE Antennas Propag. Mag.*, vol. 54, no. 3, pp. 210-228, June 2012.

[9] DuPont. (2011, Apr.). "Dupont Kapton HN" [Online]. Available: http://www.dupont.com/content/dam/assets/products-and-services/membranes-films/assets/DEC-Kapton-HN-datasheet.pdf [Nov. 19, 2015]

[10] C. R. Rowell and R. D. Murch, "A capacitively loaded PIFA for compact mobile telephone handsets," *IEEE Trans. Antennas Propag.*, vol. 45, no. 5, pp. 837-842, May 1997.

[11] Y. S. Shin *et al*., "PDMS-based micro PCR chip with Parylene coating," *J. Micromech. Microeng.*, vol. 13, no. 5, pp. 768-774, Sept. 2003.

[12] M. Vallejo, J. Recas, P. G. del Valle, and J. L. Ayala, "Accurate human tissue characterization for energy-efficient wireless on-body communications," *Sensors*, vol. 13, no. 6, pp. 7546-7569, June 2013.

[13] M. S. Islam, K. P. Esselle, D. Bull, and P. M. Pilowsky, "Converting a wireless biotelemetry system to an implantable system through antenna redesign," *IEEE Trans. Microw. Theory Tech.*, vol. 62, no. 9, pp. 1890-1897, Sept. 2014.

CHAPTER 5
(Review) High-performance green semiconductor devices: Materials, designs, and fabrication

---

From large industrial computers to non-portable home appliances and finally to light-weight portable gadgets, the rapid evolution of electronics has facilitated our daily pursuits and increased our life comforts. However, these rapid advances have led to a significant decrease in the lifetime of consumer electronics. The serious environmental threat that comes from electronic waste not only involves materials like plastics and heavy metals, but also includes toxic materials like mercury, cadmium, arsenic, and lead, which can leak into the ground and contaminate the water we drink, the food we eat, and the animals that live around us. Furthermore, most electronics are comprised of non-renewable, non-biodegradable, and potentially toxic materials. Difficulties in recycling the increasing amount of electronic waste could eventually lead to permanent environmental pollution. As such, discarded electronics that can naturally degrade over time would reduce recycling challenges and minimize their threat to the environment.

This review provides a snapshot of the current developments and challenges of green electronics at the semiconductor device level. It looks at the developments that have been made in an effort to help reduce the accumulation of electronic waste by utilizing unconventional, biodegradable materials as components. While many semiconductors are classified as non-biodegradable, a few biodegradable semiconducting materials exist and are used as electrical components. This review begins with a discussion of biodegradable materials for electronics, followed by designs and processes for the manufacturing of green electronics using different techniques and designs. In the later sections of the review, various examples of biodegradable

electrical components, such as sensors, circuits, and batteries, that together can form a functional electronic device, are discussed and new applications using green electronics are reviewed.

5.1. Materials

An ideal green electronic chip would degrade at a controlled and reasonable rate relative to the lifetime of the chip, without generating biodegradable waste that has adverse effects on the environment. This would significantly reduce the accumulation of persistent solid waste and decrease the demand for e-waste landfill space. A working electronic chip is an integrated circuit consisting of multiple device components like diodes, transistors, inductors, and capacitors using electronic grade materials including semiconductors, metals, and insulators. These are typically based on inorganic materials and have dominated the electronics industry due to their excellent electrical and mechanical properties that provide great reliability, robustness, and performance. Inorganic materials are generally considered non-biodegradable because natural decomposition takes a very long time. However, a class of biodegradable and harmless inorganic materials exists which may be combined in various ways to create high-performance green electronic chips.

Inorganic Semiconductors

Inorganic semiconductors are known for their invariant physical and electrical properties that provide everlasting lifetimes for transistors and diodes in modern reliable electronic gadgets. Recent studies in dissolvable electronics have found completely the opposite behavior of these unchanging characteristics and revealed the transient behavior of some of the most commonly used inorganic semiconductors, such as Si, Ge, and ZnO. These materials were demonstrated to dissolve slowly over time and totally disappear in aqueous solution, groundwater, or biofluids [1-3]. In a

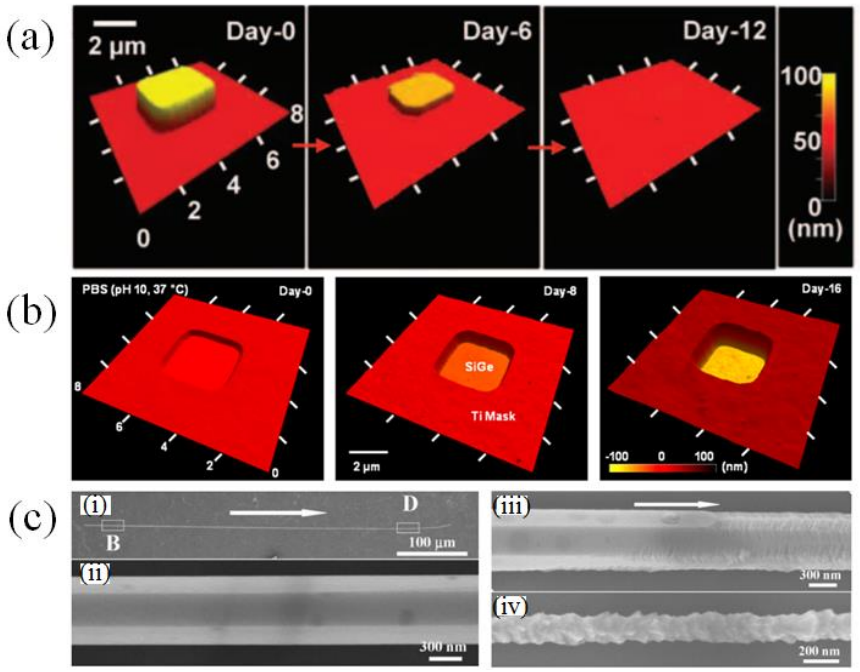

Figure 5.1. *Experimental studies of transient electronic materials and devices and corresponding theoretical analysis. (a) Atomic force microscope topographical images of a Si NM (initial dimensions: 3 mm × 3 mm × 70 nm) at various stages of hydrolysis in PBS at 37°C; adapted from [4]. Reprinted with permission from AAAS. (b) Series of AFM topographical images of SiGe (3 μm × 3 μm × 30 nm) at different stages of hydrolysis in a buffer solution (pH 10) at physiological temperature (37 °C) after day 0 (top left), day 8 (top right), and day 16 (bottom right), respectively; adapted with permission from [2]. Copyright (2015) American Chemical Society. (c) SEM images of an individual ZnO wire that has interacted with deionized water of pH ≈ 4.5–5.0. (i) Low-magnification SEM image of the ZnO wire. (ii, iii) High-magnification SEM images taken from the rectangular area B in (i) before and after interacting with deionized water, respectively. (iv) High-magnification image of the rectangular area D in (i) after about 30 min interaction; adapted from [3]. John Wiley & Sons. © 2006 WILEY-VCH Verlag GmbH & Co. KGaA, Weinheim.*

relatively short period of time, a fully functional integrated circuit based on such resorbable

semiconductors can disappear by hydrolysis in a well-controlled manner without generating toxic materials [4]. This is enabled by employing ultrathin sheets of inorganic semiconductors as the active materials. Whereas integrated circuits in relatively thick wafer dies (a small block of semiconductor) for conventional electronics would take several hundred years to fully dissolve (hence non-biodegradable), the dissolution process can be facilitated down to several days by utilizing semiconductors in the form of nanomembranes or nanowires. In Figure 5.1, the images of several nanoscale semiconductors, including Si nanomembranes, SiGe nanomembranes, and ZnO nanowires, in water-based solutions are shown at various dissolution stages. All of the semiconductors disappeared within a short time period. For instance, a block of Si nanomembrane (3 μm × 3 μm × 70 nm) completely dissolved in a phosphate buffer solution (PBS; pH of 7.4) within 12 days. Similar dissolution behaviors were observed for the other abovementioned semiconductors as well. The dissolution chemistry of these bioresorbable semiconductors are summarized below.

For Si:

$$Si + 4H_2O \rightarrow Si(OH)_4(aq) + 2H_2$$

For Ge:

$$Ge + O_2(aq) + H_2O \rightarrow H_2GeO_3(aq)$$

For ZnO:

$$ZnO(s) + 2\ OH^- \rightarrow ZnO_2^{\ 2-} + H_2O.$$

In all cases, the transient behavior of the inorganic materials heavily depended on the pH level and the temperature of the aqueous solution. Si dissolved at a faster rate with an increasing pH level. Also, the dissolution was faster at 37 °C compared to room temperature, suggesting that materials dissolve more rapidly at higher temperatures. The hydrolysis analysis showed varied

dissolution rates for different crystalline structures of materials as well. For instance, polycrystalline-Si dissolved at a slower rate than amorphous-Si, where the reduced density in a-Si expedited diffusion. The important take away in such dissolvable semiconductors is that they can all be dissolved in a well-defined time frame in a controlled fashion without generating toxic byproducts that affect the environment. By controlling the size of the nanocrystals, engineers can precisely control the lifetime of electronics. Such efforts would help reduce the amount of accumulated e-waste by allowing electronics to self-destruct and disappear after the suggested period of usage time.

Metals

Metals in electronics serve to connect the components from device to device to form an integrated circuit, as well as passive components like spiral inductors and transmission lines. In most electronics, non-biodegradable materials like gold, platinum, lead, and copper are used as electrical traces. Average home electronics contain several milligrams of such metals, which can accumulate extremely fast when multiplied across thousands of units and burden the environment as e-waste [5, 6]. While the key to minimizing this is to properly recycle and extract such metals before discarding, it is nearly impossible to do for the skyrocketing number of electronics discarded daily. For green electronics fabrication, it is important to seek biodegradable metals as counterparts. Before such massive e-waste significantly threatened the environment, biodegradable metals were investigated mostly for biomedical implants like cardiovascular applications. Most commonly used metals in such applications are Fe, Mg, and their alloys, which adapt to the human body and eventually dissolve over time [7]. The focus of biodegradable metals has been mainly on reducing the immune response from the contact tissues and minimizing the

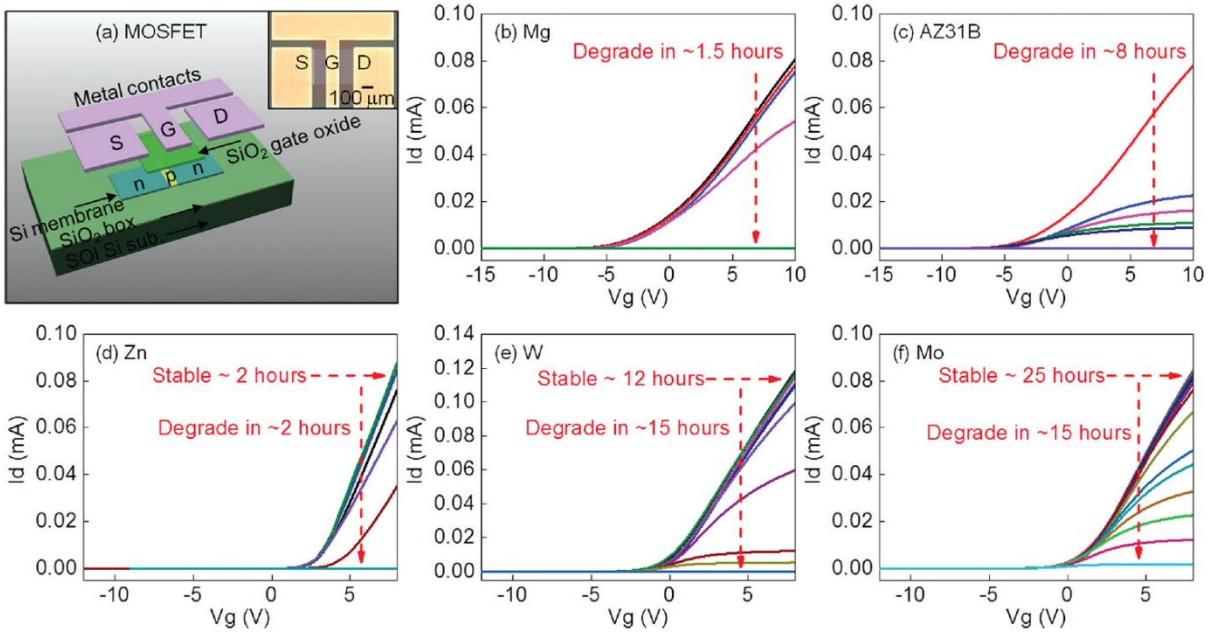

Figure 5.2. *(a) Geometry of an n-channel MOSFET, with a top view optical micrograph in the inset; (b)–(f) functional degradation of n-channel MOSFETs, as evaluated through measurements of the drain current (I_d) as a function of gate voltage (V_g) for a drain bias (V_d) of 0.2 V, with transient metal contacts: Mg, AZ31B Mg alloy, Zn, W, and Mo; adapted from [9]. John Wiley & Sons. © 2013 WILEY-VCH Verlag GmbH & Co. KGaA, Weinheim.*

corrosion of metallic biomaterials, rather than on the electrical properties [8]. An ideal metal for electronics would possess high carrier mobility, low resistance, high thermal conductivity, excellent mechanical properties, and corrosion resistance to maximize the performance and reliability of the integrated circuit. For biodegradable metals, the changes in electrical properties as the metals degrade are the most important parameters to consider. To investigate the ideal metals for dissolvable electronics, Yin *et al.* analyzed a list of biodegradable metals for electronics applications [9]. These metals included Mg, AZ31B Mg alloy, Zn, Fe, W, and Mo, which can all dissolve in an aqueous solution in a well-controlled manner. Changes in electrical properties were

measured and represented as electrical dissolution rates (EDR), which converted changes in electrical resistance to an effective thickness h, according to $R = R_0h_0/h$ (where R_0 and h_0 are the initial electric resistance and initial thickness, respectively). As these dissolvable metals, along with dissolvable electronic components, are useful for implantable applications as well, the study also focused on the EDR behavior at body temperature. Per this study, (i) Mg, AZ31B Mg alloy, and Zn had EDRs that were much higher than those of W, Mo, and Fe; (ii) the EDRs of Mg, Mg alloy, and Zn increased in salt solutions; and (iii) the EDRs increased with body temperature (between RT and 37 °C) for W, Mo, and Fe, but not significantly for Mg, AZ31B Mg alloy, and Zn. Finally, these dissolvable metals were tested on a thin film MOSFET as electrical contacts as shown in Figure 5.2. As a result, transistors with Mg, AZ31B alloy, and Zn contacts ceased function within 8 hours, and those with W and Mo contacts ceased function after 12 hours and 25 hours, respectively. This study established significant guidelines for metals towards maximizing the performances of green electronics that disappear. Further studies of such interconnects for high-speed applications would assure that such metals can also be used for microwave frequency electronics, which are essential for wireless mobile electronics.

Insulators

Hydrolysis also occurs in common dielectric materials, such as silicon oxides (SiO_x), silicon nitrides (SiN_x), and magnesium oxides (MgO) [4, 10]. These dielectrics have widespread usage in electronic devices for gate and interlayer dielectrics and passivation layers, as they are thermodynamically stable in contact with Si. For Si-based MOSFETs, silicon dioxide (SiO_2) is the preferred material as it is used to produce high-performance devices that incorporate gate dielectrics formed by thermal oxidation. These thermally grown oxides yield exceptional interface

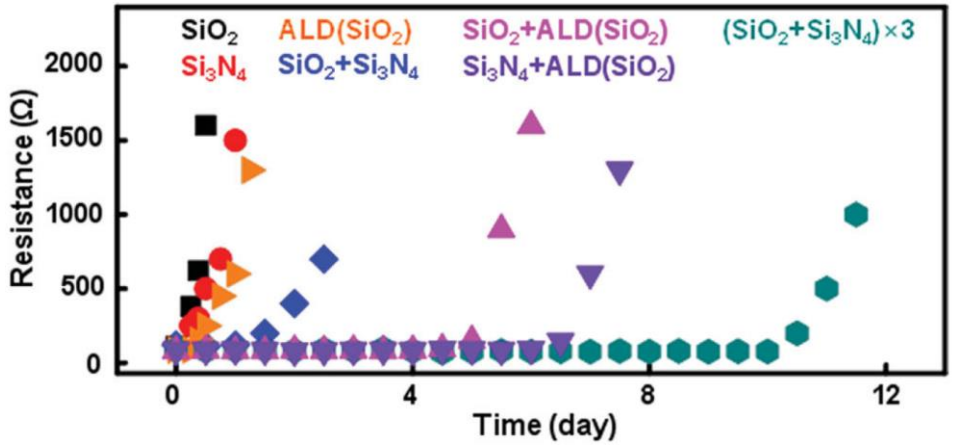

Figure 5.3. *Measurements of changes in resistance of Mg traces (≈300 nm thick) encapsulated with different materials and thicknesses while immersed in deionized (DI) water at room temperature. A single layer of PECVD SiO_2 (black, 1 μm), PECVD-LF Si_3N_4 (red, 1 μm), and ALD SiO_2 (orange, 20 nm), a double layer of PECVD SiO_2/PECVD-LF Si_3N_4 (blue, 500/500 nm), PECVD SiO_2/ALD SiO_2 (magenta, 500/20 nm), PECVD-LF Si_3N_4/ALD SiO_2 (purple, 500/20 nm), and a triple layer of PECVD SiO_2/PECVD-LF Si_3N_4 (Cyan, 200/200/200/200/100/ 100 nm) were used for the encapsulation; adapted from [10]. John Wiley & Sons. © 2013 WILEY-VCH Verlag GmbH & Co. KGaA, Weinheim.*

qualities between silicon and the oxide, and they have a lower defect density than any other known gate dielectrics for Si-based MOSFETs [11, 12]. Nitrides are also appealing for high-performance devices as they can induce stress to uniaxially strain the channels in MOSFETs for mobility enhancement. Although it is less appealing as a dielectric, MgO is also a good candidate for gate dielectrics due to its sharp interface with Si, as well as its high-κ and wide bandgap for low leakage [13]. Studies of dissolution kinetics on these dielectric materials suggest that these too can dissolve in aqueous solutions, following the same trend as the abovementioned inorganic semiconductors

and metals. The dissolution rate was the fastest for MgO, followed by plasma-enhanced chemical-vapor-deposited SiO_2 and Si_3N_4. The dissolution rate for SiO_2 and Si_3N_4 depended heavily on the method of deposition. Figure 5.3 summarizes the dissolution rate curves of all three materials by comparing the changes in resistance of Mg traces encapsulated in different materials and thicknesses.

A complete set of biodegradable electronics-grade inorganic materials that dissolve in aqueous solutions have been reviewed, suggesting that high-performance electronic devices that can fully dissolve over time can be fabricated using the materials summarized in this section. This set of materials can be mixed and optimized to yield important devices, such as diodes, transistors, capacitors, and inductors, all of which form the basis of fully dissolvable green electronics [14]. While biodegradable semiconductors, metals, and insulators are suitable for fully dissolving zero-waste consumer electronics, other high-performance non-dissolving or toxic semiconductors like GaAs, GaN, and InP must be used to create high-speed and high-power circuits. As it is unavoidable to use such semiconductors, designs that use a minimal amount of semiconductor materials can be beneficial for reducing the accumulated waste and also save material costs. For instance, the elimination of the bottom handling wafer by transfer printing thin film high-speed or high-power transistors and diodes onto a biodegradable substrate would greatly help minimize environmental pollution.

5.2. Substrates

Integrated circuit fabrication undergoes many microfabrication process steps involving extreme conditions such as high-temperature doping and oxidation, strong acidic and basic solutions-based chemical treatments, and high-speed stream of plasma etching, as well as dicing

and packaging. These abrasive processes require semiconductor chips to have sufficiently thick supporting substrates, defined by the mechanical strength of the material, to prevent them from cracking during handling. The thickness of the substrate can range from tens to hundreds of microns, whereas the thickness of the top active layer only ranges from sub-microns to a couple of microns. In most cases, the substrate is the same material as the active layer and is considered waste from an environmental standpoint. Replacing such non-biodegradable substrates with biodegradable and ecofriendly materials would, therefore, enormously decrease the amount of semiconductor material used in the integrated circuit. In this section, various types of substrates used for green electronic chips are reviewed. While choosing the most ecofriendly substrate is the key, it is also important to consider the electrical and mechanical characteristics, which should minimally affect the performance of the electrical components printed on top.

Silk

Silk film has been used as a substrate for dissolvable electronics because it is mechanically flexible and robust, biocompatible, and bioresorbable [4, 14-17]. It is also appealing as the dissolution process can be controlled at a programmable rate and is compatible with aqueous processing [18, 19]. Silkworm silk is largely used in silk thin film substrates. In a silk fibroin-based film manufacturing process developed by Perry *et al.*, the purification of Bombyx mori cocoons was achieved by boiling the cocoons in an aqueous solution of sodium carbonate [19]. After rinsing and drying, the remaining fibroin was dissolved in lithium bromide solution, which was later removed by a subsequent dialysis process. Centrifugation and microfiltration were used to produce 8-10% silk fibroin with high quality and stability. Casting the solution on a flat substrate and drying it in air could yield uniform silk films. These films are excellent substrates for

implantable and dissolvable electronics as the decomposition of the material demonstrated as transplanted scaffolds has been proven to be biocompatible for tissues and nerves [20].

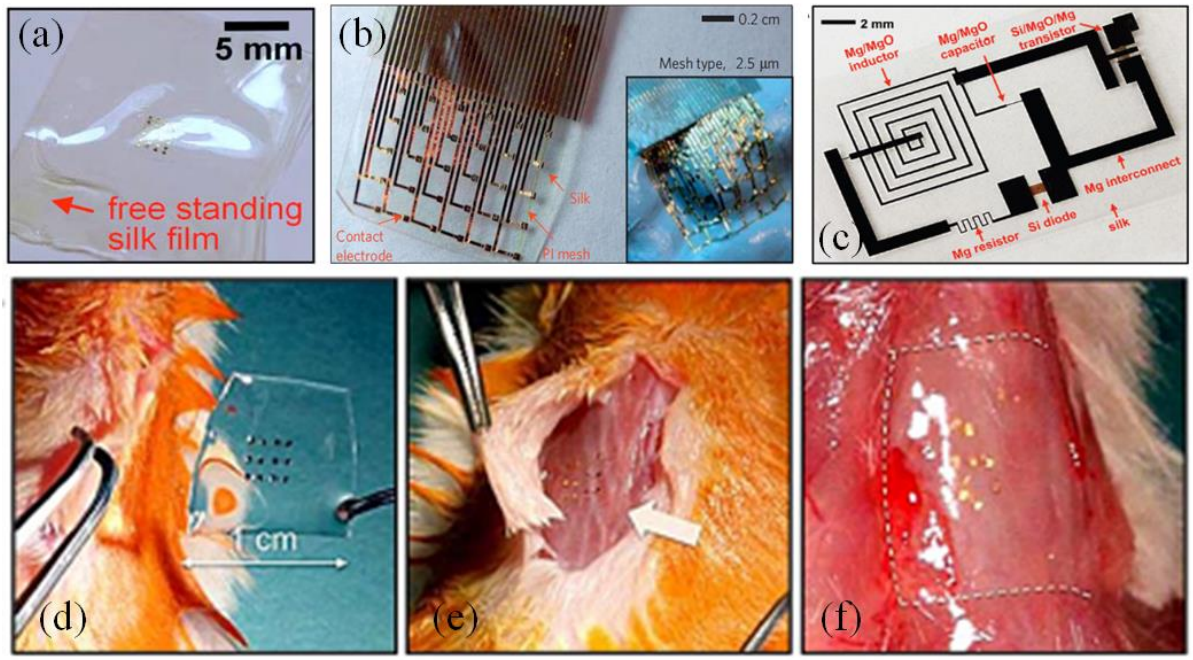

Figure 5.4. *(a) Ultrathin Si devices on a flexible silk substrate; reprinted from [15]. With the permission of AIP publishing. (b) Image of an electrode array with a mesh design on a dissolvable silk substrate. The arrows indicate struts in the mesh that help stabilize the Au interconnects after dissolution of the silk. The inset illustrates the high degree of conformal contact that can be achieved on the brain model once the silk substrate has been dissolved; adapted by permission from Macmillan Publishers Ltd: [Nature Materials] [17]. Copyright (2010). (c) Image of a device that includes transistors, diodes, inductors, capacitors, and resistors, with interconnects and interlayer dielectrics, all on a thin silk substrate; adapted from [4]. Reprinted with permission from AAAS. Images of the dissolution process of an implanted device on a silk substrate in mice (d) before implantation, (e) shortly after implantation, and (f) two weeks after implantation; reprinted from [15], with the permission of AIP Publishing.*

Figure 5.4a–c shows examples of simple electronic devices built on silk film, such as Si transistors, electrophysiological recording electrodes, and dissolvable electronic systems [4, 15, 17]. The degradation process of the silk film is also demonstrated as shown in Figure 5.4d–f, where Si devices encapsulated with polyimide on silk film were implanted in mice and evaluated after several days. Figure 5.4d shows the device before implantation, Figure 5.4e shows the device shortly after implantation, and Figure 5.4f shows the complete dissolution of silk with only the devices remaining after two weeks. This process consists of the dissolution of silk in water and proteolytic degradation that is completely biocompatible to the contact tissues [21]. Moreover, the dissolution rate can be controlled by changing the drying rate of Bombyx mori silk solutions [22], by reducing β-sheet content [23], and by treating the film with ethanol [17]. Their excellent degradation capability and biocompatibility make silk-based electronics promising candidates for green electronics. Further electrical analysis of the films for high-performance electronics applications, such as electrical breakdown and dielectric and microwave loss properties, are desirable for reliable electronics operations.

Cellulose and Paper

Cellulose nanofiber (CNF) film has attracted great attention due to its biodegradable nature and large abundancy and has been used in flexible electronics as a substrate for degradable applications [24-26]. Derived from natural fibers such as woods and plants, CNF films can be made like plastic films and have excellent mechanical properties and high transparencies. Unlike plastics, however, these films can be discarded without sophisticated recycling processes as fungi will eat away the fibers. CNF film is first produced from wood, degraded via a fungal biodegradation process on disposal, and sent back to the woods without adverse environmental

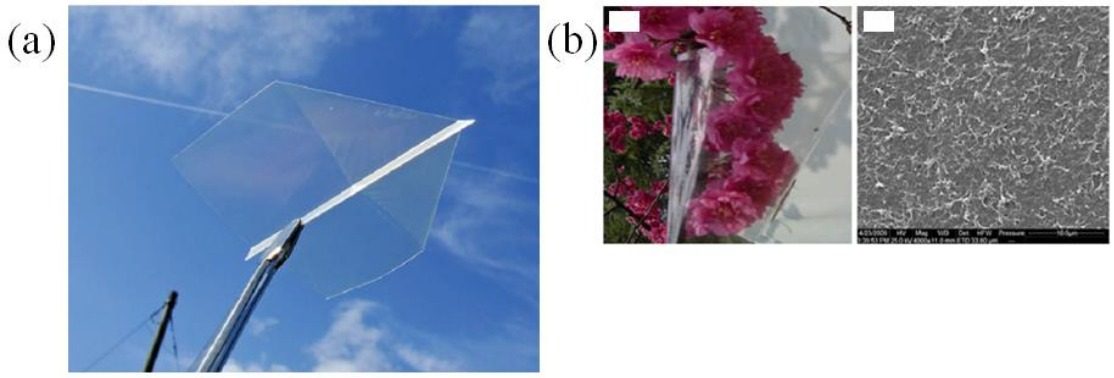

Figure 5.5. *Cellulose nanofiber papers. (a) An oven-dried cellulose nanofiber sheet that is as foldable as conventional paper; adapted from [27]. John Wiley & Sons. Copyright © 2009 WILEY-VCH Verlag GmbH & Co. KGaA, Weinheim. (b) A photograph of cellulose film regenerated from NaOH/urea/zincate solution (left) and an SEM image of the surface (right); adapted from [28]. (2011) © Springer Science+Business Media B.V. 2011. With permission of Springer.*

effects. Numerous methods to produce such biodegradable cellulose nanofiber films have been demonstrated. For instance, Nogi *et al.* reported optically transparent nanofiber paper [27]. They started by removing lignin and hemicelluloses in wood flour, followed by grounding the wood flour in a water-swollen condition. Freeze-drying and mechanically compressing under vacuum were used to obtain the sheet of nanofiber paper without air and voids. To make the sheet transparent, different methods were tested, such as polishing using emery paper, laminating optically transparent plastics, depositing transparent resins, and drawing transparent patterns on the paper. The obtained cellulose nanofiber paper is highly transparent and foldable as shown in Figure 5.5a. Different approaches were also used to produce transparent cellulose films by Yang *et al.* [28]. Dried cellulose was first dispersed in pre-cooled NaOH/urea/ZnO aqueous solution followed by degassing via centrifuging. To obtain the transparent films, the dope was casted on a

glass plate and coagulated with a H_2SO_4 aqueous solution. Finally, the films were washed with water, followed by air-drying. Optical and scanning electron microscope (SEM) images of the transparent cellulose film are shown in Figure 5.5b.

Polymers

Biodegradable polymers like poly lactic-co-glycolic acid (PLGA), a copolymer of poly lactic acid (PLA) and poly glycolic acid (PGA), PLA, polycaprolactone (PCL), and poly(1,8-octanediol-co-citrate) (POC) have also been used as substrates for inorganic semiconductor devices [29, 30]. These substrates have been a common choice for biodegradable organic electronics, drug release carriers, and implantable tissue engineering scaffolds [31-37]. The ability to integrate high-performance electronics with such commonly used biodegradable polymers could expand the capabilities of such applications. PLGA has been one of the most popular biodegradable polymers as its properties, such as dissolution rate and hydrophobicity, can be tuned by varying the ratio between PLA and PGA. Nevertheless, PLGA likes to swell in moisture and can cause fracture and disintegration of the printed electronics, which can lead to malfunctioning of the device at any time. PCL is also preferred as it is relatively easy to cast and shape. Also, as one of the earliest biodegradable polymers studied, it is widely available from commercial markets. Different from other polymers, POC is an elastomer that can stretch with strains up to 30% with a linear elastic mechanical response [30]. This could yield biodegradable stretchable electronics using inorganic electronic device layouts with device islands connected by serpentine or noncoplanar mesh interconnects [38]. Optical images of inorganic semiconductor devices fabricated on PLGA, PCL, PLA, and POC are shown in Figure 5.6.

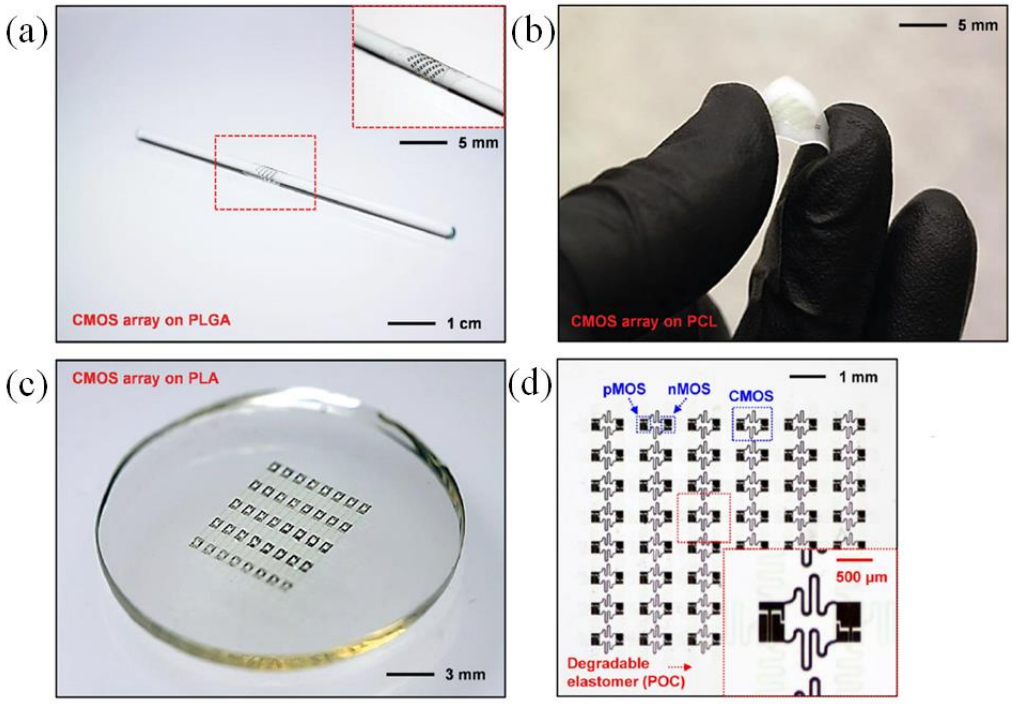

Figure 5.6. *Transient electronic systems on biodegradable polymers. (a) Photograph of an array of transient CMOS inverters on a thin PLGA substrate wrapped onto a cylindrical glass rod, with a magnified image in the inset. (b) Image of a transient device on a PCL substrate, in a bent configuration. (c) An array of transient CMOS inverters on a PLA substrate; adapted from [29]. John Wiley & Sons. © 2014 WILEY-VCH Verlag GmbH & Co. KGaA, Weinheim. (d) An array of transient CMOS inverters interconnected in a filamentary serpentine (FS) mesh on a POC substrate; adapted with permission from [30]. Copyright (2015) American Chemical Society.*

Thus, different classes of biodegradable materials exist which can be used to build biodegradable electronic systems. Basic substrate property requirements for high-performance electronics using inorganic materials include a smooth surface roughness, good mechanical strength, low thermal expansion, good thermal stability, and process capability to withstand solvents, acids, base, water, etc. RF electronics would demand additional requirements, such as

low RF loss, high dielectric κ, high breakdown, and high thermal conductivity. Typically, a biodegradable substrate does not possess all of these requirements, and this poses limitations in performance for the devices despite using inorganic semiconductors as active materials. Continuous material science efforts are being made to meet such requirements and to generate a substrate that will be perfect for green electronics. With available green device layers and substrates, different combinations of high-performance green electronic chips can be built.

5.3. Design and Fabrication of High-Performance Green Electronics

In this section, fabrication process steps toward building various green electronic chips that either degrade fully or partially are discussed. The generic fabrication process of obtaining single-crystal semiconductor thin films begins with selective wet etching of the sacrificial layers underneath the nanomembrane on the host wafer. For instance, a freestanding Si nanomembrane is obtained from a silicon-on-insulator (SOI) wafer by removing the buried oxide (BOX) layer using concentrated hydrofluoric acids (HF). Obtaining thin-films of other semiconductors generally follows a similar process where Ge thin film is obtained from a GeOI wafer, and a GaAs thin film is obtained from GaAs grown on a sacrificial AlGaAs layer. This unique process not only yields rigid host wafers capable of active layer re-growth, but also high-performance single crystal semiconductor thin films that are mechanically flexible for operational features unavailable with bulk materials, as the extremely small thicknesses of nanomembranes compared to bulk materials allow flexural rigidities that are many orders lower [39]. The disadvantage of this process is that any material vulnerable to sacrificial layer etchant is unavailable for use. Thermally grown SiO_2, which is an excellent dielectric insulator for Si, cannot be utilized as it would etch away in HF solution during the sacrificial layer undercut. Moreover, thermally growing SiO_2 after the release

induces significant mechanical stress on the nanomembranes. Dielectrics deposited using chemical

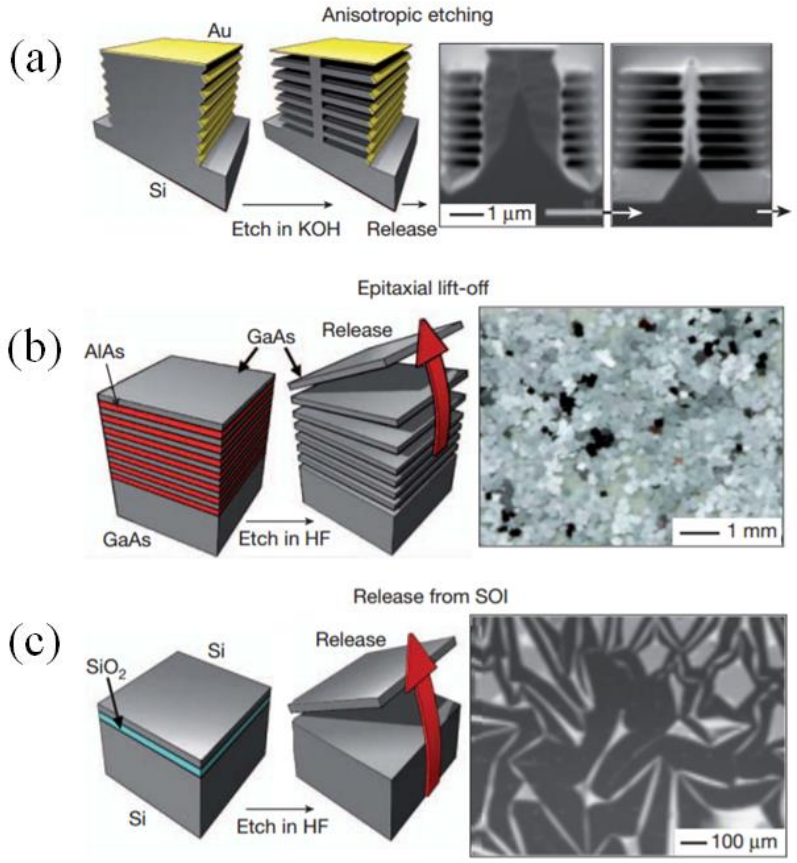

Figure 5.7. *(a) Process for generating multilayer stacks of silicon NMs from a bulk wafer by anisotropic etching. Patterned features of etch resist (gold) on the structured sidewalls of vertically etched trenches allow access of an anisotropic wet chemical etchant only to certain regions of the silicon. (b) Epitaxial multilayer assembly of GaAs and aluminum arsenide (AlAs) grown on a GaAs wafer. Etching vertically through the thickness of the stack, and then immersing the structure in hydrofluoric acid, leads to the selective removal of the AlAs layers. Complete undercut etching releases large numbers of GaAs NMs. (c) Release of a silicon NM from a SOI wafer. Etching vertically through the top silicon layer exposes the underlying SiO_2 layer, allowing its removal by etching in hydrofluoric acid; adapted by permission from Macmillan Publishers Ltd: [Nature] [39], Copyright (2011).*

vapor deposition, evaporated deposition, or atomic layer deposition are instead substituted for insulators and passivation layers. Novel approaches to overcome this have also been proposed, where high-performance thin film MO SFETs utilizing thermal oxides and (100) oriented thin Si were fabricated on SOIs that have supporting wafers with (111) orientation. This allows for the release of top thin films using tetramethyl ammonium hydroxide (TMAH) solutions for anisotropic wet etching of the bottom supporting substrate, instead of using HF solutions to undercut etch the BOX layer [11, 16]. Other developing techniques include xenon difluoride (XeF_2) gas-based isotropic etching for the release of top films from bulk Si wafers. These common processes are summarized using the schematic illustrations in Figure 5.7, all of which may be applied to produce high-performance semiconductor thin films for green electronic chips.

Such released thin film semiconductor layers may be subsequently transfer printed onto foreign substrates. Elastomeric stamps made using commercially available polydimethylsiloxane (PDMS) rubber have adhesion forces that lead to conformal contact with solid objects, which are used to pick up semiconductor thin films. These picked-up films are either transfer printed on a dry surface using kinetic control of adhesion or on an adhesive coated substrate [40]. Common flexible substrates for non-biodegradable applications are plastic films that can withstand moderately high processing temperatures (~300 °C) and chemical solutions like photoresists, solvents, acids, and bases, allowing post-transfer microfabrication process steps like photo-lithography, deposition, and etching. Different from generic flexible electronics fabrication, however, further microfabrication processing of the transferred semiconductor thin films on biodegradable substrates is highly limited, as they are typically vulnerable to high-temperatures and wet chemicals.

The first demonstration of Si transistors on a biodegradable substrate was fabricated on a thin

sheet of polyimide carrier substrate and transferred to a silk film, as shown in Figure 5.8 [15]. First, a releasable polyimide layer was laid on a temporary Si substrate using poly(methyl methacrylate) (PMMA) as the sacrificial layer. Such a format allows for planar conventional microfabrication processes to complete the Si transistor fabrication. Finally, the sacrificial PMMA layer was

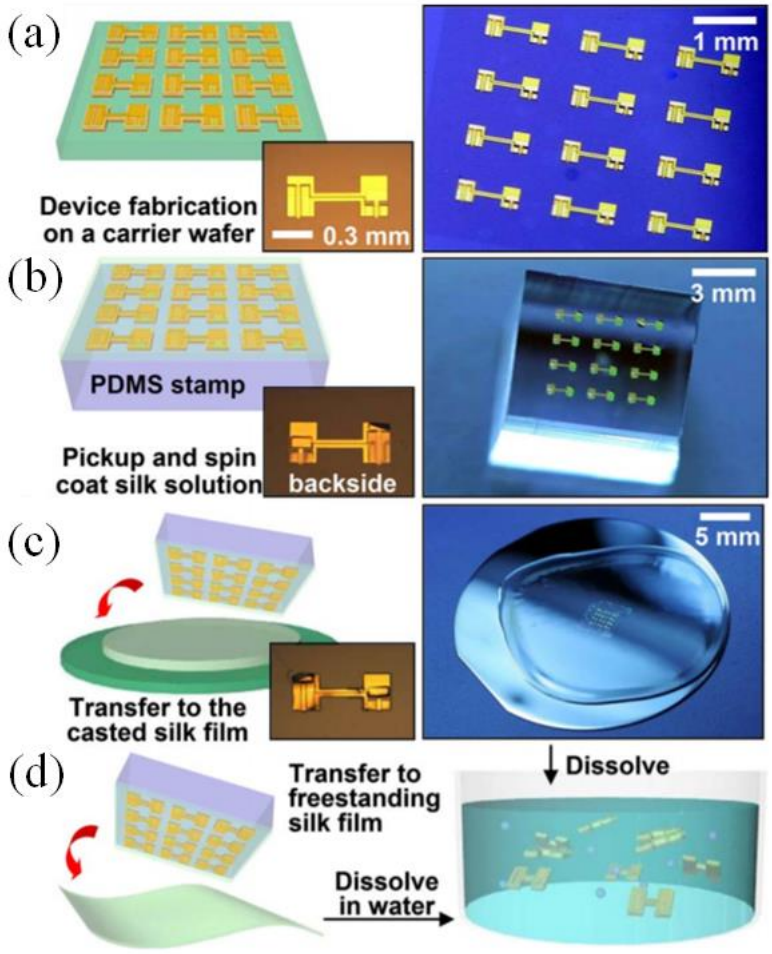

Figure 5.8. *Schematic diagram (left), corresponding high resolution image (right), and micro-scope image (inset) of (a) ultrathin devices on a carrier wafer, (b) devices lifted onto the surface of a PDMS stamp, and (c) process for transfer printing onto a silk film cast on a silicon wafer. (d) Schematic diagram of transfer printing onto a freestanding silk film (left) and dissolution (right); reprinted from [15], with the permission of AIP Publishing.*

dissolved in boiling acetone to release the top transistors packaged in polyimide and transfer printed onto a silk substrate using a large slab of elastomer stamp. From the transfer characteristics and IV characteristics of the Si transistors on silk thin film before and after dissolution, the extracted electron mobility and threshold voltage changed from ~500 cm^2/Vs and ~0.2 V to ~440 cm^2/Vs and ~0.5 V before and after dissolution of the silk thin film, respectively. The on/off ratio remained as ~10^4 after dissolution of the silk thin film substrate. The modest change in performance shows the possibility of combining implantable biomedical devices with high performance flexible electronics.

Several methods were developed to minimize post-transfer processing steps and create fully biodegradable electronics by removing the polyimide layer. In one example using silk as the substrate, a high resolution shadow mask was adapted to eliminate photolithography steps. Metals and dielectrics were deposited on transfer-printed Si nanomembrane blocks through patterned stencil masks to complete the integrated circuit [4]. A photograph of the transient Si transistor and diode, along with a Mg-based simple circuit fabricated using this method, are shown in Figure 5.4c.

To yield a more complex circuit based on high-performance CMOS, photolithography processes are inevitable. Similar to the polyimide carrier substrate method, the entire circuitry was fabricated on a temporary diluted polyimide substrate, followed by picking the entire circuit using a large slab of elastomeric stamp. Removing the thin supporting polyimide using reactive ion etching prior to transfer printing the circuit onto biodegradable substrates yielded the transfer of high-performance circuitry consisting of only biodegradable materials [29]. This entire process is described in Figure 5.9. Since steps like deposition, etching, and lithographic patterning associated with fabrication of the electronic components are separated from the biodegradable substrates,

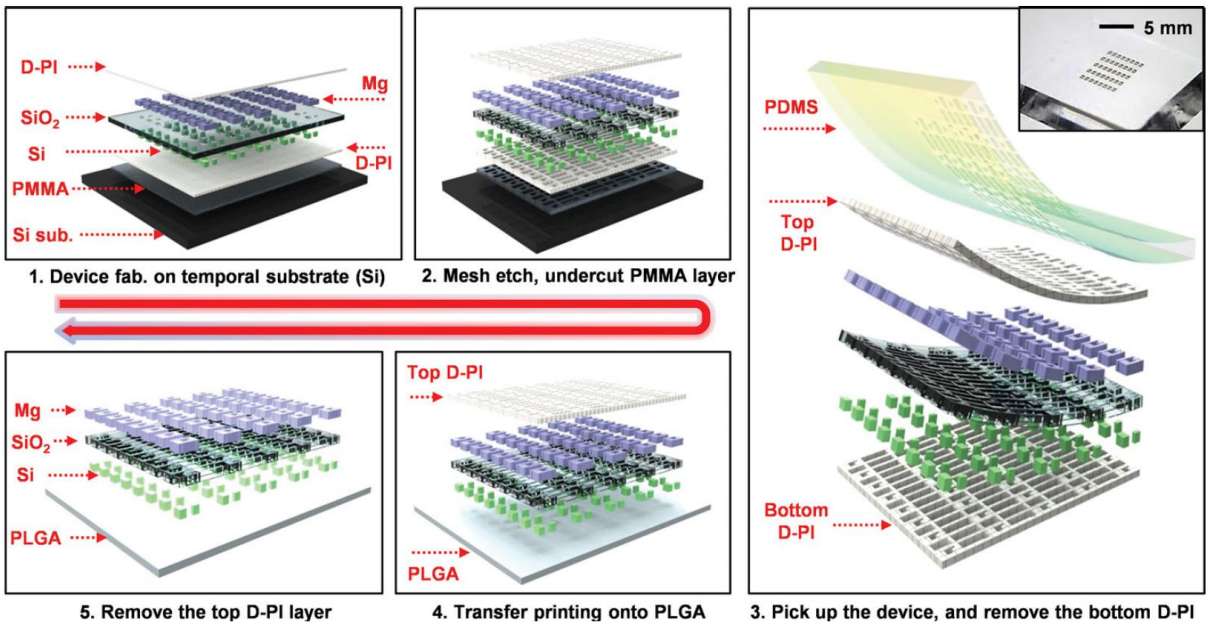

Figure 5.9. *(a) Schematic illustrations of key processes for fabricating transient complementary metal-oxide semiconductors (CMOS) on a carrier substrate (upper left). Defining a mesh type structure allows dissolution of the PMMA layer in boiling acetone at 90 °C to release the entire device (upper middle). Retrieving the released device onto a PDMS stamp (right, image of the device on PDMS in the inset) allows exposure and removal of the bottom layer of D-PI by reactive ion etching. Transfer printing onto a PLGA substrate (lower middle), and RIE etching of the top D-PI, completes the process (lower left); adapted from [29] John Wiley & Sons. © 2014 WILEY-VCH Verlag GmbH & Co. KGaA, Weinheim.*

transient electronic devices fabricated this way can be printed onto nearly any type of biodegradable substrate, whether it is highly susceptible to temperature, moisture, or solvents.

In another report on green electronics, partially biodegradable (99%) electronics chips that have comparable performances to state-of-the-art electronics were reported. Fabricating such high-performance devices requires compound semiconductors and process steps with extreme conditions. GaAs-based microwave electronic circuits, along with Si-based digital circuits, were

fabricated on a thin sheet of polyimide substrate and the completed circuitries were transfer printed onto biodegradable CNF substrates. GaAs-based transistors and Si-based transistors were transfer printed onto polyimide carrier substrates using elastomer stamps, followed by photolithography-based deposition and etching to add passive components and to complete the circuitry. A final passivation layer based on polyimide was spin-casted and cured to prevent toxic materials like arsenic from leaking out and also to prevent oxidation. And by removing the sacrificial PMMA layer beneath the packaged device, the released device could be printed onto a CNF substrate, with polymer adhesive in between for permanent bonding. The high-performance electronic devices fabricated using this technique included RF GaAs HBT, RF rectifier, and Si nanomembrane-based digital circuits on biodegradable CNF substrates [6]. The reported RF GaAs HBT could achieve a f_{max} of 6.9 GHz and a f_T of 37.5 GHz, and a full bridge rectifier based on a RF GaAs Schottky diode could achieve 2.43 mW of DC output power when input RF power was 21 dBm at 5.8 GHz, all on CNF paper. These reported transistors and circuits are adequate for wireless applications at microwave frequency range.

5.4. High-Performance Green Optoelectronics, Sensors, and Power Supplies

Similar techniques used for fabricating integrated circuits can be applied to create other electronic devices, such as optoelectronics, sensors, and power supplies. These are important electronic components that will benefit in performance from using inorganic semiconductors instead of organic ones.

Transient Optoelectronics

Various optoelectronic devices, such as solar cells and photodetectors for transient and

biodegradable applications, have been reported [4]. As described in Figure 5.10, solar cells and photodetectors were fabricated using the same materials and fabrication processes as that of the transient transistors and inverters described in [4]. With this approach, a biodegradable solar cell could achieve a fill factor of 66% and power conversion efficiencies of around 3% calculated from

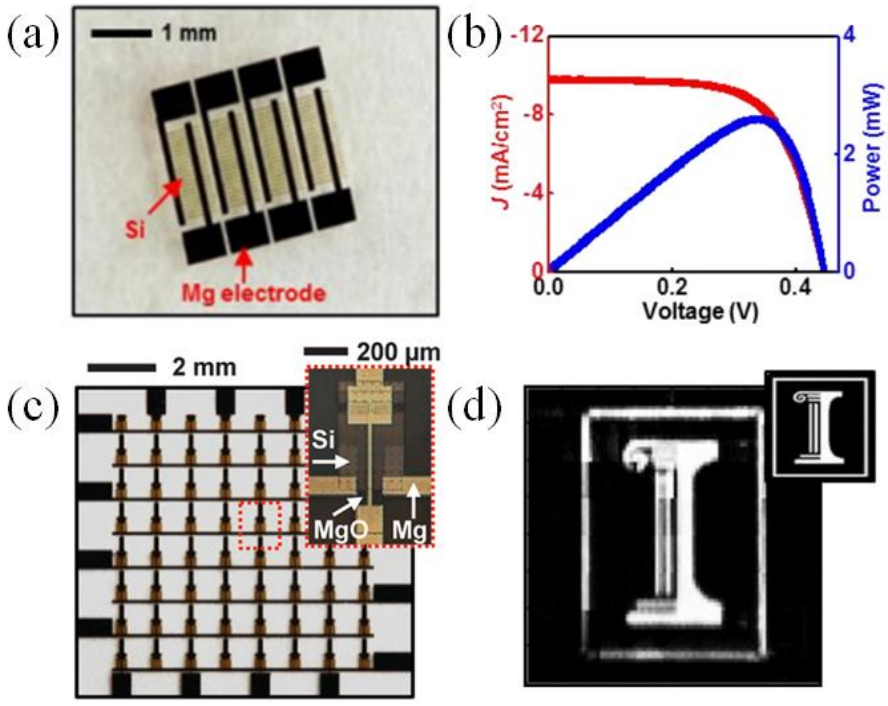

Figure 5.10. *Transient optoelectronics. (a) Image of solar cells that use ~3 μm thick bars of Si and Mg interconnects. (b) Current density and power measured from a representative device as a function of voltage when illuminated using light from a solar simulator. (c) An addressable array of Si NM photodetectors with blocking diodes. Mg serves as contact and interconnection electrodes and MgO as the dielectric. (d) Image of the letter 'I' obtained using a passive matrix, 8 × 8 array of transient photodetectors, operated in a mode in which the object is scanned and a collection of recorded images is combined to improve the effective resolution. Inset shows the original object pattern; adapted from [4]. Reprinted with permission from AAAS.*

the measured current density and output power. Also, a relatively clear image could be obtained using a transient array of photodetectors, as shown in Figure 5.10d. A Mg-based biodegradable circuit on a silk substrate utilizing a wireless RF power scavenger circuit to turn on a commercial LED was demonstrated as shown in Figure 5.11a [14]. Here, an input power of 8.5 mW was used to drive the LED. Also, a wirelessly powered blue LED on transient printed circuit boards using a RF power harvesting unit was demonstrated as shown in Figure 5.11b [41].

Bioresorbable Sensors

Sensors are one of the most important parts in biomedical systems. Several different types of biodegradable and transient sensors based on inorganic materials have been reported to measure different biological signals [4, 29, 30, 42, 43]. For instance, simple strain gauges based on Si

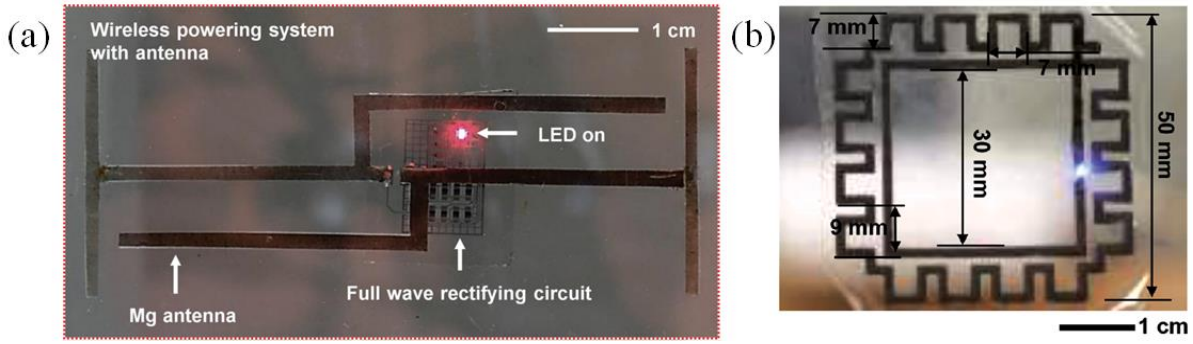

Figure 5.11. *Transient wireless scavengers. (a) Image of a full wave rectifying system powered wirelessly with an RF transmitter and a Mg receiving antenna; adapted from [14]. John Wiley & Sons. © 2013 WILEY-VCH Verlag GmbH & Co. KGaA, Weinheim. (b) A transient RF power harvesting circuit with a meander loop antenna formed using a screen-printed W paste. The blue LED attached to the antenna demonstrates wireless power harvesting with a half-wave rectification circuit; adapted from [41]. John Wiley & Sons. © 2014 WILEY-VCH Verlag GmbH & Co. KGaA, Weinheim.*

resistors, temperature sensors based on Si diodes, and Mg resistors on silk film were fabricated using the same technique described for transient transistors and diodes as shown in Figure 5.12a–c. The strain gauge achieved gauge factors of ~40, which is comparable to those of conventional devices. The Si diode-based temperature sensors showed a voltage–temperature slope of ~ –2.23 mV/°C and the Mg-based temperature sensors showed a resistance increasing slope of ~ –0.14 Ω/°C, both of which are useful for the accurate measurement of temperatures.

More advanced types of implantable sensors in bioresorbable formats to record neural signals were also demonstrated [42, 43]. One novel multifunctional device combined mechanical, physical, and chemical sensors in a bioresorbable format by printing the nanomembrane electronics on PLGA [42]. Furthermore, the device was bonded to a rigid silicon substrate with nanopores so that it could be inserted deep inside the brain to measure various signals. The nanoporous structure of silicon and the bioresorbable materials used for the sensors allowed complete dissolution of the

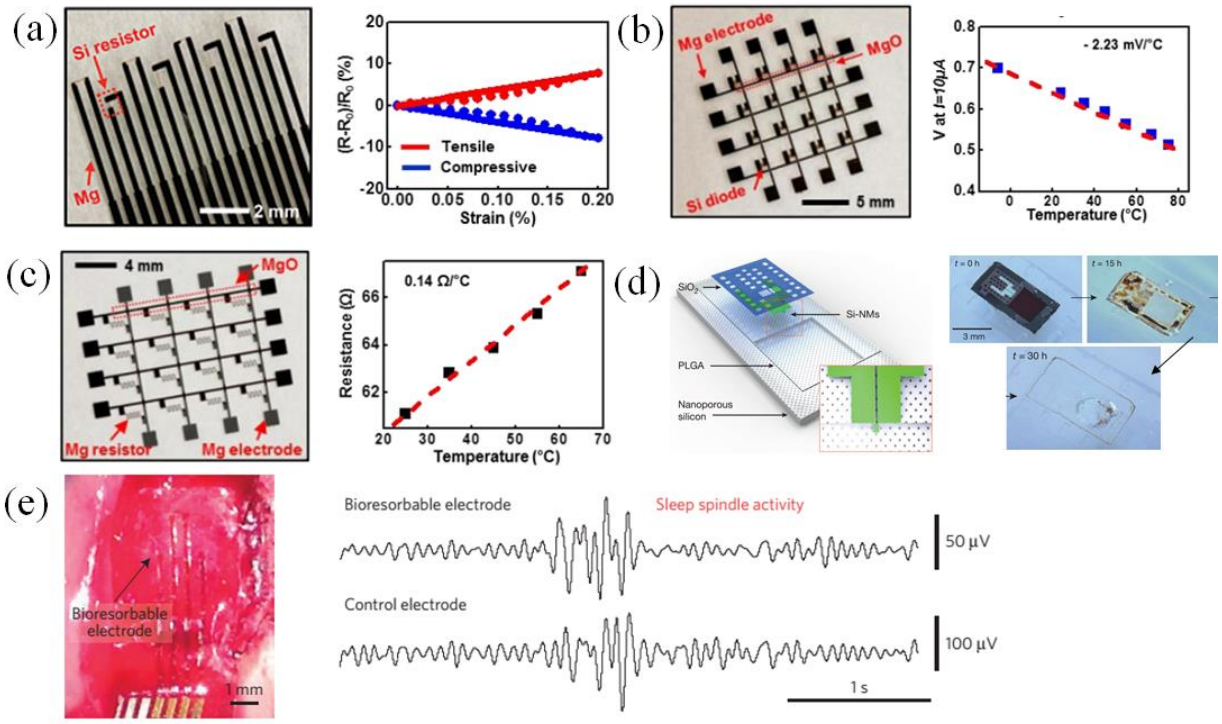

Figure 5.12. *Transient sensors. (a) Image of strain sensors based on Si NM resistors (left). Experimental (symbol) and analytical (line) results of the fractional change in resistance of a silicon resistor as a function of applied tensile (red) and compressive strain (blue) (right). (b) Image of a temperature sensors based on Si NM diodes (left). Voltages applied to a temperature sensor to yield an output current of 10 μA at different temperatures (right). (c) Image of a temperature sensor that use Mg resistors, Mg interconnects, and MgO as an interlayer dielectric (left). Measured dependence of the resistance of a Mg temperature sensor on temperature (right); adapted from [4]. Reprinted with permission from AAAS. (d) Schematic illustration of a biodegradable pressure sensor. Images collected at several stages of accelerated dissolution upon insertion into an aqueous buffer solution (right); adapted by permission from Macmillan Publishers Ltd: [Nature] [42], copyright (2016). (e) Photograph of bioresorbable electrode array placed on the cortical surface of a rat (left). Sleep spindles recorded by a bioresorbable electrode and a commercial stainless steel microwire electrode as a (right); adapted by permission from Macmillan Publishers Ltd: [Nature Materials] [43], copyright (2016).*

device at a controlled rate. Figure 5.12d shows a schematic illustration and photograph of the multifunctional sensor and its dissolution capability, respectively. Another bioresorbable device developed for micro-electrocorticography utilizing advanced inorganic materials was demonstrated as well [43]. Figure 5.12e shows an image of a 4-channel bioresorbable electrode array on the cortical surface of a rat's left hemisphere that recorded sleep spindle activity. These Si nanomembrane electrodes and SiO_2 encapsulating layer were fabricated on a degradable PLGA substrate. These bioresorbable electrodes have demonstrated their ability to capture intracortical and subdermal physiological activity and dissolve after a controlled period of time.

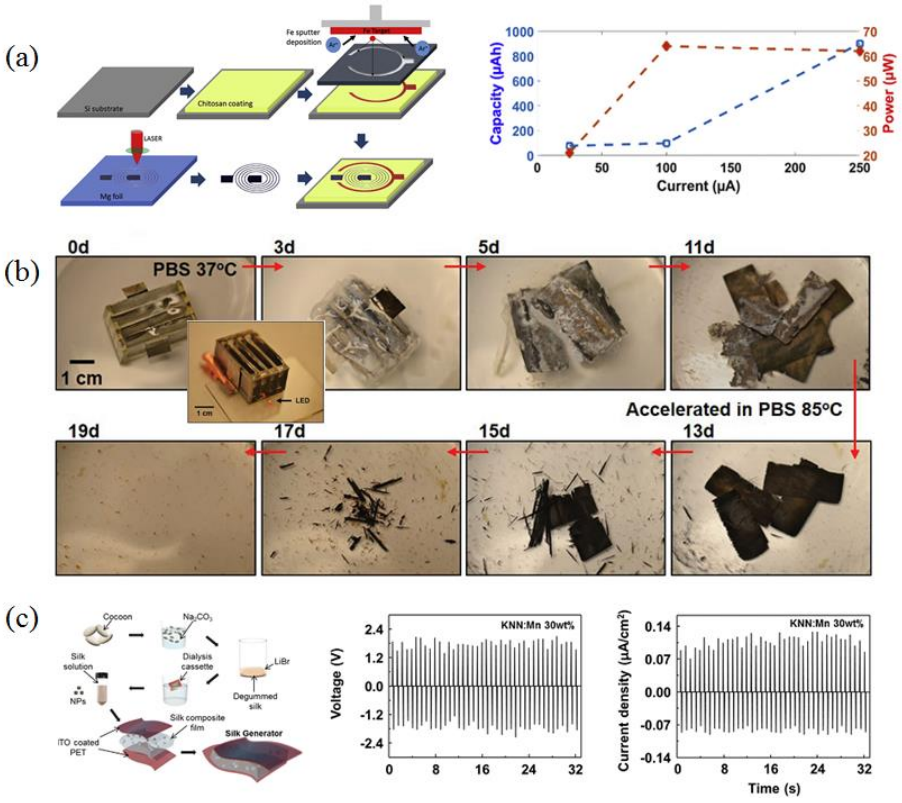

Figure 5.13. *Transient power supplies. (a) Schematic fabrication process of a biodegradable battery (left) and the capacity and power of a Mg-Fe device at different currents; reprinted from [44]. Copyright (2016), with permission from Elsevier. (b) Dissolution of the battery pack that consists of four Mg-Mo cells in series. Inset shows the battery powered operation of a red LED; adapted from [45]. John Wiley & Sons. © 2014 WILEY-VCH Verlag GmbH & Co. KGaA, Weinheim. (c) Schematic fabrication process of a biodegradable nanogenerator (left), output voltage (middle), and current density (right) of the composite nanogenerator with 30 wt% KNN:Mn nanoparticles; reprinted from [46]. Copyright (2015), with permission from Elsevier.*

Biodegradable Power Supplies

Power supplies are an important part of electronic systems, particularly for biomedical devices. For biodegradable green electronics, adding a power supply would eliminate the need for external

wires. Power supply systems that enable the wireless function of electronic devices include wireless scavengers, batteries, and nanogenerators. These supply systems were also demonstrated in biodegradable formats [14, 44-46]. RF power scavengers that can receive power wirelessly have shown the capability to convert RF power at 950 MHz to turn on an LED, which was reviewed with optoelectronics [14]. RF power around 17.3 dBm (54 mW) was wirelessly received by an Mg antenna connected to an RF power scavenger circuit and 8.3 mW was used to turn on the LED with a power converting efficiency of 15.7%. This demonstration is shown in Figure 5.11.

Edupuganti *et al.* reported a Mg-based biodegradable battery with a maximum power of 67 μW and a capacity of 5.2 mAh [44]. The fabrication starts from forming a Mg spiral anode using laser micromachining followed by placing the Mg spiral onto a silicon wafer coated with chitosan which works as a biodegradable substrate, as described in Figure 5.13a. An Fe cathode was sputtered through a laser micromachined mask of Mg foil onto the substrate. The demonstrated size and power level of this biodegradable battery are suitable for low-power transient systems. Yin et al. demonstrated another biodegradable primary battery using Mg foils as anodes, metal foils based on Fe, W, or Mo as cathodes, and polyanhydrides as packages [45]. The battery showed a capacity of ~2.4 mAh with a 1 cm^2 active area, 50 μm thick Mg foil, and 8 μm thick Mo foil. Figure 5.13b shows the dissolution process of the battery, from which we find the package dissolve first, leaving only the Mg and Mo foils after 11 days.

Biodegradable piezoelectric composite nanogenerators based on silk fibroin were demonstrated as well [46]. As shown in Figure 5.13c, after obtaining the silk solution from the cocoon, a mixture of polyvinylpyrrolidone (PVP) Ag nanowires were poured into the solution, followed by adding prepared biocompatible ferroelectric nanoparticles into it. The solution was spin-casted onto an ITO/PET substrate which served as the bottom electrode and another ITO/PET film was

placed on top of the composite serving as the top electrode. The thin film type nanogenerator achieved a maximum output voltage of 2.2 V and current densities of 0.12 μA/cm^2 with 30 wt% $K_{0.5}Na_{0.5}Nb_{0.995}Mn_{0.005}O_3$ (KNN:Mn) nanoparticles, as shown in Figure 5.13c. By adding glycerol into the composite, the degradation of the composite was controllable. These nanogenerators are suitable for powering implantable devices that require low power.

Like the reviewed optoelectronics, sensors, and power supplies, inorganic materials are found in most types of high-performance electronic components. Using different combinations of biodegradable inorganic materials, it is expected that nearly all types of electronic components to complete an electronic device, such as a cell phone, can be achieved.

5.5. Conclusion

We have reviewed and summarized a set of materials, chip designs, and fabrication processes for making high-performance green electronics. From transistors and diodes to sensors and nanogenerators, electronic components have been demonstrated in fully or partially biodegradable formats. These combined demonstrations will lead to a massive reduction in e-waste and reduce the necessity for sophisticated and expensive recycling processes. Furthermore, the focus of this review was to distinguish biodegradable electronics based on inorganic semiconductors from other biodegradable electronics to emphasize the recent progress towards high-performance green electronics. As conventional electronics benefit from high carrier mobilities of inorganic semiconductors, green electronics must be fabricated using the same or comparable materials, with minimal changes in the fabrication procedures, with high reliability, and without a significant cost increase. These criteria are essential to address the serious environmental threat that mankind faces today due to the massive amounts of e-waste created daily. While biodegradable integrated circuit

fabrication methods were summarized in detail, the content covered in this review may be further extended without substantial changes to manufacture other electronic components like optoelectronics, sensors, and power supplies. Combined with other efforts to produce green components for electronics, such as displays and cases, next generation consumer electronics should be more ecofriendly.

5.6. Reference

[1] S.-W. Hwang, G. Park, C. Edwards, E. A. Corbin, S.-K. Kang, H. Cheng, *et al.*, "Dissolution Chemistry and Biocompatibility of Single-Crystalline Silicon Nanomembranes and Associated Materials for Transient Electronics," *ACS Nano*, vol. 8, pp. 5843-5851, Jun 2014.

[2] S.-K. Kang, G. Park, K. Kim, S.-W. Hwang, H. Cheng, J. Shin, *et al.*, "Dissolution Chemistry and Biocompatibility of Silicon- and Germanium-Based Semiconductors for Transient Electronics," *ACS Applied Materials & Interfaces*, vol. 7, pp. 9297-9305, May 2015.

[3] J. Zhou, N. S. Xu, and Z. L. Wang, "Dissolving behavior and stability of ZnO wires in biofluids: A study on biodegradability and biocompatibility of ZnO nanostructures," *Advanced Materials*, vol. 18, pp. 2432-2435, Sep 2006.

[4] S.-W. Hwang, H. Tao, D.-H. Kim, H. Cheng, J.-K. Song, E. Rill, *et al.*, "A Physically Transient Form of Silicon Electronics," *Science*, vol. 337, pp. 1640-1644, Sep 2012.

[5] C. W. Lam, S.-R. Lim, and J. M. Schoenung, "Linking Material Flow Analysis with Environmental Impact Potential," *Journal of Industrial Ecology*, vol. 17, pp. 299-309, 2013.

[6] J. Cui and L. Zhang, "Metallurgical recovery of metals from electronic waste: A review," *Journal of Hazardous Materials,* vol. 158, pp. 228-256, Oct 2008.

[7] Y. Yun, Z. Dong, N. Lee, Y. Liu, D. Xue, X. Guo, *et al.*, "Revolutionizing biodegradable metals," *Materials Today,* vol. 12, pp. 22-32, Oct 2009.

[8] Y. F. Zheng, X. N. Gu, and F. Witte, "Biodegradable metals," *Materials Science & Engineering R-Reports,* vol. 77, pp. 1-34, Mar 2014.

[9] L. Yin, H. Cheng, S. Mao, R. Haasch, Y. Liu, X. Xie, *et al.*, "Dissolvable Metals for Transient Electronics," *Advanced Functional Materials,* vol. 24, pp. 645-658, Feb 2014.

[10] S.-K. Kang, S.-W. Hwang, . Cheng, S. Yu, B. H. Kim, J.-H. Kim, *et al.*, "Dissolution Behaviors and Applications of Silicon Oxides and Nitrides in Transient Electronics," *Advanced Functional Materials,* vol. 24, pp. 4427-4434, Jul 2014.

[11] H.-J. Chung, T.-I. Kim, H.-S. Kim, S. A. Wells, S. Jo, N. Ahmed, *et al.*, "Fabrication of Releasable Single-Crystal Silicon-Metal Oxide Field-Effect Devices and Their Deterministic Assembly on Foreign Substrates," *Advanced Functional Materials,* vol. 21, pp. 3029-3036, Aug 2011.

[12] D. G. Schlom, S. Guha, and S. Datta, "Gate Oxides Beyond SiO(2)," *MRS Bulletin,* vol. 33, pp. 1017-1025, Nov 2008.

[13] L. Yan, C. M. Lopez, R. P. Shrestha, E. A. Irene, A. A. Suvorova, and M. Saunders, "Magnesium oxide as a candidate high-kappa gate dielectric," *Applied Physics Letters,* vol. 88, p. 142901, Apr 2006.

[14] S.-W. Hwang, X. Huang, J.-H. Seo, J.-K. Song, S. Kim, S. Hage-Ali, *et al.*, "Materials for Bioresorbable Radio Frequency Electronics," *Advanced Materials,* vol. 25, pp. 3526-3531, Jul 2013.

[15] D.-H. Kim, Y.-S. Kim, J. Amsden, B. Panilaitis, D. L. Kaplan, F. G. Omenetto, *et al.*, "Silicon electronics on silk as a path to bioresorbable, implantable devices," *Applied Physics Letters*, vol. 95, p. 133701, Sep 2009.

[16] S.-W. Hwang, D.-H. Kim, H. Tao, T.-I. Kim, S. Kim, K. J. Yu, *et al.*, "Materials and Fabrication Processes for Transient and Bioresorbable High-Performance Electronics," *Advanced Functional Materials*, vol. 23, pp. 4087-4093, Sep 2013.

[17] D.-H. Kim, J. Viventi, J. J. Amsden, J. Xiao, L. Vigeland, Y.-S. Kim, *et al.*, "Dissolvable films of silk fibroin for ultrathin conformal bio-integrated electronics," *Nature Materials*, vol. 9, pp. 511-517, Jun 2010.

[18] S. Sofia, M. B. McCarthy, G. Gronowicz, and D. L. Kaplan, "Functionalized silk-based biomaterials for bone formation," *J Biomed Mater Res*, vol. 54, pp. 139-48, Jan 2001.

[19] H. Perry, A. Gopinath, D. L. Kaplan, L. Dal Negro, and F. G. Omenetto, "Nano- and micropatterning of optically transparent, mechanically robust, biocompatible silk fibroin films," *Advanced Materials*, vol. 20, pp. 3070-3072, Aug 2008.

[20] Y. M. Yang, X. M. Chen, F. Ding, P. Y. Zhang, J. Liu, and X. S. Go, "Biocompatibility evaluation of silk fibroin with peripheral nerve tissues and cells in vitro," *Biomaterials*, vol. 28, pp. 1643-1652, Mar 2007.

[21] R. L. Horan, K. Antle, A. L. Collette, Y. Huang, J. Huang, J. E. Moreau, *et al.*, "In vitro degradation of silk fibroin," *Biomaterials*, vol. 26, pp. 3385-3393, Jun 2005.

[22] Q. Lu, X. Hu, X. Wang, J. A. Kluge, S. Lu, P. Cebe, *et al.*, "Water-insoluble silk films with silk I structure," *Acta Biomaterialia*, vol. 6, pp. 1380-1387, Apr 2010.

[23] H.-J. Jin, J. Park, V. Karageorgiou, U.-J. Kim, R. Valluzzi, and D. L. Kaplan, "Water-stable silk films with reduced beta-sheet content," *Advanced Functional Materials*, vol. 15, pp.

1241-1247, Aug 2005.

[24] J. Huang, H. Zhu, Y. Chen, C. Preston, K. Rohrbach, J. Cumings, *et al.*, "Highly Transparent and Flexible Nanopaper Transistors," *ACS Nano*, vol. 7, pp. 2106-2113, Mar 2013.

[25] H. Zhu, Z. Xiao, D. Liu, Y.Li, N. J. Weadock, Z. Fang, *et al.*, "Biodegradable transparent substrates for flexible organic-light-emitting diodes," *Energy & Environmental Science*, vol. 6, pp. 2105-2111, Jul 2013.

[26] Y. H. Jung, T.-H. Chang, H. Zhang, C. Yao, Q. Zheng, V. W. Yang, *et al.*, "High-performance green flexible electronics based on biodegradable cellulose nanofibril paper," *Nature Communications*, vol. 6, p. 7170, May 2015.

[27] M. Nogi, S. Iwamoto, A. N. Nakagaito, and H. Yano, "Optically Transparent Nanofiber Paper," *Advanced Materials,* vol. 21, p. 1595, Apr 2009.

[28] Q. Yang, X. Qin, and L. Zhang, "Properties of cellulose films prepared from NaOH/urea/zincate aqueous solution at low temperature," *Cellulose,* vol. 18, pp. 681-688, Jun 2011.

[29] S.-W. Hwang, J.-K. Song, X. Huang, H. Cheng, S.-K. Kang, B. H. Kim, *et al.*, "High-Performance Biodegradable/Transient Electronics on Biodegradable Polymers," *Advanced Materials,* vol. 26, pp. 3905-3911, Jun 2014.

[30] S.-W. Hwang, C. H. Lee, H. Cheng, J. W. Jeong, S.-K. Kang, J.-H. Kim, *et al.*, "Biodegradable Elastomers and Silicon Nanomembranes/Nanoribbons for Stretchable, Transient Electronics, and Biosensors," *Nano Letters,* vol. 15, pp. 2801-2808, May 2015.

[31] C. J. Bettinger and Z. Bao, "Organic Thin-Film Transistors Fabricated on Resorbable Biomaterial Substrates," *Advanced Materials,* vol. 22, p. 651, Fe 2010.

[32] H. K. Makadia and S. J. Siegel, "Poly Lactic-co-Glycolic Acid (PLGA) as Biodegradable Controlled Drug Delivery Carrier," *Polymers*, vol. 3, pp. 1377-1397, Sep 2011.

[33] R. A. Jain, "The manufacturing techniques of various drug loaded biodegradable poly(lactide-co-glycolide) (PLGA) devices," *Biomaterials*, vol. 21, pp. 2475-2490, Dec 2000.

[34] J. M. Anderson and M. S. Shive, "Biodegradation and biocompatibility of PLA and PLGA microspheres," *Advanced Drug Delivery Reviews*, vol. 64, pp. 72-82, Dec 2012.

[35] K. A. Athanasiou, C. M. Agrawal, F. A. Barber, and S. S. Burkhart, "Orthopaedic applications for PLA-PGA biodegradable polymers," *Arthroscopy*, vol. 14, pp. 726-737, Oct 1998.

[36] D. Cohn and A. F. Salomon, "Designing biodegradable multiblock PCL/PLA thermoplastic elastomers," *Biomaterials*, vol. 26, pp. 2297-2305, May 2005.

[37] J. Yang, A. R. Webb, S. J. Pickerill, G. Hageman, and G. A. Ameer, "Synthesis and evaluation of poly(diol citrate) biodegradable elastomers," *Biomaterials*, vol. 27, pp. 1889-1898, Mar 2006.

[38] J. A. Rogers, T. Someya, and Y. Huang, "Materials and Mechanics for Stretchable Electronics," *Science*, vol. 327, pp. 1603-1607, Mar 2010.

[39] J. A. Rogers, M. G. Lagally, and R. G. Nuzzo, "Synthesis, assembly and applications of semiconductor nanomembranes," *Nature*, vol. 477, pp. 45-53, Sep 2011.

[40] M. A. Meitl, Z. T. Zhu, V. Kumar, K. J. Lee, X. Feng, Y. Huang, *et al.*, "Transfer printing by kinetic control of adhesion to an elastomeric stamp," *Nature Materials*, vol. 5, pp. 33-38, Jan 2006.

[41] X. Huang, Y. Liu, S.-W. Hwang, S.-K. Kang, D. Patnaik, J. F. Cortes, *et al.*, "Biodegradable

Materials for Multilayer Transient Printed Circuit Boards," *Advanced Materials,* vol. 26, pp. 7371-7377, Nov 2014.

[42] S.-K. Kang, R. K. J. Murphy, S.-W. Hwang, S. M. Lee, D. V. Harburg, N. A. Krueger, *et al.*, "Bioresorbable silicon electronic sensors for the brain," *Nature,* vol. 530, pp. 71, Feb 2016.

[43] K. J. Yu, D. Kuzum, S.-W. Hwang, B. H. Kim, H. Juul, N. H. Kim, *et al.*, "Bioresorbable silicon electronics for transient spatiotemporal mapping of electrical activity from the cerebral cortex," *Nature Materials,* vol. 15, pp. 782, Jul 2016.

[44] V. Edupuganti and R. Solanki, "Fabrication, characterization, and modeling of a biodegradable battery for transient electronics," *Journal of Power Sources,* vol. 336, pp. 447-454, Dec 30 2016.

[45] L. Yin, X. Huang, H. Xu, Y. FZhang, J. Lam, J. Cheng, *et al.*, "Materials, Designs, and Operational Characteristics for Fully Biodegradable Primary Batteries," *Advanced Materials,* vol. 26, pp. 3879-3884, Jun 2014.

[46] K. N. Kim, J. Chun, S. A. Chae, C. W. Ahn, I. W. Kim, S. W. Kim, *et al.*, "Silk fibroin-based biodegradable piezoelectric composite nanogenerators using lead-free ferroelectric nanoparticles," *Nano Energy,* vol. 14, pp. 87-94, May 2015.

CHAPTER 6
High-performance green flexible electronics based on biodegradable cellulose nanofibril paper

Today's consumer electronics, such as cell phones, tablets and other portable electronic devices, are typically made of non-renewable, non-biodegradable, and sometimes potentially toxic (for example, gallium arsenide) materials. These consumer electronics are frequently upgraded or discarded, leading to serious environmental contamination. Thus, electronic systems consisting of renewable and biodegradable materials and minimal amount of potentially toxic materials are desirable. Here we report high performance flexible microwave and digital electronics that consume the smallest amount of potentially toxic materials on biobased, biodegradable, and flexible cellulose nanofibril papers. Furthermore, we demonstrate gallium arsenide microwave devices, the consumer wireless workhorse, in a transferrable thin-film form. Successful fabrication of key electrical components on the flexible cellulose nanofibril paper with comparable performance to their rigid counterparts and clear demonstration of fungal biodegradation of the cellulose nanofibril-based electronics suggest that it is feasible to fabricate high performance flexible electronics using ecofriendly materials.

6.1. Introduction

Consumer electronics, particularly portable electronics, such as smart phones, tablets etc. together with their supported Big Data industry have helped sustain the economic growth in the majority part of today's world. However, rapid technological advances have led to a significant decrease in the lifetime of the consumer electronics and also rapid consumption of non-renewable

natural resources. On average, cell phones are used for less than 18 months and computers are used for less than three years before being replaced [1, 2]. In fact, in 2007, it was estimated that over 426,000 cellphones (most of them were still functional) and 112,000 computers were discarded every day in the U.S., totaling 3.2 million tons of electronic waste generated per year [3, 4]. These discarded electronics increase the demand for landfill space and may also cause some serious environmental concerns [4-7]. Thus, the use of biodegradable materials in electronics can reduce the accumulation of persistent solid waste, thereby benefiting our living environment. Moreover, today's chips in portable electronic devices are made at large amount yet unnecessary consumption of precious materials. In a typical semiconductor electronic chip, the active region comprised in the top thin layer is only a small portion of the chip, whereas the bottom substrate that holds the chip consists of more than 99% of the semiconductor materials [8]. In microwave chips for wireless functions, besides the waste of the bottom substrate, only a tiny fraction of the lateral chip area is used for the needed active transistors/diodes with the rest being used only for carrying other non-active components. Some toxic semiconductor materials like gallium arsenide (GaAs) [9, 10] are widely used in high speed communication devices, such as cell phones and tablets, and can lead to a significant amount of hazardous materials and high cost in applications that require sparse areal coverage, such as monolithic microwave integrated circuits (MMIC). In order to minimize the usage of semiconductors, fully formed electronic devices can be fabricated on a sacrificial material in a dense array format, where each micro-scale device can be released and transfer printed onto any type of substrate, including biodegradable flexible substrates. The feasibility of such an approach has been demonstrated in several reports, where devices are fabricated on a wafer that enables deterministic assembly of individual devices on foreign substrates via the transfer printing process [11-14]. Utilizing this technique, the handling substrate is no longer necessary and

the substrate can be re-used for further growth of active layers upon the depletion of all devices. This is especially useful in GaAs based electronics where the chemical extraction of GaAs from discarded waste is prohibitively expensive and dangerous due to the presence of Arsenic [9, 10]. To obtain degradable capabilities, new materials that are non-toxic and biodegradable in nature, such as paper, silk, and a number of synthetic polymers, have been explored as electronic substrates [15-19]. Many groups have reported electronics on paper by depositing organic semiconductors, but while the concept is very interesting in that it is flexible and degradable, the performance of such electronics falls behind the requirements of state-of-the-art electronics [20-22]. Another promising approach developed by Hwang et al. was to use biodegradable silk combined with high performance inorganic semiconductors [17, 19]. Despite their excellent degradation capability, biocompatibility, and performance, silk-based electronics are highly vulnerable to water and solvents. In addition, the suitability of silk for microwave applications is unknown. It should also be noted that only silicon (Si)-based electronics were demonstrated on biodegradable silk substrate. However, Si has a low mobility compared to GaAs, which limits its use in microwave electronics. Cellulose nanofibril (CNF) is an ecofriendly material as it is completely derived from wood [23, 24]. With its high transparency [25, 26] and flexibility [27], as well as desirable electrical properties [28], CNF is an ideal candidate as an alternative and ecofriendly substrate for electronics. A number of groups have reported on CNF-based electronics [29-32]. However, whether the biodegradable CNF substrate exhibits suitable radio frequency (RF) properties for microwave based consumer electronics applications has been unknown.

In the following, we explore the microwave applications of CNF and demonstrate high performance electronics that are comparable to existing state-of-the-art electronics, including process-complicated GaAs-based microwave level electronics where the operating frequency is

beyond gigahertz, as well as Si-based digital electronics, on CNF substrates. Fungal biodegradation of these CNF-based electronics, for the purpose of cycling degraded CNF back to forestry as fertilizer, was also carried out to show the decaying process over time. While transfer

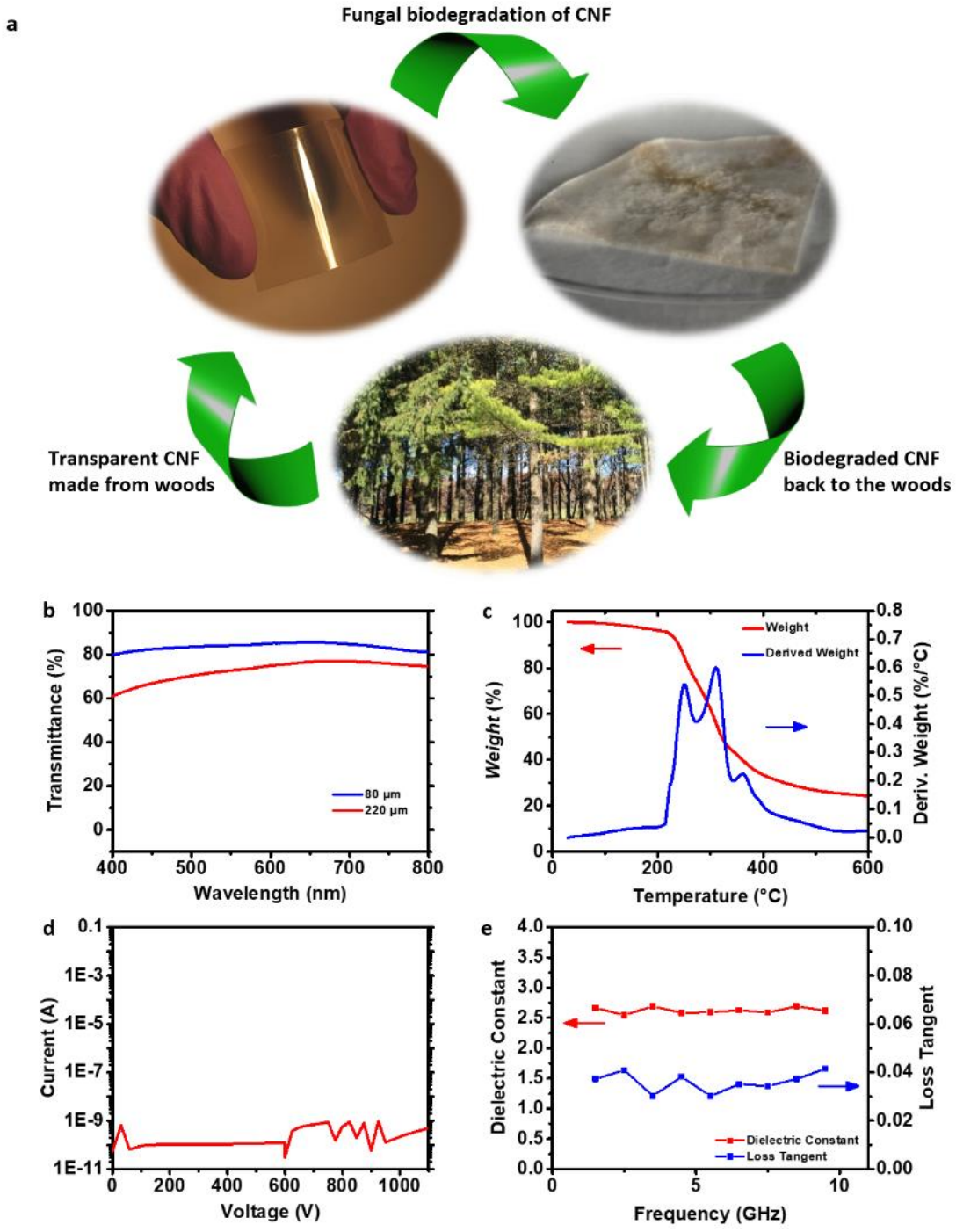

Figure 6.1. *Introduction to cellulose nanofibril (CNF) paper and its basic characteristics as a substrate for electronics (a) An illustration of a likely life cycle of the bioased and biodegradable CNF paper. First, cellulose nanofibrils (CNFs) extracted from the woods is made into CNF paper. The CNF paper can be degraded via fungal biodegradation and sent back to the woods without adverse environmental effects. (b) The transmittance curve over a visible spectrum. Blue and red curves show the transmittance of 80 μm and 200 μm thick CNF films, respectively. (c) A thermogravimetric (TGA) plot showing the weight change of the CNF film as a function of temperature, along with the first derivative (DTG) of the curve. The film remains stable up to 213 °C. (d) The electrical breakdown characteristics of CNF film. Current is measured while high voltage is applied on both sides of the film. (e) Radio frequency characteristics of the CNF film. Dielectric constant (red) and loss tangent (blue) are measured in the frequency range of 0 to 10 GHz using a microstrip waveguide.*

printing techniques and CNF paper are used to realize various high-performance flexible electronics in this work, what is described is a new, much more sustainable, green electronic chip concept to address the societal impact of today's economically important yet environmentally unsustainable consumer electronics, based on the important properties that were discovered from CNF.

6.2. Cellulose nanofibril film and its characteristics

Figure 6.1a presents a likely life cycle of the CNF film where the film is first made from CNFs extracted from the woods, degraded via a fungal biodegradation process upon disposal, and sent back to the woods without adverse environmental effects. Electronic systems based on such

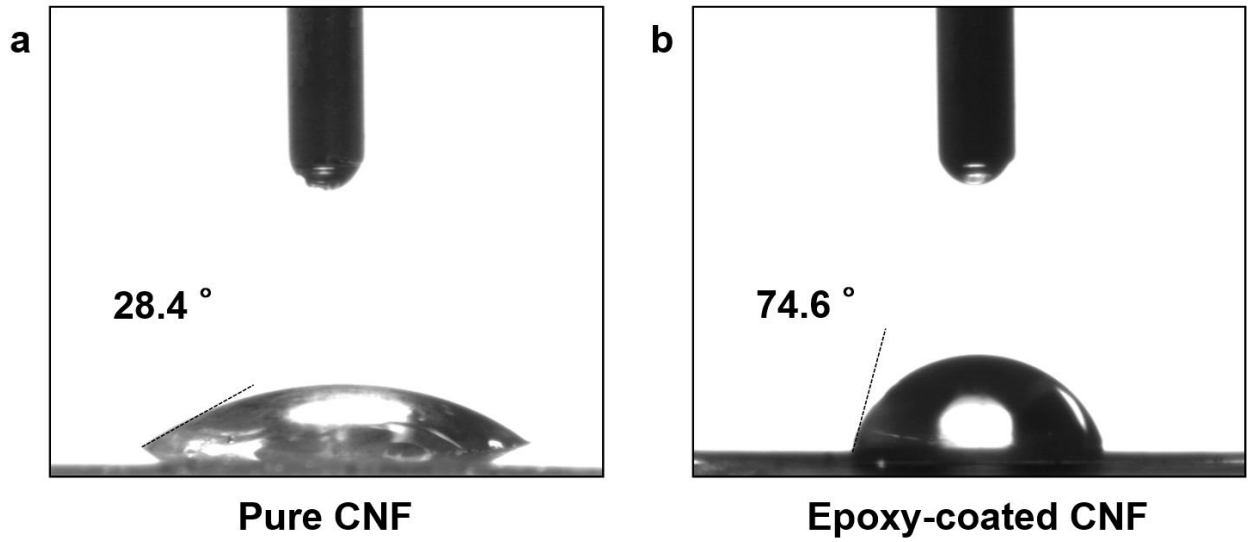

Figure 6.2. *Comparison of the contact angles of a water droplet on a pure CNF film and an epoxy-coated CNF film. The contact angle was (a) 28.4° for the pure CNF paper at t = 1 s and (b) 74.6° for the epoxy-coated CNF paper at t = 1 s.*

material could significantly facilitate recycling and management of waste streams. Thus, the ecofriendly wood-based CNF substrate is clearly an ideal substitution for electronics that exist today. However, pure CNF film is vulnerable to water [33]. To address this issue, we coated the pure CNF film with a bisphenol A-based epoxy resin. As shown in Figure 6.2, the epoxy coating increased the contact angle of the CNF film from 28.4° to 74.6°, thereby making the CNF film much more hydrophobic. This treatment allowed for easier handling of the CNF substrate and offered better manufacturing capabilities. Epoxy is a type of thermoset plastic commonly used in electronics packaging materials (e.g., electronic molding compounds as well as underfills) due to its ease of handling, desirable materials properties, and relatively low cost. The epoxy coating can also enhance the mechanical properties of the CNF film. Figure 6.1b–e introduces the unique material properties of epoxy-coated CNF films. As shown in Figure 6.1b, the CNF film was

transparent, thus making it ideal for certain applications. The transmittance was over 80% for an 80 µm thick CNF film and 60% for a 220 µm thick CNF film over the visible spectrum. Figure 6.1c presents thermogravimetric analysis (TGA) data showing the weight loss of the epoxy-coated CNF film as a function of temperature as well as the first derivative (DTG). There were three peaks

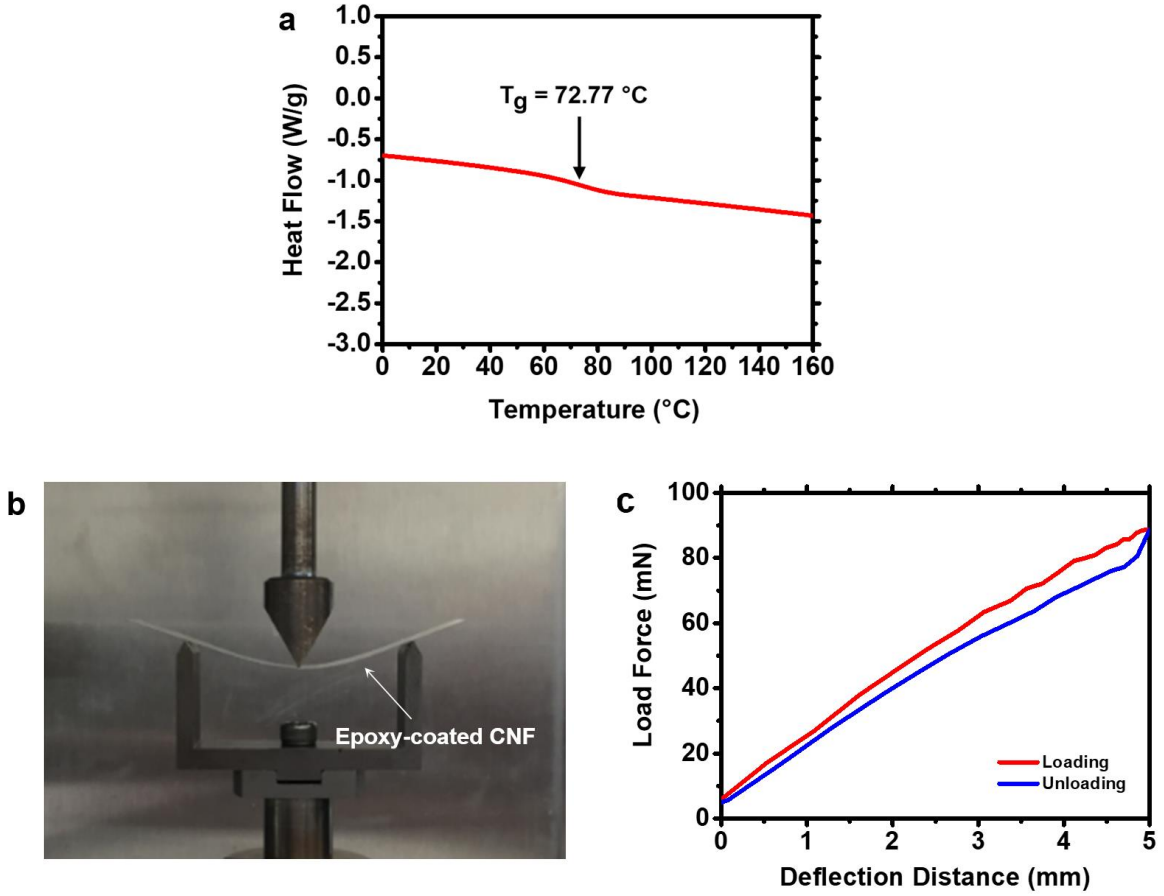

Figure 6.3. *(a) The differential scanning calorimetry (DSC) curve of the epoxy coated CNF film obtained during the second heating cycle. (b) Load-deflection test of the epoxy-coated CNF film using a dynamic mechanical analyzer. Measurement set-up for testing the load-deflection. (c) Measured load force in relation to deflection distance during loading (red) and unloading (blue). The film is reversible back to its flat state after unloading.*

in the DTG curve, with the first (213 °C) and third (270 °C) peak corresponding to the decomposition of the CNF and epoxy process, respectively. The middle peak observed at 310 °C was attributed to the overlapping of the CNF and epoxy decomposition peaks. The glass transition temperature (T_g) of the film was measured at 72.8 °C (Figure 6.3a), which was similar to that of polyethylene terephthalate (PET) film, a commonly used substrate for flexible electronics. In addition, the CNF film was strong and flexible enough to allow reversible bending as shown in Figure 6.3b–c. The flexural modulus of the epoxy-coated CNF film was calculated to be 2.5 GPa, which is comparable to that of PET (1.5 to 2.8 GPa) [34-36]. The electrical properties of the CNF film were also appealing for use with electronics. As presented in Figure 6.1d, the CNF film did not undergo an electrical breakdown, even at very high voltages (e.g., 1100 V), which is far beyond the requirement for consumer electronics. Furthermore, because the dielectric and RF properties of the substrate are major aspects to be considered in designing a RF circuit, the RF loss and dielectric constant were extracted using a microstrip waveguide and analyzed at high frequencies. In the frequency range from 0 to 10 GHz, the dielectric constant ranged from 2.58 to 2.69, and the loss tangent ranged from 0.0302 to 0.0415, as presented in Figure 6.1e. The above characterizations for the first time unveiled the suitability of CNF for high-frequency microwave applications. While the dielectric constant and RF loss values were comparable to those of PET film, the biodegradability property of CNF makes it a superior candidate over PET for addressing the abovementioned environmental impact.

6.3. Fabrication process of GaAs devices on CNF substrates

Compared to devices operating at low frequencies (~MHz) or direct current (DC) levels, microwave (~GHz) devices are especially difficult to fabricate on foreign substrates, due to the

small feature sizes and high temperature processes required for high performance. Here, we present, for the first time, methods to fabricate microwave GaAs-based devices on foreign substrates, namely the CNF substrate in this case. It should be noted that today's majority portable gadgets (>85% in cell phones) with wireless communication functions employ GaAs-based microwave devices for their superior high-frequency operation and power handling capabilities. Figure 6.4a outlines the procedure for manufacturing GaInP/GaAs heterojunction bipolar transistors (HBTs)

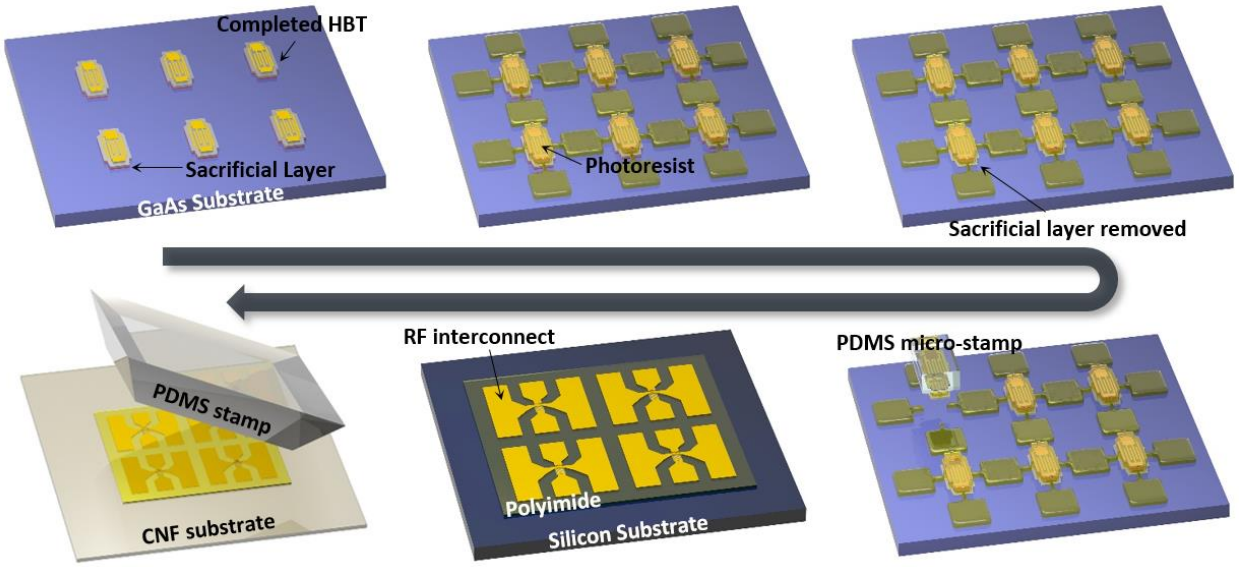

Figure 6.4. *The fabrication process for deterministic assembly of GaAs devices on CNF paper. Schematic illustration of the fabrication process of GaInP/GaAs HBTs on a CNF substrate. The HBTs are fabricated on a sacrificial layer grown on a GaAs substrate and released with protective anchors made of photoresists. Each HBT is picked up using a PDMS micro-stamp and printed onto a temporary Si substrate with polyimide as the adhesive. After RF interconnect metallization, the devices are released from the temporary substrate and printed onto a CNF substrate using a PDMS stamp.*

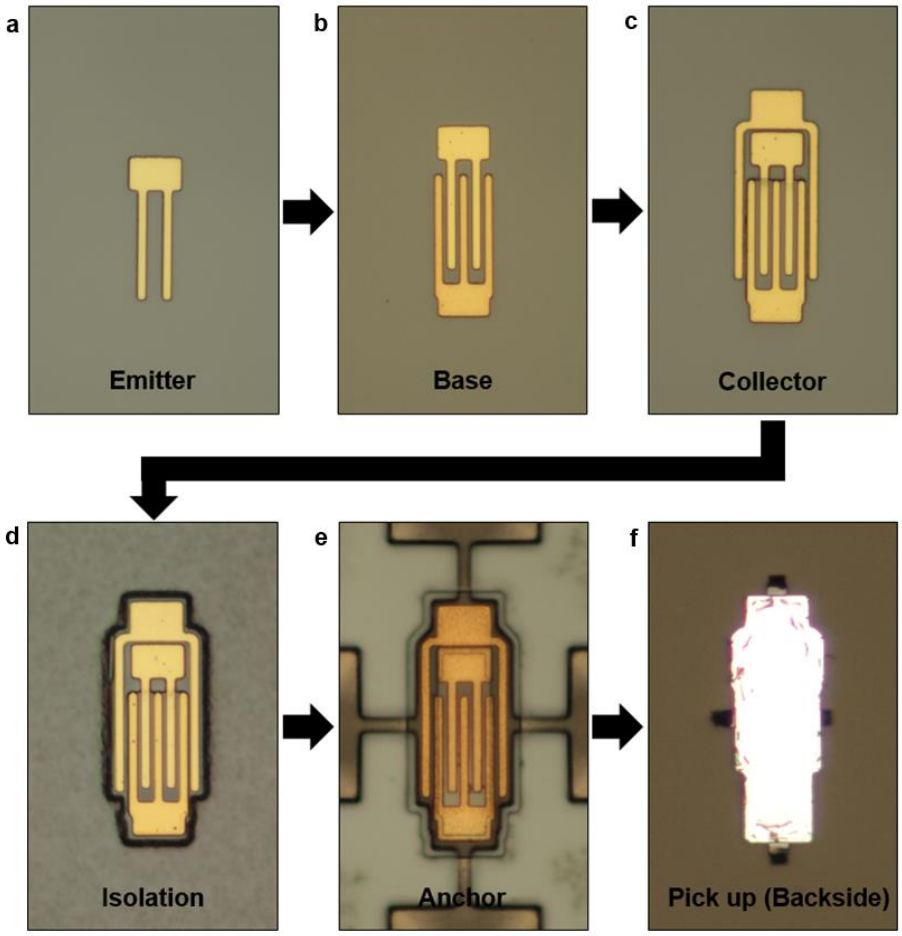

Figure 6.5. *Illustration of the fabrication steps of GaInP/GaAs HBT via a sequence of optical images. (a) Emitter metal is deposited on a GaAs cap layer. (b) Emitter layer is plasma etched and base metal is deposited. (c) After base mesa etching, the collector metal is deposited. (d) Isolation of the HBT is done by plasma etching. (e) Protective anchor patterning on the HBT. (f) HBT is picked up using a PDMS stamp. The image shows the backside of the HBT.*

on a CNF substrate via schematic illustrations. Thin heterojunction epitaxial layers in stacks of n-cap layer (GaAs:Si)/ n-emitter layer (GaInP:Si)/ p-base layer (GaAs:C)/ n-collector layer (GaAs:Si)/ n-sub-collector layer (GaAs:Si) were grown on a 500 nm thick sacrificial layer

($Al_{0.96}Ga_{0.04}As$) on a GaAs wafer. The fabrication process began by following conventional procedures to fabricate the HBTs (Figure 6.5), followed by protective anchor patterning using a photoresist (PR). This will protect the devices and allow the devices to be tethered to the substrate after etching away the underlying sacrificial layer using a diluted hydrofluoric acid (HF) solution. Van der Waals contact with a soft elastomer stamp made of polydimethylsiloxane (PDMS) to the device breaks the anchors on all four sides and easily picks up a single device. The devices are transfer printed in deterministic assembly onto a temporary Si substrate using ultrathin polyimide (PI, ~1 μm) as an adhesive, followed by ground–signal–ground (G–S–G) RF interconnect metallization. Polyimide is an excellent material for GaAs-based devices not only as an adhesive, but also as a passivating material that can suppress the high surface states of GaAs and prevent leakage current [37]. Devices are then released from the temporary substrate and printed onto a CNF substrate using a PDMS stamp (Figure 6.6). Figures 6.7a-c present optical microscopy images of fully formed HBTs on a GaAs substrate that are ready to be picked up. As shown in

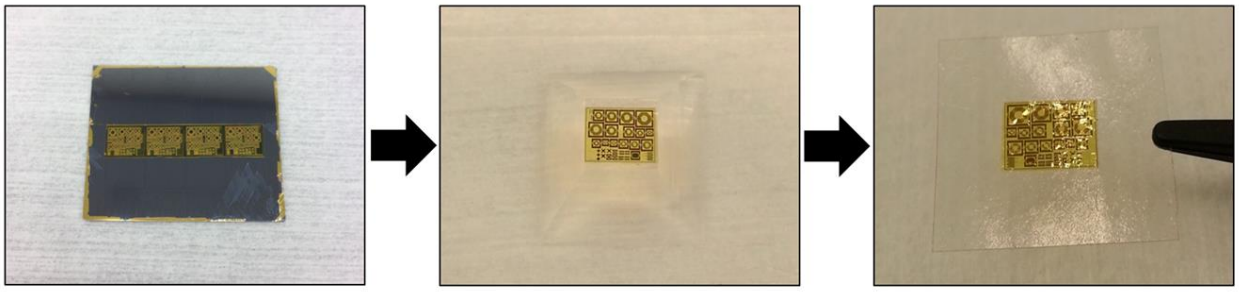

Figure 6.6. *A sequence of optical images demonstrating the transfer process of microwave electronics on a CNF substrate. Here, the transfer process of passive elements is shown as an example. The passive elements are fabricated on a temporary Si substrate (left), picked up using a PDMS stamp (middle), and then transfer printed onto a CNF substrate (right).*

Figure 6.7a, an array of 1,500 releasable HBTs on a 5 × 6 mm^2 GaAs substrate can be fabricated. The image in Figure 6.7d presents an array of HBTs on a CNF substrate wrapped around a tree stick demonstrating the high flexibility of these electronics.

6.4. Analysis of the influence of GaAs on the environment

The Environmental Protection Agency (EPA) has set the Arsenic standard for drinking water at 10 parts-per-billion (ppb) [38], i.e., 10 µg L^{-1}. Compared to a typical GaAs MMIC, which only consists of a few HBTs on a large substrate, this pick-and-place method greatly reduces the usage of expensive and hazardous semiconductor materials. Figure 6.7e presents a quantitative analysis on the amount of Arsenic present in the corresponding device/transistor due to the usage of GaAs that may lead to adverse environmental impact. Also shown in Figure 6.7e is the amount of water calculated according to the EPA standard based on the amount of arsenic present in these devices/transistors. This analysis shows that a significant amount of clean water can be saved or

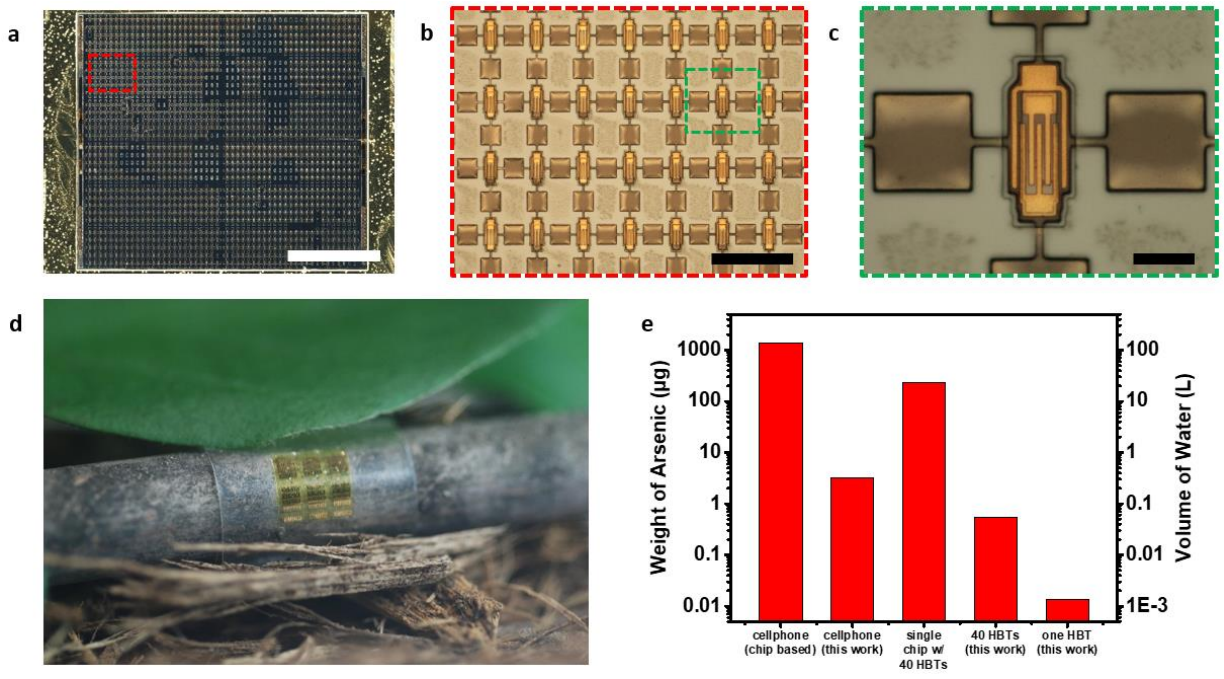

Figure 6.7. *GaAs devices on CNF paper and quantitative analysis on the influence of GaAs to the environment. (a) An optical microscopy image showing 1,500 releasable HBTs in a dense array format on a 5 × 6 mm^2 size GaAs substrate. Scale bar, 2 mm. (b) A magnified image of the array. Scale bar, 200 µm. (c) An optical image showing a single releasable HBT that is tethered to the substrate with photoresist anchors. Scale bar, 30 µm. (d) A photograph of an array of HBTs on a CNF substrate wrapped around a tree stick with a ~3 mm radius. (e) Comparison chart showing the amount of the arsenic corresponding to each type of device/transistor listed as well as the amount of water calculated according to the EPA standard based on the quantity of the arsenic present in these devices/transistors. For a single conventional cell phone, approximately 138 L of water is required to satisfy the EPA standard, whereas only 0.32 L is required using our approach. Additionally, 23 L is required for a single conventional chip with 40 HBTs, while only 0.054 L is required for the same number of HBTs with our approach. One HBT only requires 0.0013 L of water.*

preserved using our deterministic assembly approach in making the GaAs-based electronics. The weight of Arsenic was obtained by converting the measured volume of from either conventional GaAs chip or our printed HBTs to weight. As an example, a conventional miniature GaAs HBT based MMIC with 40 HBTs on a 1.15 × 0.75 mm^2 large and 100 µm thick substrate [39], was used as a reference for the comparison. Moreover, our single GaAs HBT with a volume of 5.04 × 10-6 mm^3 was used. Assuming that there are six GaAs HBT-based MMIC chips in a typical cell phone, approximately 138 L of water is required at minimum to meet the standards, whereas, the same cell phone using our approach only requires 0.32 L of water. For a single conventional chip with 40 HBTs, 22.9 L of water is required, whereas only 0.054 L is required for the 40 HBTs fabricated

using our method. This approach is even more advantageous where only a few HBTs are required. For instance, a single conventional chip with 40 HBTs and 20 HBTs would have similar weight because they are typically built on a similarly sized substrate; however, 20 HBTs printed using our approach would weigh exactly half of the 40 HBTs. In fact, a single printed HBT only requires 0.0013 L of water to meet the EPA standard for drinking water.

6.5. Microwave GaAs electronic devices on CNF substrates

Figures 6.8c–e show the electrical properties of a single finger (2 × 20 μm^2) non-self-aligned HBT on a CNF substrate, which is optically shown in Figures 6.8a and 3b. The inset image of Figure 6.8c shows an optical microscopy image of the device that was measured. The Gummel

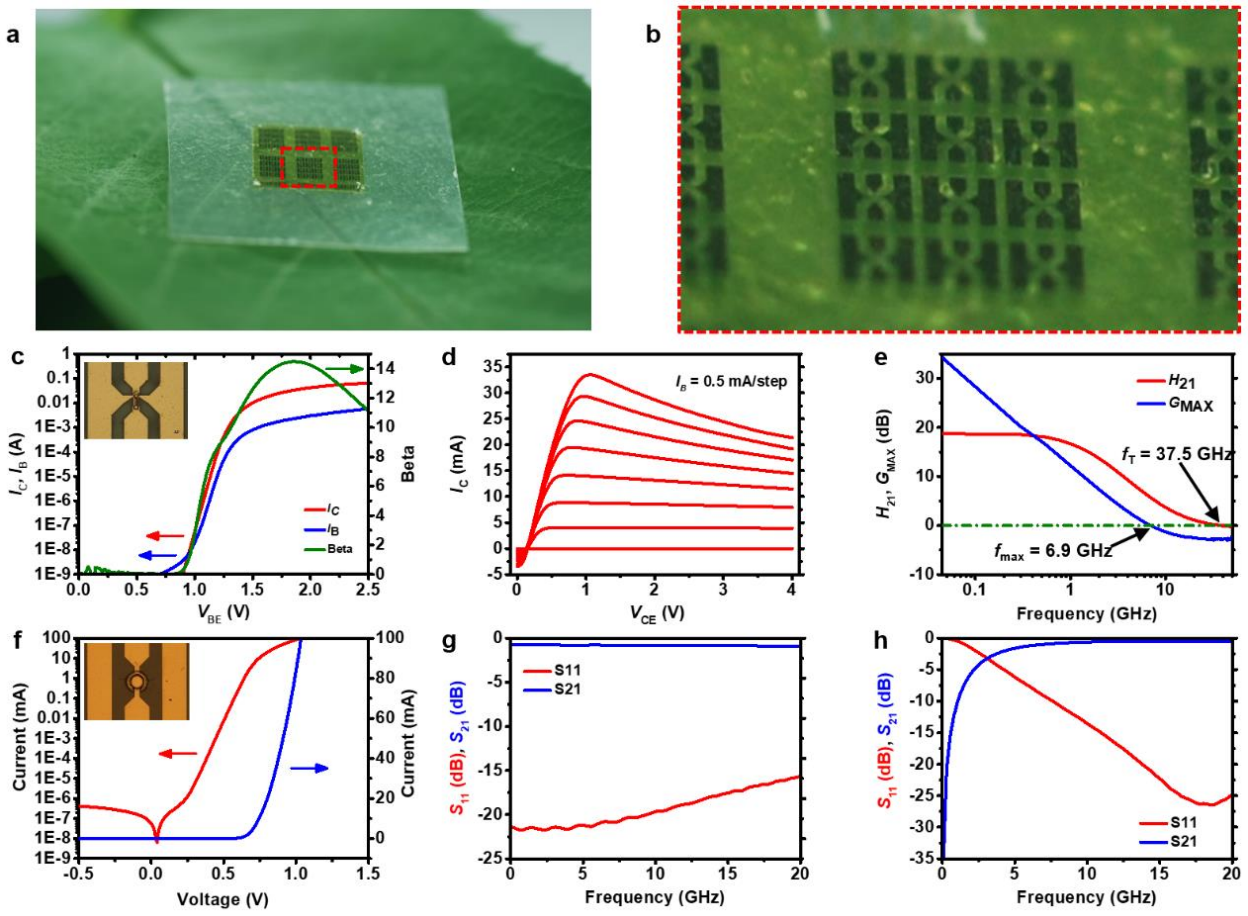

Figure 6.8. *Microwave active GaAs electronic devices on CNF paper. (a) Photograph of an array of HBTs on a CNF substrate put on a tree leaf. (b) Magnified photograph of the array. (c) Gummel plot and Beta plot showing the maximum DC gain of the HBT. The maximum beta is 14.49. The inset optical image shows one of the HBTs in the array that was measured and characterized. (d)* I_C *vs.* V_{CE} *plot of the HBT plotted at 0.5 mA steps of* I_B*. (e) Current gain (*H_{21}*) and power gain (*G_{MAX}*) as a function of frequency, with a collector voltage bias of 2 V and a base current bias of 2 mA. (f) Current versus voltage plot of the Schottky diode on a CNF substrate. The red curve shows the logarithmic scale and the blue curve shows the linear scale. The inset optical image shows the diode transferred onto a CNF substrate with G–S–G interconnects. (g) Measured* S_{11} *(red) and* S_{21} *(blue) plotted against frequency under a forward current bias of 10 mA. (h) Measured* S_{11} *(red) and* S_{21} *(blue) plotted against frequency under a reverse voltage bias of –0.5 V.*

plot presented in Figure 6.8c reflects collector and base electric current, I_C and I_B, against base-emitter voltage, V_{BE} with zero V_{BC} bias. The common-emitter current gain curve under zero V_{BC} bias is shown in green in Figure 6.8c, which indicates that the beta (β) had its maximum value of 14.49 at a V_{BE} of 1.86 V. Under an extreme bending condition (i.e., at a bending radius of 2.5 mm), the maximum beta value decreased slightly to 13.64 (Figure 6.9). The I_C vs. V_{CE} curve is presented in Figure 6.8d. The positive $V_{CEOFFSET}$ value of 0.14 V is due to the single heterojunction structure of our HBT where the offset comes from the difference in bandgap between the emitter (GaInP) and the base (GaAs). The decaying collector current observed as V_{CE} was increased at high base current is attributed to poor thermal dissipation as the thermal conductivity of the underlying CNF substrate (κ = 1.0 W m^{-1} K^{-1}) [40] was lower than that of a typical GaAs substrate (κ = 56 W m-1 K^{-1}) [41]. The RF performances of the HBT were analyzed from the measured scattering (S-)

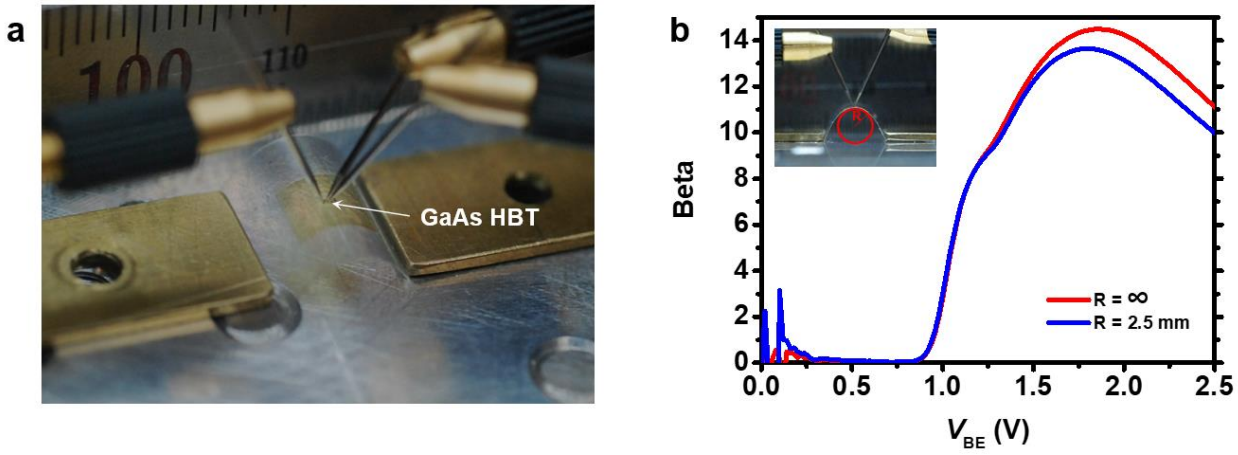

Figure 6.9. *Effect of bending on the Beta gain of GaAs HBT. (a) Measurement set-up for testing the GaAs HBT under bending. (b) Comparison of the Beta plot for GaAs HBT when the CNF substrate was flat (red) or bent (with a radius of curvature of 2.5 mm) (blue).*

parameters from 0.045 to 50 GHz (Figure 6.10). Open and short patterns of the probing pads on the CNF substrate were used to subtract the effect of parasitic inductances and capacitances of the pad. Figure 6.8e presents the current gain (H_{21}) and power gain (G_{MAX}) against frequency for the

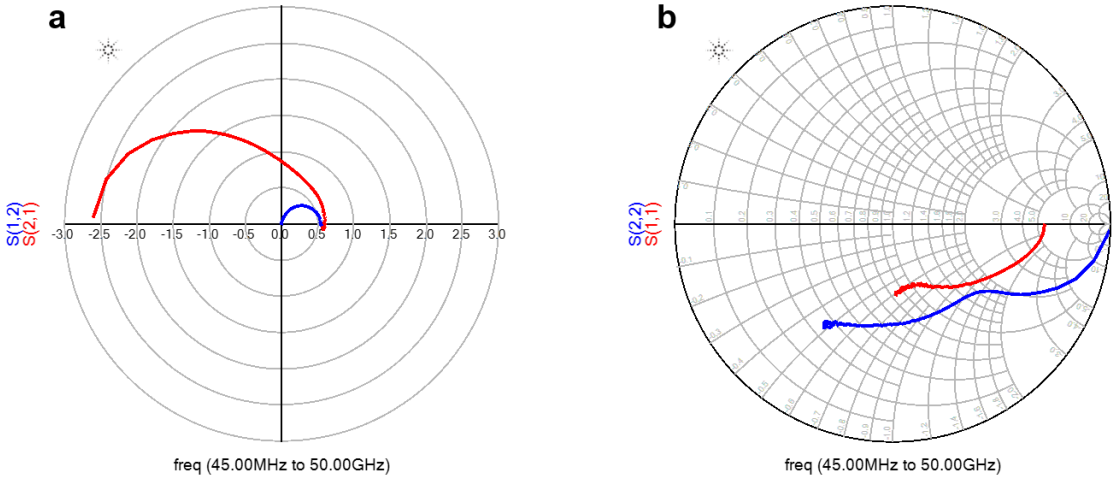

Figure 6.10. *Measured S-parameters of the HBT on a CNF substrate with (a) S_{12} (blue) and S_{21} (red) plotted on a polar plot, and (b) S_{11} (red) and S_{22} (blue) plotted on a Smith chart.*

device under a bias of V_C = 2 V and I_B = 2 mA. A high cut-off frequency (f_T) of 37.5 GHz and a maximum oscillation frequency (f_{max}) of 6.9 GHz were obtained. The relatively low f_{max} of 6.9 GHz was attributed to the non-self-aligned structure of the HBT where large emitter-base spacing (2 µm) introduced high base resistance, causing the f_{max} to drop [42]. These outstanding RF results further prove the suitability of CNF for microwave applications. Although we observed a decay of current at increasing voltages due to the relatively low thermal conductivity of the CNF film, the frequency responses of the HBT were sufficiently high to be used as practical amplifiers in mobile devices where the cellular frequency is in the range of 800 to 2500 MHz. By incorporating materials with high thermal conductivities, such as boron nitride or diamond nanoparticles into the CNF film, the device performance can be further improved.

Schottky diodes based on GaAs are commonly used in high speed communication systems as mixers and rectifiers. Same fabrication techniques with minor changes, as described in Figure 6.4 can be implemented to fabricate high performance Schottky diodes. Similar to the HBTs, nearly 1,200 Schottky diodes with high yield can be fabricated on a 5 × 6 mm^2 GaAs substrate. Figure 6.8f (with an inset image showing the measured diode) presents the DC performance of the diode measured on a CNF substrate, where an ideal Schottky behavior with a low turn on voltage of 0.7 V was obtained. A logarithmic plot (shown in red) of the data shows a good ideality factor of 1.058. Figures 6.8g and 6.8h present the measured S-parameters of the diode at forward bias and reverse bias, respectively (polar plots and Smith charts are shown in Figure 6.11). At a forward current bias of 10 mA (V = 740.6 mV), the insertion loss (S_{21}) was only −1 dB at 20 GHz, making it suitable for RF applications. At a reverse voltage bias of −0.5 V (I = −414.1 pA), the insertion loss (S_{21}) reached −2 dB at 4.3 GHz. The low resistance obtained under reverse bias at high frequencies shows that these diodes can perform with high switching speeds in microwave circuits.

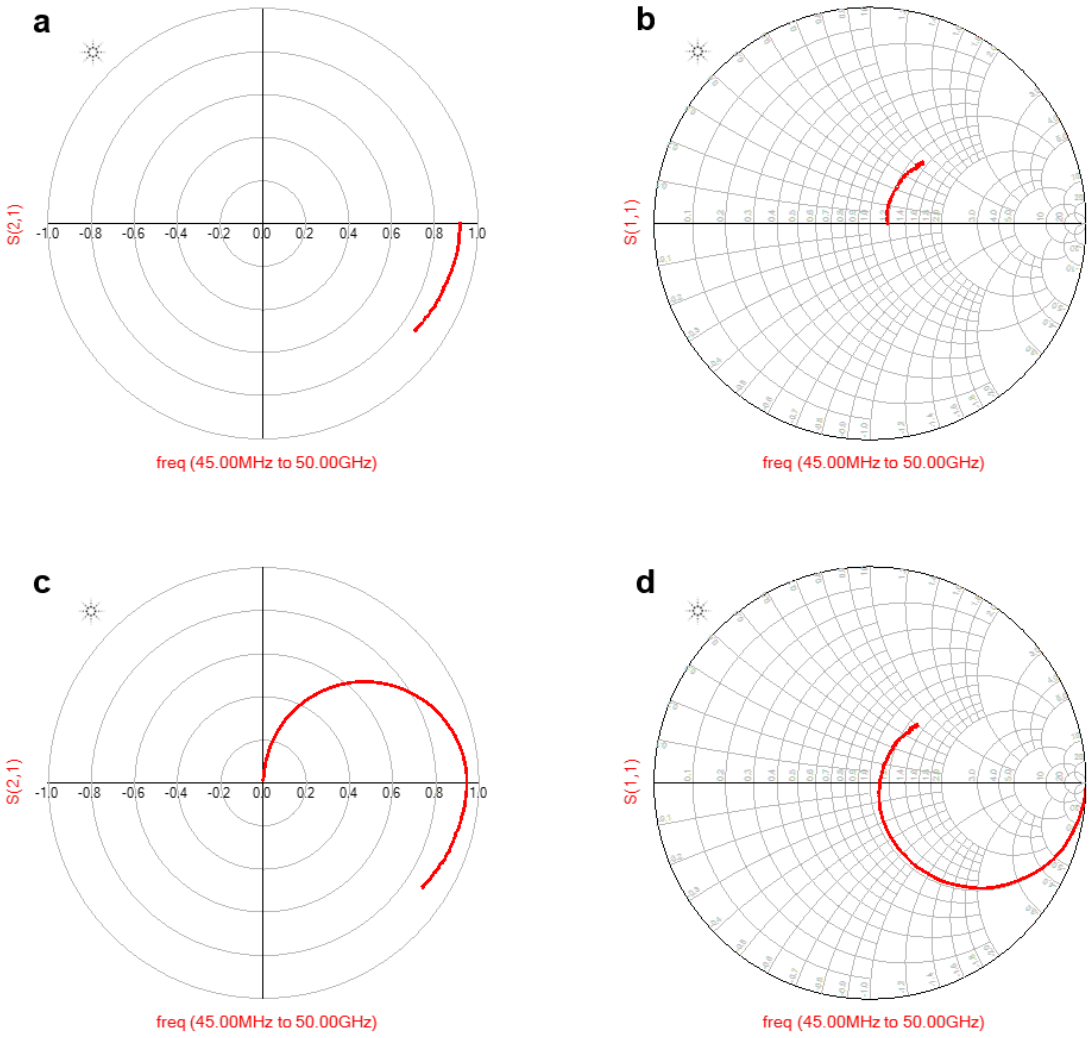

Figure 6.11. *Measured S-parameters of the Schottky diode on a CNF substrate. Figure (a) shows S_{21} plotted on a polar plot while (b) shows S_{11} plotted on a Smith chart under forward bias. Figure (c) shows S_{21} plotted on a polar plot while (d) shows S_{11} plotted on a Smith chart under reverse bias.*

Passive elements are crucial components that are used for various purposes, such as RF chokes and impedance matching networks in RF circuits. To demonstrate the full capability of the CNF substrate for microwave circuit application, simple metal–insulator–metal (MIM) capacitors and

spiral inductors were fabricated on a CNF substrate. Figure 6.12a presents the structure of the two passive elements on a CNF substrate with schematic illustrations. Bottom inductor metal and MIM capacitors, with 200 nm of TiO_2 as the dielectric material, were deposited on a releasable thin polyimide (PI, ~1 µm) sheet spin casted on a temporary Si substrate. Another polyimide layer

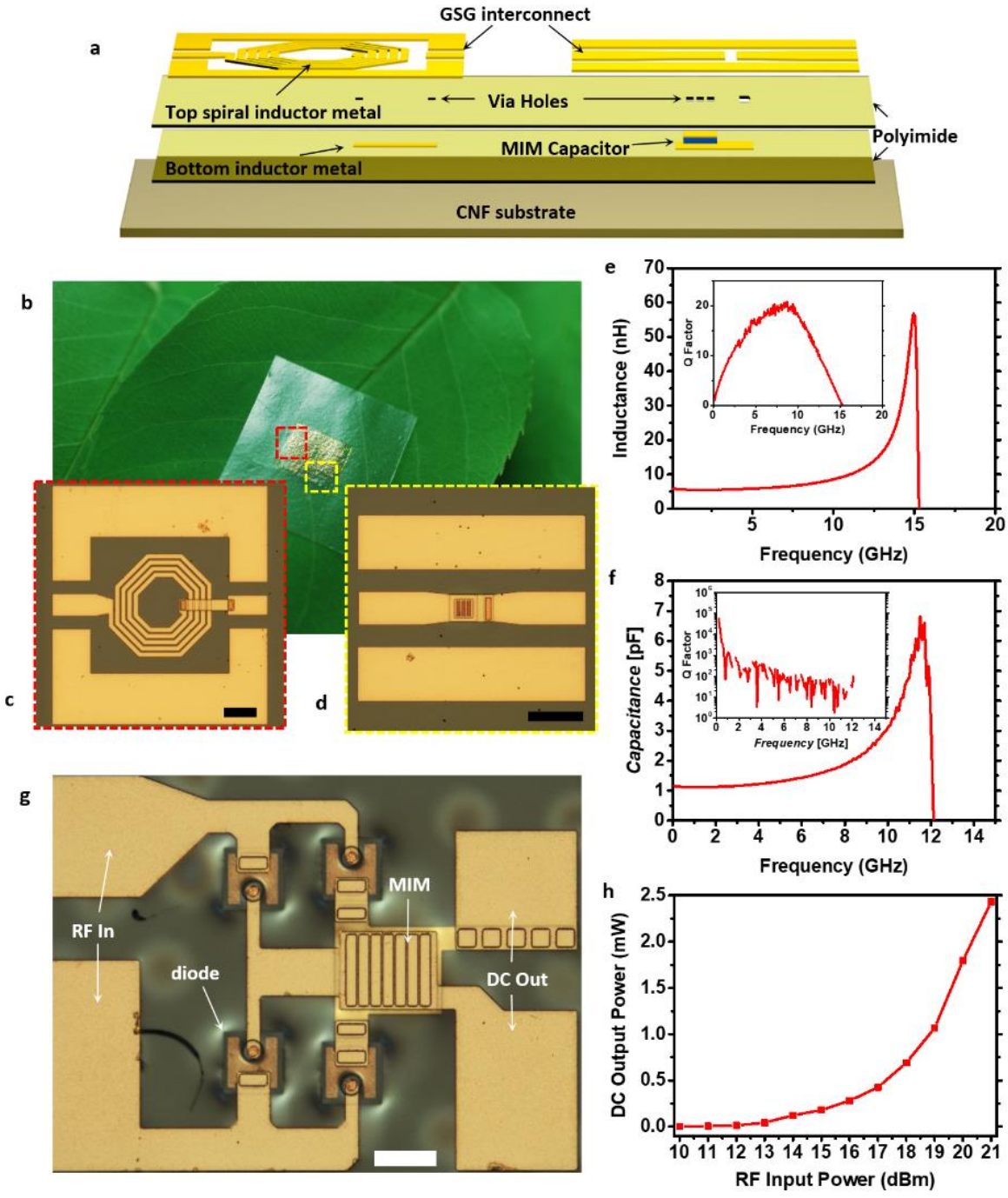

Figure 6.12. *Microwave passive elements and integrated circuit on CNF paper. (a) An exploded view schematic illustration of the inductor and capacitor on a CNF substrate. (b) Array of inductors and capacitors on a CNF substrate put on a tree leaf. (c) Optical image of the measured 4.5 turn inductor. Scale bar, 100 µm. (d) Optical image of the measured MIM capacitor. Scale bar, 100 µm. (e) Inductance plotted against frequency with an inset plot showing the inductor Q factor as a function of frequency. (f) Capacitance plotted against frequency with an inset plot showing the capacitor Q factor as a function of frequency. (g) An optical microscopy image of a full bridge rectifier built on a CNF paper. Here, the microwave Schottky diodes and an MIM capacitor were integrated. Scale bar, 50 µm. (h) Measured rectified DC output power of the rectifier while applying RF input power from 10 dBm to 21 dBm at 5.8 GHz.*

served as via holes during the subsequent metallization step for the G–S–G RF interconnects. The finished passive components were then released from the temporary substrate and transfer printed onto the CNF substrate. Figure 6.12b shows a photograph of the inductors and capacitors on a CNF substrate placed on a tree leaf. Figures 6.12c and 6.12d show the optical microscopy images of the measured inductor and capacitor, respectively. Measured S-parameters are plotted in Figure 6.13. The inductance of the 4.5 turn inductor versus frequency is plotted in Figure 6.12e. The width of the metal line of this inductor was 10 µm and the spacing between the adjacent metal lines was 5 µm. A constant inductance of ~6 nH was obtained up to ~8 GHz, with a self-resonant frequency (f_{res}) of 15.1 GHz. A peak Q value of ~20 was obtained at 8 GHz as shown in the inset image of Figure 6.12e. Figure 6.12f plots capacitance against frequency for a 30 × 30 µm^2 MIM capacitor with Q factor plotted in the inset image. A constant capacitance of ~1.3 pF was measured up to 6 GHz, with a f_{res} of 12.1 GHz. Such high Q and f_{res} values obtained at a broad frequency range

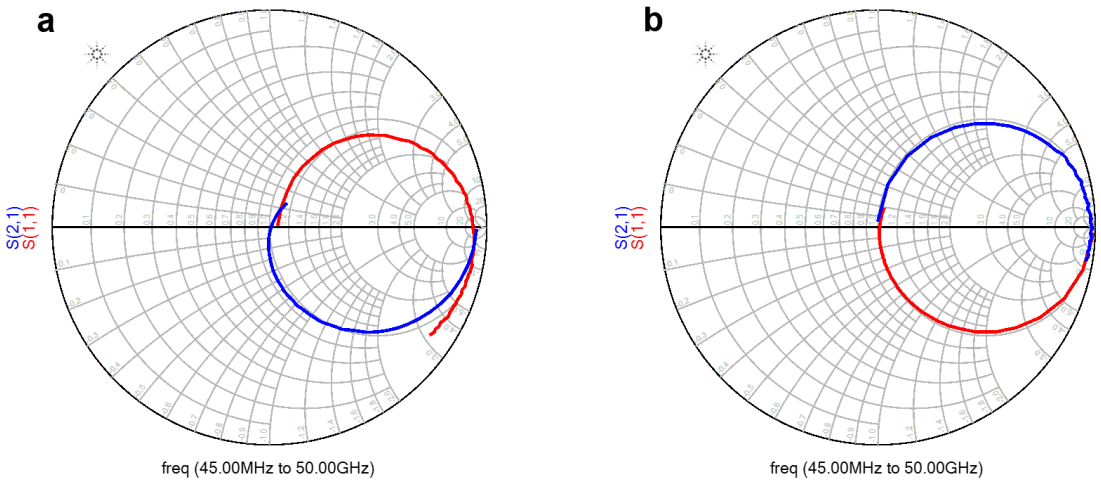

Figure 6.13. *(a) Measured S_{11} (red) and S_{21} (blue) of the inductor on CNF plotted on a Smith chart. (b) Measured S_{11} (red) and S_{21} (blue) of the capacitor on CNF plotted on a Smith chart.*

suggest that these inductors and capacitors are applicable for high speed RF integrated circuits, in conjunction with the microwave devices, on CNF substrates. To evaluate the printed microwave devices on a CNF substrate in an application, four microwave GaAs-based Schottky diodes and an MIM capacitor were combined into a simple integrated circuit to form a full bridge rectifier, as optically shown in Figure 6.12g with its circuit diagram shown in 6.14. The rectification behavior of RF-to-DC conversion at 5.8 GHz is shown in Figure 6.12h. This frequency is one of the popular

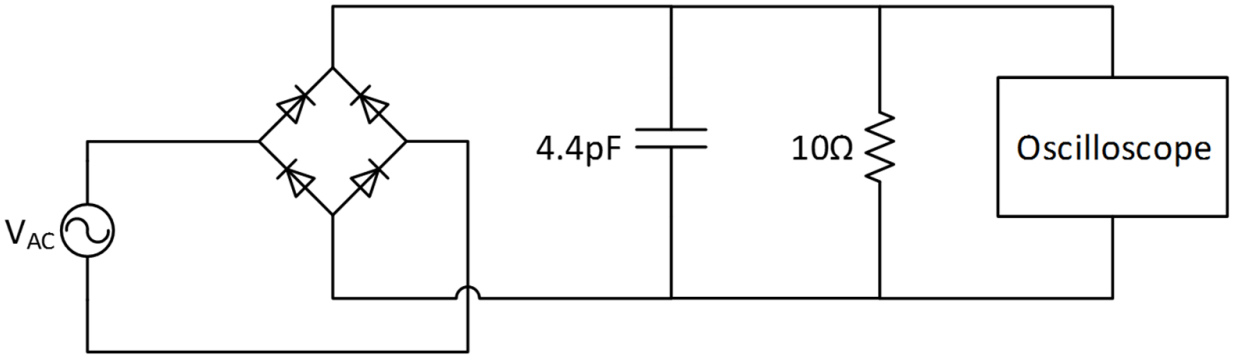

Figure 6.14. *Circuit diagram of the rectifier built on a CNF film*

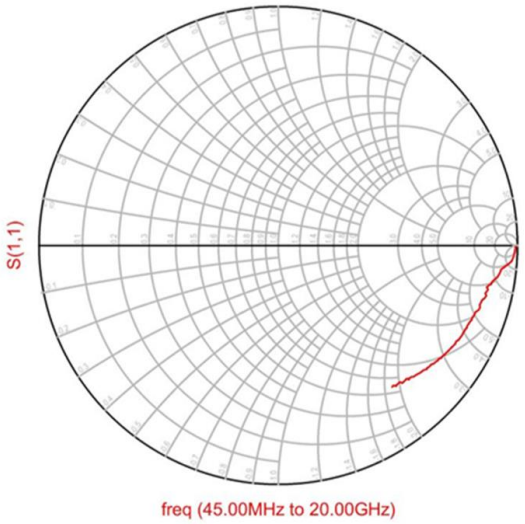

Figure 6.15. *Measured S_{11} of the rectifier at the RF input port plotted on a Smith chart.*

frequencies in wireless local area network (WLAN), commonly used in high speed Wi-Fi systems. As shown in the plot, the rectifier can rectify a 21 dBm input signal to an output power of 2.43 mW. The ability to rectify such high frequency signals can be attributed to the excellent electron mobility of GaAs and the low turn-on voltage of the Schottky diodes. With an appropriate matching network, the rectification ratio is expected to increase drastically by enhancing the reflection loss of the circuit. S_{11} of the rectifier is shown in Figure 6.15.

6.6. Silicon-based digital electronics on CNF substrates

In addition to microwave electronics that allow wireless communication for mobile electronic devices, digital circuits are also important components that are dominant in most electronic devices as microprocessors and controllers. Figure 6.16 summarizes a set of digital logic circuitries on a CNF substrate using Si-based complementary metal–oxide–semiconductor (CMOS) devices. Figure 6.16a shows the completed digital circuits on a CNF substrate, which includes ‘universal’

logic gates (Inverter, NOR gate, and NAND gate) and a full adder. The fabrication was done by separately printing Si nanomembrane-based p-type metal–oxide–semiconductor field-effect transistors (MOSFETs) and n-type MOSFETs onto a polyimide-coated temporary Si substrate, followed by deposition of gate oxides and metal interconnects for making CMOS-based digital

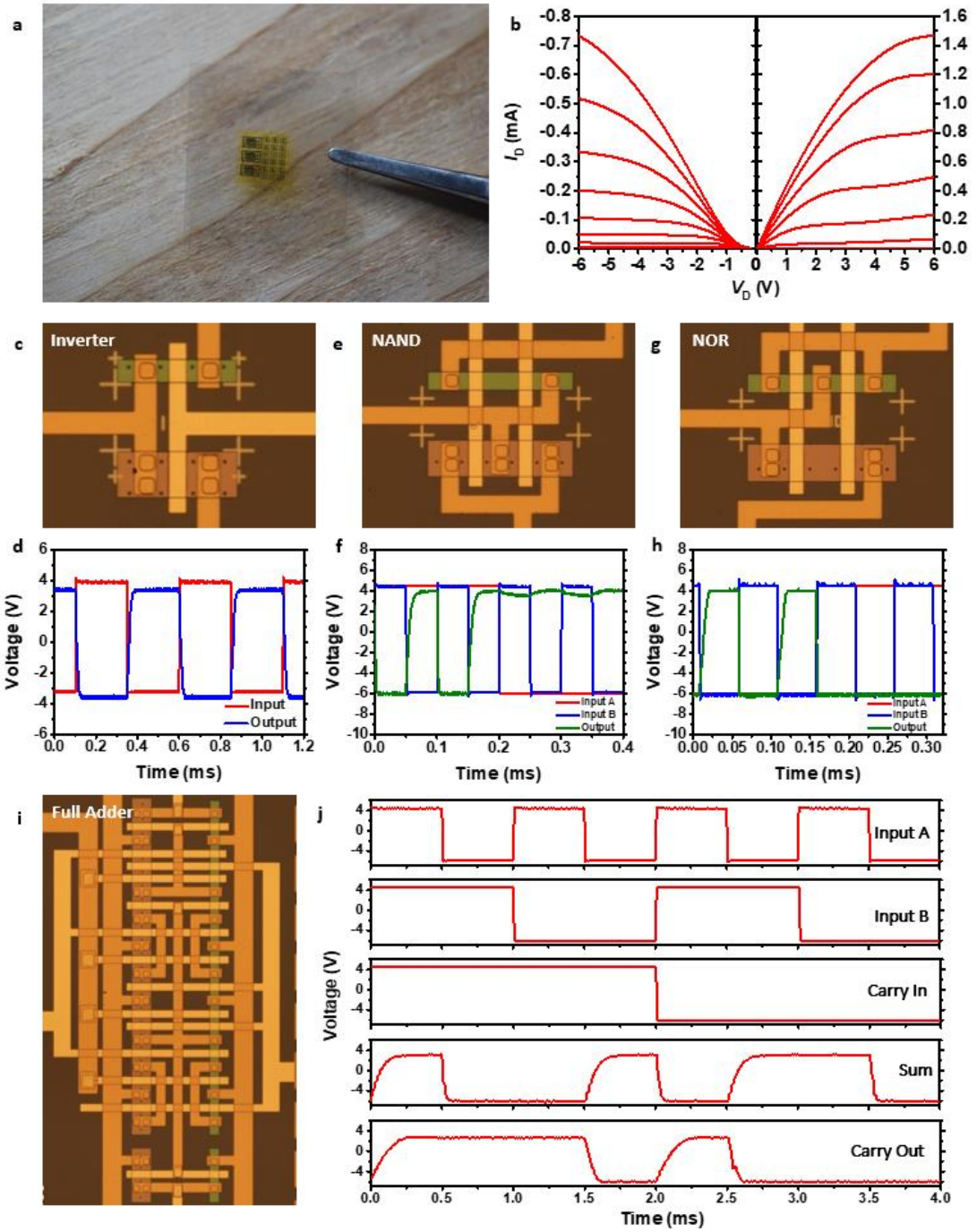

Figure 6.16. *Digital electronics on CNF paper. (a) A photograph of CNF paper with digital electronics. (b) I_D versus V_D plot of a p-type MOSFET (left) and an n-type MOSFET (right) at V_G steps of 1 V. (c) An optical microscopy image of an inverter. (d) Input–output characteristics of the inverter. (e) An optical microscopy image of a NAND gate. (f) Input–output characteristics of the NAND gate. (g) An optical microscopy image of a NOR gate. (h) Input–output characteristics of the NOR gate. (i) An optical microscopy image of a full adder. The adder consists of 28 transistors. (j) Characteristics of the full adder: Input A, Input B, Carry In, Sum, and Carry Out are shown in descending order.*

circuits. Figure 6.16b presents the current–voltage characteristics of the p-type MOSFET (left) and n-type MOSFET (right). Figure 6.16c shows an optical image of the CMOS inverter. As presented in Figure 6.16d, the inverter exhibits a good input and output relationship. A further modelling of these CMOS transistors established NOR and NAND logic gates, which are optically shown in Figures 6.16e and 6.16g, respectively. The input and output relationships of the NOR and NAND gates are shown in Figures 6.16f and 6.16h, respectively. The inputs and outputs can be seen as well-defined “0”s and “1”s. All of these components can be used together to yield a simple integrated circuit on a CNF substrate. As an example, a full adder, which is highly scalable and useful in many cascaded circuits, was designed and fabricated on a CNF substrate, as optically shown in Figure 6.16i. This full adder is a mirror full adder, which consisted of 28 transistors with 4 of them used for inverter construction. As presented in Figure 6.16j, the two single bit outputs (SUM and Carry Out) had a 0.2 ms switching delay when responding to the three single bit inputs (Input A, Input B, and Carry In). This made the full adder work at a frequency of up to 5 kHz.

6.7. Fungal biodegradation tests of the CNF-based electronics

As presented in Figures 6.4 to 6.16, all types of electronic systems required for building an electronic device can be realized on a CNF paper. To prove the concept of biodegrading electronic devices and to close the cycling loop that is shown in Figure 6.1a, one of the electronics that we have presented here was subjected to a fungal degradation test. Figure 6.17 summarizes a sequence of fungal degradation tests on CNF-based electronic devices. First, two different types of decay fungi, brown rot fungus *Postia placenta* and white rot fungus *Phanerochaete chrysosporium*, were considered and tested on the pure CNF substrate and on the epoxy-coated CNF substrate, without any electronics printed on them. Figure 6.17a presents the average weight loss percentages of these CNF-based films after 28 days. For each degradation test, five identical samples were degraded under the same conditions. Pure CNF samples showed a larger average weight loss (*Postia placenta*: 19.20%, *Phanerochaete chrysosporium*: 35.20%) compared to the epoxy-coated samples. While *Postia placenta* induced a slower degradation rate for pure CNF film, it caused a faster degradation for the epoxy-coated CNF film (*Postia placenta*: 9.96%, *Phanerochaete chrysosporium*: 6.60%) in comparison with *Phanerochaete chrysosporium*. Therefore, Postia placenta was chosen as the decaying agent for our CNF-based electronics that consisted of the epoxy-coated CNF film. The amount of epoxy in the epoxy-coated CNF film was 9.6% by weight. Figure 6.17b shows the weight loss result of digital electronics on CNF substrates after *Postia placenta* decaying for 84 days. Four replicas were made, and on average, the weight loss percentage was 12.25%, with a standard deviation of 5.43%, suggesting that the CNF film will fully degrade after an extended period of time. Figure 6.17c-e shows the images of the decaying process of an epoxy-coated CNF substrate with digital electronics against *Postia placenta*. Photos were taken after 6 hours, 10 days, 18 days, and 60 days as shown in Figures 6.17c and 6.17d. As

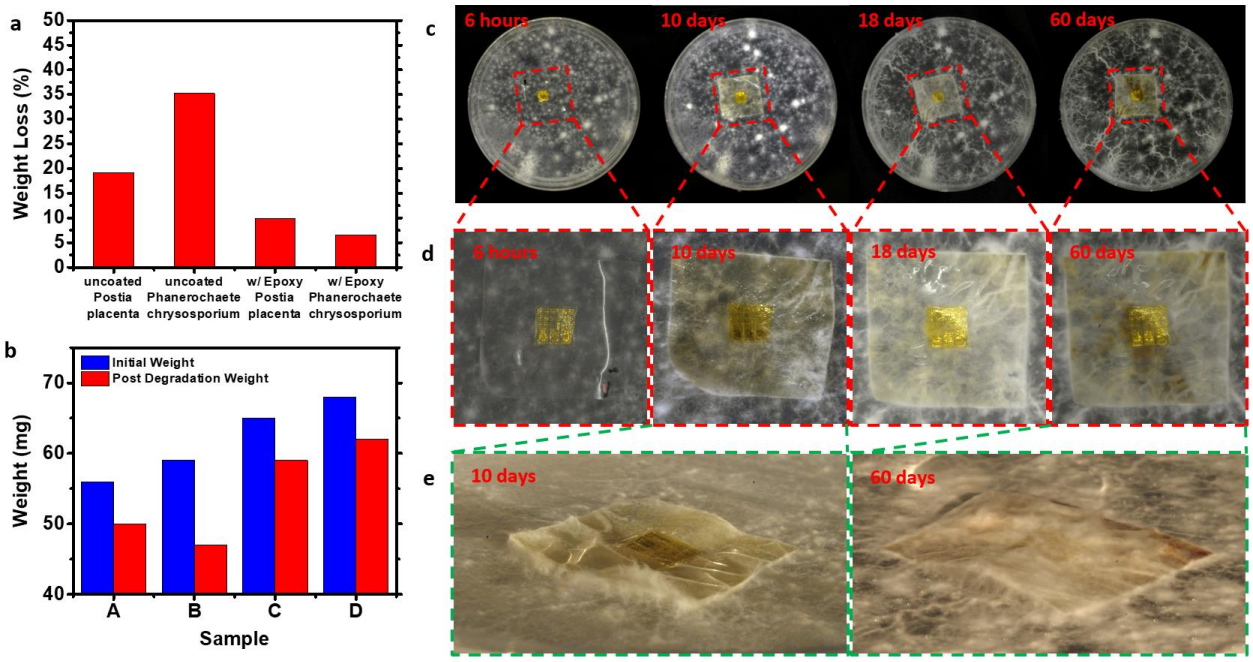

Figure 6.17. *Fungal biodegradation tests of the CNF-based electronics. (a) Fungal biodegradation tests of two types of CNF films. The left two bars show the percent weight loss for uncoated pure CNF films. The right two bars show percent weight loss for epoxy coated CNF films. The tests suggest that Postia placenta degrades the uncoated CNF films slower than Phanerochaete chrysosporium; however, Postia placenta degrades the epoxy coated CNF films faster than Phanerochaete chrysosporium. (b) Fungal biodegradation tests of digital electronics printed on top of the epoxy coated CNF films. Four samples were degraded with Postia placenta. (c) A series of photographs taken at 6 hours, 10 days, 18 days, and 60 days after starting the degradation process. (d) A series of magnified photographs of the CNF-based electronics during the degradation process. (e) Tilted view photograph of the CNF-based electronics after 10 days and 60 days of degradation. The fungus fully covers the film after 60 days.*

presented in Figure 6.17e, the fungi started to partially cover the sample after 10 days, and fully covered the sample after 60 days. Once degraded, the leftover electronics portion, which is

encapsulated in polyimide, can be collected to be further decomposed and recycled. Although polyimide can deteriorate with certain fungi, the degradation process is extremely slow compared to CNF, and because polyimide is generally non-permeable to water or solvents, it can be used to protect against any leakage of materials to the environment [43].

6.8. Experimental Section

Preparation of CNF paper: The tetramethylpiperidine-1-oxy (TEMPO) oxidized CNFs were refined in a microfluidizer processor (Microfluidics, Newton, MA), followed by filtering (Millipore Corporation, USA) under air pressure (0.55 MPa) with polytetrafluoroethylene (PTFE) membranes that have 0.1 μm pore sizes. Subsequently, the filter cake was separated from the membrane and sandwiched between layers of waxy coated paper, filter paper, and caul plates at room temperature for drying, followed by further drying in an oven at 60 °C for several hours. The dried CNF film was then coated with a bisphenol A based epoxy resin (Dow Chemical Company, 56:24:24 mixture of low viscosity epoxy resin, flexible epoxy resin, and amine-based curing agent) and pressed at 130 °C for ten minutes under a pressure of 100 psi.

Characterization of CNF paper: A contact angle goniometer (OCA 15/20, Future Digital Scientific Corp., USA) was used for the water contact angle measurements at ambient temperature. The volume of the water droplet was fixed at 4.0 μL, and the contact angle was determined 1 s after the water droplet was deposited on the surface of the CNF film. Three point flexural tests were conducted using a dynamic mechanical analyzer (DMA, TA Instruments RSA III, USA). Rectangular epoxy-coated CNF film (with a length of 40 mm, a width of 13 mm, and a thickness of 0.2 mm) was used for the flexural tests. The maximum flexural deflection was set at 5 mm for the tests. To measure transmittance, CNF film with a thickness of either 80 μm or 200 μm was

loaded onto a spectrophotometer (5000 UV-Vis-NIR, Cary). The system was set to transmission mode and the transmittance was recorded every 1 nm throughout the spectrum from 400 nm to 800 nm. The thermal stability of the epoxy coated CNF films were characterized via thermogravimetric analysis (TGA) using a TGA/Q50 thermal analyzer (TA Instruments, DE USA). Approximately 10 mg of the CNF films were heated from 30 to 600 °C at a heating rate of 10 °C min^{-1} in an N_2 atmosphere. Differential scanning calorimetry (DSC) was performed in an N_2 atmosphere using a DSC thermal analyzer (Auto Q20, TA Instruments) from 0 to 160 °C at a heating rate of 5 °C min-1 and a N_2 flow rate of 20 mL min^{-1}. The sample (~8.0 mg) was stored in a sealed aluminum pan. To measure the electrical breakdown characteristics, metal (Ti/Au, 10/200 nm) was evaporated on both sides of a 200 μm thick CNF film via a shadow mask, with a pad of 300 μm in diameter. High voltage was applied using a voltage source (2410 High-Voltage Source Meter, Keithley) through standard DC probing while the current was monitored. To measure the dielectric constant and loss tangent, the microstrip transmission line-approximation-method was used. A square CNF film with an area of 17.64 cm^2 was attached with a copper film as the ground on the back side, and a 6 mm wide copper tape as the transmission line on the center of the top side. S-parameters were collected through the SMA connectors as the RF signal was transmitted through the microstrip transmission line. The dielectric constant and loss tangent of the CNF film were then extracted according to the small signal circuit approximation.

Fabrication of high speed GaAs HBTs: The fabrication process began by depositing emitter finger metals (Pd/Ge/Au, 30/40/200 nm) using an electron-beam evaporator via a photoresist (AZ5214) lift-off process, followed by inductively coupled plasma etching (ICP-RIE, BCl_3/Ar = 10/5 sccm, pressure = 2 mTorr, plasma power = 50 W, inductor power = 500 W) of the cap and emitter layer. Another photoresist lift-off process to deposit base metal fingers (Ti/Pt/Au =

10/30/200 nm) and ICP-RIE etching using SiO_2 (800 nm) as a hard mask were carried out next to etch the sub-collector layer. After depositing collector metal fingers (Pd/Ge/Au = 30/40/200 nm), the sample was annealed at 450 °C for 30 seconds in ambient forming gas (H_2/N_2 = 5/95%) in a rapid thermal anneal (RTA) system for ohmic contact formation. Isolation of individual devices was done using ICP-RIE to etch the sub-collector layer and the underlying sacrificial layer. Protective anchors were patterned by spin casting a thick (~7.0 µm) photoresist layer (Megaposit SPR220, Rohm and Haas Electronic Materials) at 4000 rpm for 30 seconds, soft baked at 110 °C for 120 seconds, exposed to ultra-violet light at a dose of 500 mJ cm^{-2}, developed (MF-24A) for 120 seconds, and hard baked at 110 °C for 10 minutes. The AlGaAs sacrificial layer was undercut etched using diluted HF (1:100 = deionized water: 49% HF) for 3 hours.

Fabrication of GaAs Schottky diodes: A hard mask of SiO_2 (800 nm) was deposited via a lift-off process, followed by ICP-RIE etching of an n– GaAs layer to reach an n+ GaAs layer. Cathode metal (Pd/Ge/Au = 30/40/200 nm) was deposited next via a lift-off process and annealed in RTA (same conditions as the HBT RTA process) for ohmic contact formation. A Schottky metal (Ti/Pt/Au = 10/30/200 nm) was deposited on an n– GaAs layer for anode contact, followed by an ICP-RIE isolation process, patterning of the protective anchor, and sacrificial layer etching using the same procedures used for HBTs.

Preparation of the micro-stamp: A pattern of negative photoresist (SU8 50, Microchem, 100 µm) on a Si substrate was prepared for PDMS (Slygard 184, Dow Corning, 10:1 mixture of pre-polymer to curing agent) molding of an 80 × 80 μm^2 elastomer micro-stamp for selective transfer printing of the devices.

Fabrication of GaAs devices on a temporary substrate: On a Si substrate, a thin layer of sacrificial polymer, i.e., polymethyl methacrylate (950 PMMA A2, Microchem, 60 nm) was spin

casted, followed by hard baking at 180 °C for 3 minutes. A thin sheet of polyimide (PI, Sigma-Aldrich, ~1 μm) was spin casted at 5500 rpm for 60 seconds on the top, followed by soft bake at 80 °C for 25 seconds to create adhesion. Using a micro-stamp mounted on a modified mask aligner (MJB-3 aligner, Karl Suss), an HBT or a Schottky diode was transfer printed on the polyimide adhesive and hard baked at 130 °C for 3 minutes. A quick spray of acetone removed the protective anchor on the device, but left the polyimide undamaged. Another thin sheet of polyimide (~1 μm) was spin casted, followed by soft bake at 150 °C for 5 minutes and hard bake at 300 °C for 1 hour in a vacuum oven. Copper (100 nm) was deposited using an electron-beam evaporator with a lift-off process to serve as a hard mask to open via holes for the device contacts, followed by reactive ion plasma etching (RIE, CF_4/O_2 = 2/40 sccm, pressure = 300 mTorr, power = 200 W) of polyimide and wet etching of a copper mask (Copper Etch APS-100). G–S–G RF pads (Ti/Cu/Ti/Au = 10/1800/10/200 nm) were deposited via a lift-off process for DC and RF characterization of the devices.

Fabrication of passive devices on a temporary substrate: On a Si substrate with a PMMA sacrificial layer and a thin sheet of polyimide, a bottom inductor metal and capacitor metal (Ti/Au = 10/300 nm) were deposited via a lift-off process. Photolithography patterning on the bottom capacitor metal defined the capacitor size, where the dielectric material (TiO_2 = 200 nm) and top capacitor metal (Ti/Au = 10/300 nm) were deposited. With polyimide (~1 μm) spin casted, copper (100 nm) served as a hard mask to open via holes for a top spiral inductor metal and a G–S–G interconnect (Ti/Cu/Ti/Au = 10/1800/10/200 nm) deposited via a lift-off process.

Fabrication of microwave rectifier on a temporary substrate: Both Schottky diodes and MIM capacitors were integrated together by utilizing the same fabrication processes described above for these two types of devices.

Fabrication of digital electronics on a temporary substrate: n-type and p-type active regions for CMOS were prepared separately on the p-type (4×10^{15} cm^{-3}) and n-type (5×10^{14} cm^{-3}) silicon-on-insulator (SOI) wafers. Before ion implantation, 20 nm of thermal oxides (Tystar Oxidation Furnace) were grown on both n- and p-type SOIs for screen oxides. Uniform ion implantation was followed to slightly raise the doping concentration of the active region to minimize channel resistances and adjust the threshold voltage of the MOSFET. A short period of thermal annealing in a furnace was applied to recover the defects generated from implantation and activate the dopants. Heavy ion implantation was applied on the photolithography pre-defined source and drain region. After a second thermal annealing in the furnace, active regions on the SOI wafers were isolated using reactive plasma etching (Unaxis 790). The SOI wafers were then placed in a diluted HF (1:10) solution to etch the sacrificial buried oxide layer and release the membrane. Polyimide (~1 μm) was spin casted and cured on a 60 nm thick PMMA-coated Si wafer. A soft bake of 1 min at 100 °C dried out the solvent while maintaining the adhesive surface. Individually released membranes from each type of the SOIs were aligned and transferred separately onto the polyimide using a PDMS stamp mounted on a modified mask aligner, followed by hard bake at 300 °C for 1 hour in a vacuum oven. A standard source/drain metal pad, dielectric layer, via hole openings, and gate process for CMOS fabrication were processed on a temporary substrate. A second polyimide layer was coated on the surface for passivation and protection followed by via hole etching for the measurement pads.

Transfer printing electronics on a CNF substrate: The polyimide encapsulated devices (HBT, Schottky diode, inductor and capacitor, and digital electronics) on temporary Si substrates were boiled in acetone at 200 °C for two hours to remove the underlying sacrificial layer (PMMA). A large PDMS elastomer stamp was used to transfer print the finished devices onto the CNF substrate

with a thin layer of polymer (SU8 2000.5, Microchem, 500 nm) as the adhesive layer to ensure good bonding between the CNF substrate and the transferred devices.

Measurement and analysis: An Agilent N5225A PNA Network Analyzer was used to measure the S-parameter of the microstrip transmission line based on a CNF film. For the devices, the DC measurements were performed using an HP 4155B Semiconductor Parameter Analyzer, and RF measurements were performed using an Agilent E8364A PNA Series Network Analyzer. The measurement setup of the network analyzer was calibrated to the G–S–G probe tips using a standard Short-Open-Load-Thru (SOLT) calibration kit. HP 8350B Sweep Oscillator and 83592B RF Plug-in systems were used to provide RF power to the rectifier. The DC output signals were measured using a Rigol DS1102E oscilloscope with a 10 ohm resistor as the load. The S-parameters obtained from the RF measurements were analyzed using the Advanced Design System (ADS) software.

Fungal biodegradation tests of CNF-based electronics: To prepare for a fungal degradation test, the two decay fungi, *Postia placenta* (Fr.) M.Lars. and Lomb. (MAD 698) and *Phanerochyte chrysosporium* (ME461) were grown and maintained on 2% malt agar (DifCo, Detroit, MI) in petri dishes (15 × 100 mm). Inoculum was incubated at 27 °C in a 70% relative humidity (RH) room for 2 weeks to obtain confluent growth on petri dishes. Meanwhile, the CNF films or CNF-based electronics went through a 24 hour cleaning process in a propylene gas chamber. The cleaned samples were then laid on agar plates containing the confluent fungal growth according to American Wood Preserver's Association E-10-06 standard. Evaluations were observed at 6 hours, 10 days, 18 days, and 60 days for fungal growth on specimens; photographic records were obtained. Photographs were taken at time zero as a control.

Weight loss determination of degraded CNF substrate: Pure CNF and epoxy coated CNF

substrate specimens either with or without electronics were preconditioned in a 27°C, 65% RH conditioning room for two weeks. The weights were measured and recorded as the initial weight. Thereafter, specimens were loaded in petri dishes, allowing fungal growth and degradation in a 27°C, 70% RH room. At the end of 84 days (28 days for samples without electronics), specimens were harvested, fungal mycelia was brushed off, air dried for 48 hours, and reconditioned for 14 days. Weights were then measured and recorded as post degradation weight. Weight losses were then calculated and determined.

6.9. Conclusion

In summary, the feasibility of a sustainable, green chip concept that is applicable in both microwave and digital electronics, by strategically combining the minimum use of expensive, environmentally toxic semiconductor materials and the employment of microwave compatible, biodegradable CNF as substitutional substrates, was established. The demonstrated excellent performance GaAs-based HBTs and Schottky diodes, passive inductors and capacitors, and Si-based CMOS digital devices, “universal” logic gates and integrated full adders on CNF substrates, which are essential components in most typical electronic systems, share common fabrication techniques that can be easily integrated together. The combination of all of these thin-film form components into large scale integrated circuits on CNF substrates would provide ways to make many types of fully functional and ecofriendly electronics that could help reduce the accumulation of the massive amounts of persistent electronic waste disposed of daily and dramatically reduce the consumption of non-renewable natural resource. At the system level, there have been on-going efforts to reduce the use of toxic materials like lead, mercury, and arsenic that may be present in components such as batteries and displays [44-46]. These combined efforts will lead to a new

generation of more ecofriendly electronics.

6.10. Reference

[1] R. Geyer and V. D. Blass, "The economics of cell phone reuse and recycling," *International Journal of Advanced Manufacturing Technology,* vol. 47, pp. 515-525, Mar 2010.

[2] B. H. Robinson, "E-waste: An assessment of global production and environmental impacts," *Science of the Total Environment,* vol. 408, pp. 183-191, Dec 2009.

[3] J. A. Lorenzen, "Teaching and Learning Guide for: Green Consumption and Social Change: Debates over Responsibility, Private Action, and Access," *Sociology Compass,* vol. 9, pp. 519-529, Jun 2015.

[4] S. Pramila, M. Fulekar, and P. Bhawana, "E-waste-A challenge for tomorrow," *Research Journal of Recent Sciences,* vol. 1, pp. 86-93, Mar 2012.

[5] S. Needhidasan, M. Samuel, and R. Chidambaram, "Electronic waste–an emerging threat to the environment of urban India," *Journal of Environmental Health Science and Engineering*, vol. 12, p. 36, 2014.

[6] Q. Liu, J. Cao, K. Q. Li, X. H. Miao, G. Li, F. Y. Fan, *et al.*, "Chromosomal aberrations and DNA damage in human populations exposed to the processing of electronics waste," *Environmental Science and Pollution Research,* vol. 16, pp. 329-338, May 2009.

[7] S. E. Musson, K. N. Vann, Y. C. Jang, S. Mutha, A. Jordan, B. Pearson, *et al.*, "RCRA toxicity characterization of discarded electronic devices," *Environmental Science & Technology,* vol. 40, pp. 2721-2726, Apr 2006.

[8] J.-P. Colinge, *Silicon-on-Insulator Technology: Materials to VLSI: Materials to Vlsi*: Springer Science & Business Media, 2004.

[9] D. R. Webb, S. E. Wilson, and D. E. Carter, "Comparative Pulmonary Toxicity of Gallium-Arsenide, Gallium(Iii) Oxide, or Arsenic(Iii) Oxide Intratracheally Instilled into Rats," *Toxicology and Applied Pharmacology,* vol. 82, pp. 405-416, Mar 1986.

[10] D. Webb, I. Sipes, and D. Carter, "In vitro solubility and in vivo toxicity of gallium arsenide," *Toxicology and applied pharmacology,* vol. 76, pp. 96-104, 1984.

[11] T.-I. Kim, Y. H. Jung, H.-J. Chung, K. J. Yu, N. Ahmed, C. J. Corcoran, *et al.*, "Deterministic assembly of releasable single crystal silicon-metal oxide field-effect devices formed from bulk wafers," *Applied Physics Letters,* vol. 102, p. 182104, May 6 2013.

[12] H.-J. Chung, T.-I. Kim, H.-S. Kim, S. A. Wells, S. Jo, N. Ahmed, *et al.*, "Fabrication of Releasable Single-Crystal Silicon-Metal Oxide Field-Effect Devices and Their Deterministic Assembly on Foreign Substrates," *Advanced Functional Materials,* vol. 21, pp. 3029-3036, Aug 2011.

[13] R.-H. Kim, S. Kim, Y. M. Song, H. Jeong, T.-I. Kim, J. Lee, *et al.*, "Flexible Vertical Light Emitting Diodes," *Small,* vol. 8, pp. 3123-3128, Oct 2012.

[14] T.-I. Kim, M. J. Kim, Y. H. Jung, H. Jang, C. Dagdeviren, H. A. Pao, *et al.*, "Thin Film Receiver Materials for Deterministic Assembly by Transfer Printing," *Chemistry of Materials,* vol. 26, pp. 3502-3507, Jun 2014.

[15] D. Tobjork and R. Osterbacka, "Paper Electronics," *Advanced Materials,* vol. 23, pp. 1935-1961, May 3 2011.

[16] T. Kaneko, T. H. Thi, D. J. Shi, and M. Akashi, "Environmentally degradable, high-performance thermoplastics from phenolic phytomonomers," *Nature Materials,* vol. 5, pp. 966-970, Dec 2006.

[17] S.-W. Hwang, H. Tao, D.-H. Kim, H. Cheng, J.-K. Song, E. Rill, *et al.*, "A Physically

Transient Form of Silicon Electronics," *Science,* vol. 337, pp. 1640-1644, Sep 2012.

[18] S.-W. Hwang, X. Huang, J.-H. Seo, J.-K. Song, S. Kim, S. Hage-Ali, *et al.*, "Materials for Bioresorbable Radio Frequency Electronics," *Advanced Materials,* vol. 25, pp. 3526-3531, Jul 2013.

[19] S.-W. Hwang, D.-H. Kim, H. Tao, T.-I. Kim, S. Kim, K. J. Yu, *et al.*, "Materials and Fabrication Processes for Transient and Bioresorbable High-Performance Electronics," *Advanced Functional Materials,* vol. 23, pp. 4087-4093, Sep 2013.

[20] F. Eder, H. Klauk, M. Halik, U. Zschieschang, G. Schmid, and C. Dehm, "Organic electronics on paper," *Applied Physics Letters,* vol. 84, pp. 2673-2675, Apr 2004.

[21] Y. H. Zhou, C. Fuentes-Hernandez, T. M. Khan, J. C. Liu, J. Hsu, J. W. Shim, *et al.*, "Recyclable organic solar cells on cellulose nanocrystal substrates," *Scientific Reports,* vol. 3, Mar 2013.

[22] Y. H. Kim, D. G. Moon, and J. I. Han, "Organic TFT array on a paper substrate," *IEEE Electron Device Letters,* vol. 25, pp. 702-704, Oct 2004.

[23] H. Zhu, Z. Fang, C. Preston, Y. Li, and L. Hu, "Transparent paper: fabrications, properties, and device applications," *Energy & Environmental Science,* vol. 7, pp. 269-287, Jan 2014.

[24] M. Nogi and H. Yano, "Transparent nanocomposites based on cellulose produced by bacteria offer potential innovation in the electronics device industry," *Advanced Materials,* vol. 20, pp. 1849-1852, 2008.

[25] Z. Fang, H. Zhu, Y. Yuan, D. Ha, S. Zhu, C. Preston, *et al.*, "Novel nanostructured paper with ultrahigh transparency and ultrahigh haze for solar cells," *Nano letters,* vol. 14, pp. 765-773, 2014.

[26] M. Nogi, S. Iwamoto, A. N. Nakagaito, and H. Yano, "Optically transparent nanofiber

paper," *Advanced Materials,* vol. 21, pp. 1595-1598, 2009.

[27] H. Zhu, Z. Xiao, D. Liu, Y. Li, N. J. Weadock, Z. Fang, *et al.*, "Biodegradable transparent substrates for flexible organic-light-emitting diodes," *Energy & Environmental Science,* vol. 6, pp. 2105-2111, 2013.

[28] H. Zhu, Y. Li, Z. Fang, J. Xu, F. Cao, J. Wan, *et al.*, "Highly thermally conductive papers with percolative layered boron nitride nanosheets," *ACS nano,* vol. 8, pp. 3606-3613, 2014.

[29] K. Gao, Z. Shao, J. Li, X. Wang, X. Peng, W. Wang, *et al.*, "Cellulose nanofiber–graphene all solid-state flexible supercapacitors," *Journal of Materials Chemistry A,* vol. 1, pp. 63-67, 2013.

[30] J. Huang, H. Zhu, Y. Chen, C. Preston, K. Rohrbach, J. Cumings, *et al.*, "Highly transparent and flexible nanopaper transistors," *ACS Nano,* vol. 7, pp. 2106-2113, 2013.

[31] Y. Zhou, T. M. Khan, J.-C. Liu, C. Fuentes-Hernandez, J. W. Shim, E. Najafabadi, *et al.*, "Efficient recyclable organic solar cells on cellulose nanocrystal substrates with a conducting polymer top electrode deposited by film-transfer lamination," *Organic Electronics,* vol. 15, pp. 661-666, 2014.

[32] K. Nagashima, H. Koga, U. Celano, F. Zhuge, M. Kanai, S. Rahong, *et al.*, "Cellulose nanofiber paper as an ultra flexible nonvolatile memory," *Scientific Reports,* vol. 4, p.5532, 2014.

[33] T. Saito, M. Hirota, N. Tamura, S. Kimura, H. Fukuzumi, L. Heux, *et al.*, "Individualization of nano-sized plant cellulose fibrils by direct surface carboxylation using TEMPO catalyst under neutral conditions," *Biomacromolecules,* vol. 10, pp. 1992-1996, 2009.

[34] M. Doğan, S. Erdoğan, and E. Bayramlı, "Mechanical, thermal, and fire retardant properties of poly (ethylene terephthalate) fiber containing zinc phosphinate and organo-

modified clay," *Journal of Thermal Analysis and Calorimetry,* vol. 112, pp. 871-876, 2013.

[35] M. V. Novello, L. G. Carreira, and L. B. Canto, "Post-consumer polyethylene terephthalate and polyamide 66 blends and corresponding short glass fiber reinforced composites," *Materials Research,* vol. 17, pp. 1285-1294, 2014.

[36] S. M. Ardekani, A. Dehghani, M. A. Al-Maadeed, M. U. Wahit, and A. Hassan, "Mechanical and thermal properties of recycled poly (ethylene terephthalate) reinforced newspaper fiber composites," *Fibers and Polymers,* vol. 15, pp. 1531-1538, 2014.

[37] J. Masum, P. Parmiter, T. Hall, and M. Crouch, "Current analysis of polyimide passivated InGaP/GaAs HBT," *IEE Proceedings-Circuits, Devices and Systems,* vol. 143, pp. 307-312, 1996.

[38] J. S. Wang and C. M. Wai, "Arsenic in drinking water—a global environmental problem," *J. Chem. Educ,* vol. 81, p. 207, 2004.

[39] H. Kawamura, K. Sakuno, T. Hasegawa, M. Hasegawa, H. Koh, and H. Sato, "A miniature 44% efficiency GaAs HBT power amplifier MMIC for the W-CDMA application," in *GaAs IC Symposium, 2000. 22nd Annual*, 2000, pp. 25-28.

[40] Y. Shimazaki, Y. Miyazaki, Y. Takezawa, M. Nogi, K. Abe, S. Ifuku, *et al.*, "Excellent thermal conductivity of transparent cellulose nanofiber/epoxy resin nanocomposites," *Biomacromolecules,* vol. 8, pp. 2976-2978, 2007.

[41] R. Carlson, G. Slack, and S. Silverman, "Thermal Conductivity of GaAs and GaAs1− x P x Laser Semiconductors," *Journal of Applied Physics,* vol. 36, pp. 505-507, 1965.

[42] C.-E. Huang, C.-P. Lee, H.-C. Liang, and R.-T. Huang, "Critical spacing between emitter and base in InGaP heterojunction bipolar transistors (HBTs)," *IEEE Electron Device Letters,* vol. 23, pp. 576-578, 2002.

[43] J.-D. Gu, "Microbiological deterioration and degradation of synthetic polymeric materials: recent research advances," *International biodeterioration & biodegradation,* vol. 52, pp. 69-91, 2003.

[44] Apple. *MacBook Pro - The world's greenest lineup of notebooks.* . Available: https://www.apple.com/macbook-pro/environment/

[45] S.-J. Chun, E.-S. Choi, E.-H. Lee, J. H. Kim, S.-Y. Lee, and S.-Y. Lee, "Eco-friendly cellulose nanofiber paper-derived separator membranes featuring tunable nanoporous network channels for lithium-ion batteries," *Journal of Materials Chemistry,* vol. 22, pp. 16618-16626, 2012.

[46] L. Yin, X. Huang, H. Xu, Y. Zhang, J. Lam, J. Cheng, *et al.*, "Materials, designs, and operational characteristics for fully biodegradable primary batteries," *Advanced Materials,* vol. 26, pp. 3879-3884, 2014.

CHAPTER 7
Micro-structured photoreceptor scaffolds for modeling and therapeutic applications

Photoreceptors are the gatekeepers of vision, and they capture photons and transduce them into electro-chemical signals to be processed within the retina and visual centers of the brain. Blinding disorders of the outer retina involve dysfunction and often degeneration of the photoreceptors, as occurs in many forms of *retinitis pigmentosa*. One broadly applicable treatment strategy would be to replace photoreceptors, which are highly polarized, specialized cell types with apical outer segments containing light sensing photopigments and basal axon terminals. Here, we present novel and robust techniques to create polymer-based, complex structures in an ultrathin, implantable format. A uniquely designed polymer membrane was developed to study seeding, survival and polarization of human stem cell-derived photoreceptors. The biocompatible film was created using polydimethylsiloxane (PDMS) and patterned with an array of unique through-holes to allow photoreceptor axon egress. The ability to create such micro-scale structures allows individual photoreceptors to be placed in a reservoir in a dense array format and provides the necessary cellular and structural cues for photoreceptor polarization. Once placed, the photoreceptors start to extend axons with appropriate synaptic markers through the vertical micro-scale through-holes, placing them in an optimal position for subretinal transplantation. The findings from these experiments provide a foundation for improving photoreceptor-based models and strategies for generating and delivering implantable patch grafts of human photoreceptors for the treatment of multiple blinding disorders.

7.1. Introduction

No treatment options exist for most patients with blinding disorders of the outer retina, particularly at advanced stages of disease. Recent advances in human pluripotent stem cell (hPSC) technology may offer promising replacement therapy for such patients, including those with retinitis pigmentosa (RP) and age-related macular degeneration (AMD), both of which involve the loss of either photoreceptor (PR) cells alone or in combination with retinal pigment epithelium (RPE) cells [1-3]. hPSCs are stem cells that can differentiate into any cell in the body, including retinal cells. Although clinical trial of replacement therapy for hPSC-derived RPE is already underway, replacement of PR that is ultimately responsible for abovementioned disorders remains untested. Inside the thin layer of retina, regularly and densely spaced PRs are vertically oriented towards the cornea to sense light that is coming in through the corneal lens. For patients with damaged PR, bolus injection of these cells provides little benefit to restoring vision. Experimental studies of transplanted cells indicated survival and integration of injected PR in the rat subretinal space, but significant cell reflux from the subretinal space and appearance of disorganized masses of transplanted cells were observed. Most of all, PRs will not polarize or form specialized processes such as outer segments on a 2-D surface, but will do so in limited fashion when grown as 3-D structures [4]. To overcome this challenge, we generated a 3-D, micro-patterned, and biocompatible scaffold that mimics the outer retinal structure, which can guide the growth of PR *in vitro* and be transplanted with oriented PRs. The biocompatible film based on polydimethylsiloxane (PDMS) [5, 6], patterned with an array of cell capturing reservoirs and through-holes was prepared. Figure 7.1 shows the cross section view of the scaffold where the top half-spherical reservoir was used to contain PRs and bottom through-holes were used to guide the cell growth. The ability to create micro-scale structures allowed individual PR to be placed in a

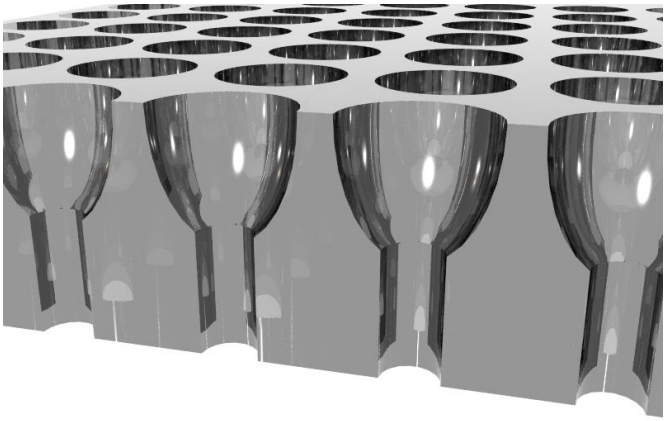

Figure 7.1. *Schematic illustration of the micro-structured scaffold capable of capturing photoreceptor cells in the upper reservoir and guiding their growth of endings towards the through-holes.*

reservoir in a dense array format. Culturing PRs in this format provided the necessary cellular and structural cues for PR polarization. Once placed, the PRs started to grow their endings towards the vertical micro-scale through-holes. These polarized PRs can then be poised for transplantation (i.e. outer segments at one end and axon terminals at the other).

7.2. Fabrication and evaluation of micro-structured scaffold

The fabrication process flow of the micro-structured retinal scaffold is described via schematic illustrations in Figure 7.2. Array dimensions were chosen such that each reservoir captures one to several cells and each through-hole allows the cells to grow their endings through and prevent cells from sagging down. Detailed dimensions of the scaffold are presented in Figure 7.3. Scaffolds were generated by patterning arrays of micro-scale circular patterns on a silicon (Si) wafer via a photolithography process, followed by combination of isotropic and anisotropic reactive ion etching. Using a single photoresist mask, the upper reservoir region was created first with an

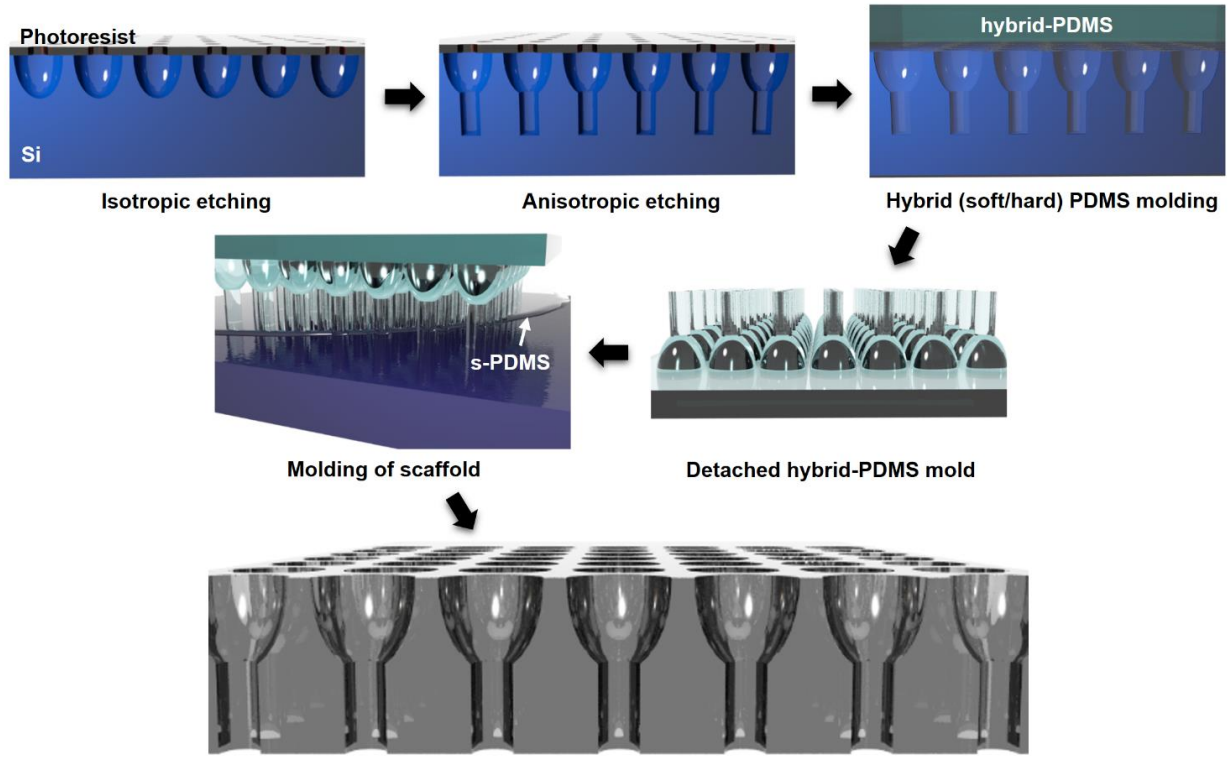

Figure 7.2. *Schematic illustration for fabricating micro-structured scaffold using microfabrication techniques combined with soft molding.*

isotropic etching process and the cylindrical vertical hole was then created using an anisotropic Bosch process. After the etched Si wafer was cleaned thoroughly with organic solvents and plasma ashing, it was coated with a thin layer of Teflon to generate hydrophobic surface condition. Once

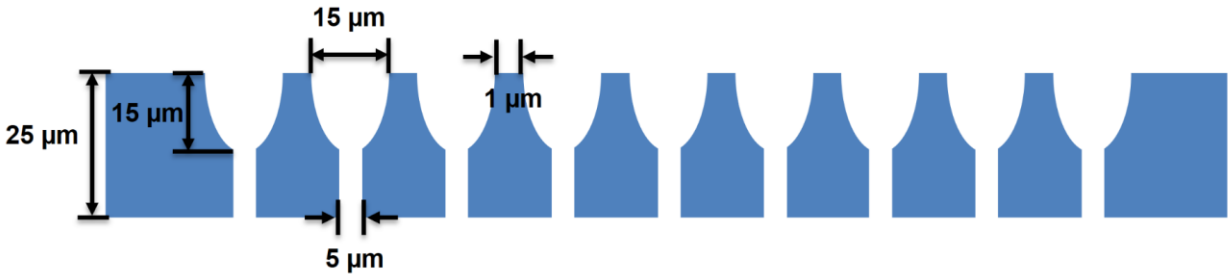

Figure 7.3. *Cross-section view schematic illustration of the micro-structured scaffold showing the detailed dimensions*

the Si surface was treated to become super-hydrophobic, a thin layer (~30 µm) of hard (h)-PDMS was spin-casted and cured. h-PDMS was prepared by mixing and degassing 3.4 g of vinyl PDMS prepolymer (VDT-731, Gelest Corp.), 18 µL of a Pt catalyst (platinum-divinyltetramethyl-disiloxane complex, SIP6831.2LC, Gelest Corp.), and 50 µL of modulator (2,4,6,8-Tetramethyl-2,4,6,8-tetravinylcyclotetrasiloxane, Sigma-Aldrich). A hydrosilane prepolymer (HMS-301, Gelest Corp.) was introduced to the mixture before coating onto the Si wafer, which hardened the h-PDMS slowly [7]. Next, a thick layer (~3 mm) of soft (s)-PDMS was poured and cured to allow easier handling during delamination. The s-PDMS used for this study was Dow Corning's Sylgard 184, a silicone elastomer largely favored for medical implants. Here, the h-PDMS prevents the

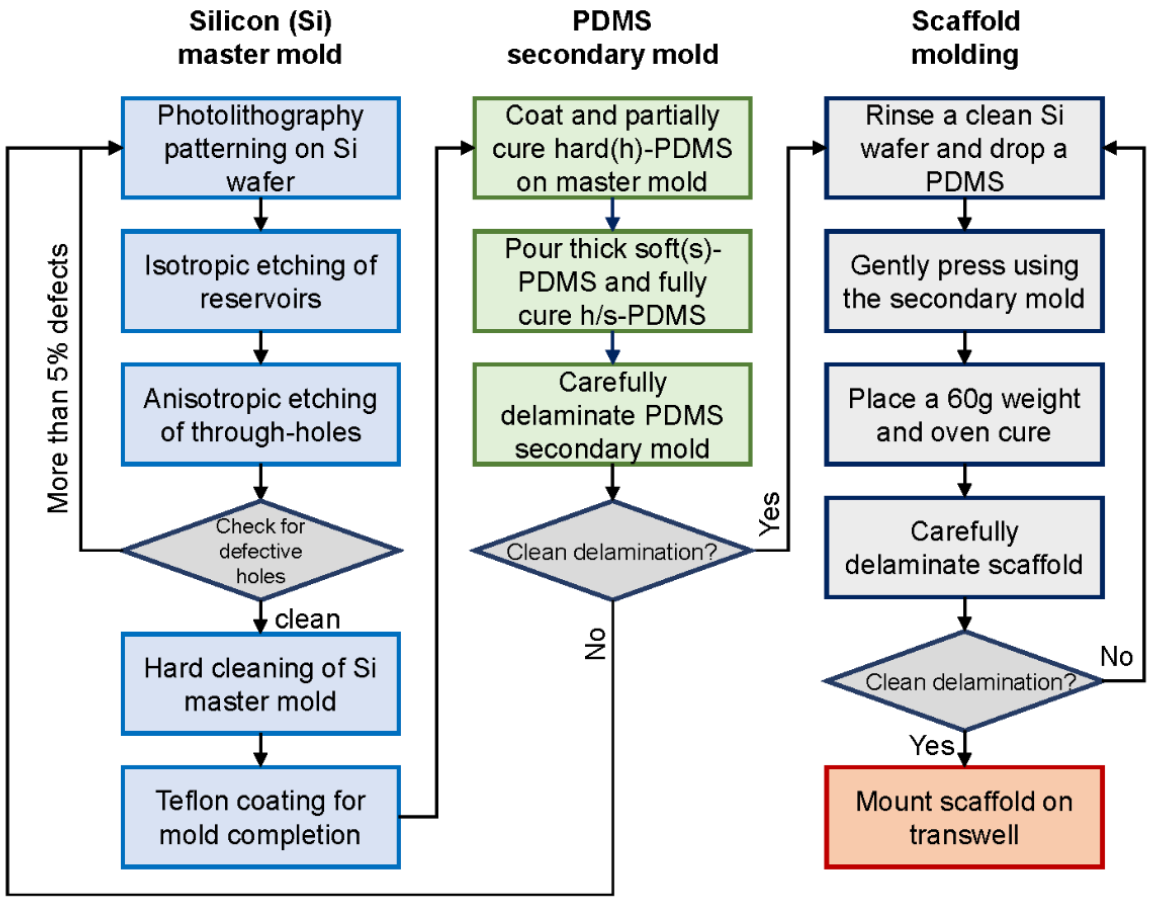

***Figure 7.4**. Process diagram of fabricating micro-structured scaffold.*

molded structures from deforming, buckling, or collapsing, while the thick s-PDMS acts to support the thin layer of h-PDMS. Careful delamination of the hybrid PDMS from the etched Si wafer led to a robust secondary mold for creating scaffolds. Subsequently, the hybrid PDMS mold was further treated with self-assembled monolayer (SAM) of silane using vacuum evaporation to prepare for molding. Treating the surface of the mold with judiciously selected silane prevented the ultrathin scaffold from bonding to the mold. Thereafter, a Si wafer was pressed on the mold, where a drop of s-PDMS was filled with capillary force and cured in an oven. This would form the structure of thin-film scaffold. Once the s-PDMS was fully cured, the resulting thin s-PDMS-based scaffold was delaminated carefully from the mold. A schematic diagram describing the process flow of the fabrication process is presented in Figure 7.4.

The scaffold was evaluated for biocompatibility with various measures, including optical, mechanical, and thermal evaluations. It is impossible to evaluate the micro-structures of the scaffold using optical microscopes, so scanning electron microscopes (SEM) were used to evaluate the structures and check the defects that may have resulted from external particles. SEM images of the top, bottom, and cross-section view of the resulting PDMS scaffold are presented in Figures 7.5a, 7.5b, and 7.5c respectively. Because the eye is in spherical geometry, the transplantable

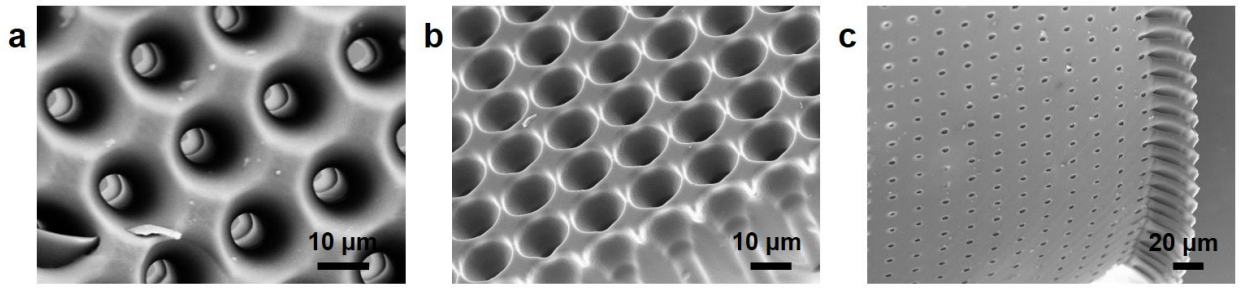

Figure 7.5. *Scanning electron microscope images of the micro-structured scaffold showing (a) top-view, (b) cross-section view, and (c) bottom-view.*

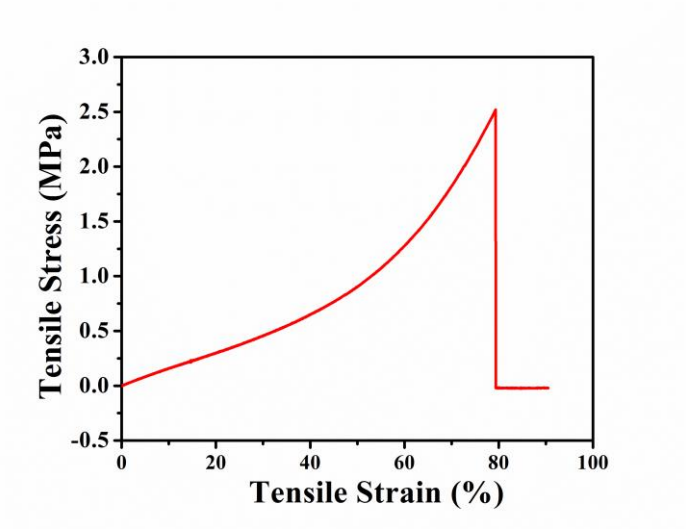

Figure 7.6. *Tensile stress vs. tensile strain curve measured for PDMS micro-structured scaffold.*

scaffold must be flexible and stretchable in order to contact seamlessly to the curvilinear sub-retinal surface. Therefore, tensile stress was measured on the thin film scaffold as shown in Figure 7.6. The mechanical Modulus of the scaffold was measured to be 1.49 MPa, which is significantly lower than that of bulk PDMS film due to empty spaces laid across the scaffold and is a suitable modulus for transplantation. Finally, cell seeding requires absolutely sterile substrate, which is often achieved by long ethanol soaking and/or high-temperature autoclaving process. Autoclave alone is a common method of sterilization for medical devices for clinical use. Our scaffold did not deform or change in anyway after standard ethanol soaking and autoclave procedure were applied, as presented in Figure 7.7. Approved scaffolds after the evaluations were mounted on a transwell for *in vitro* cell seeding and growth.

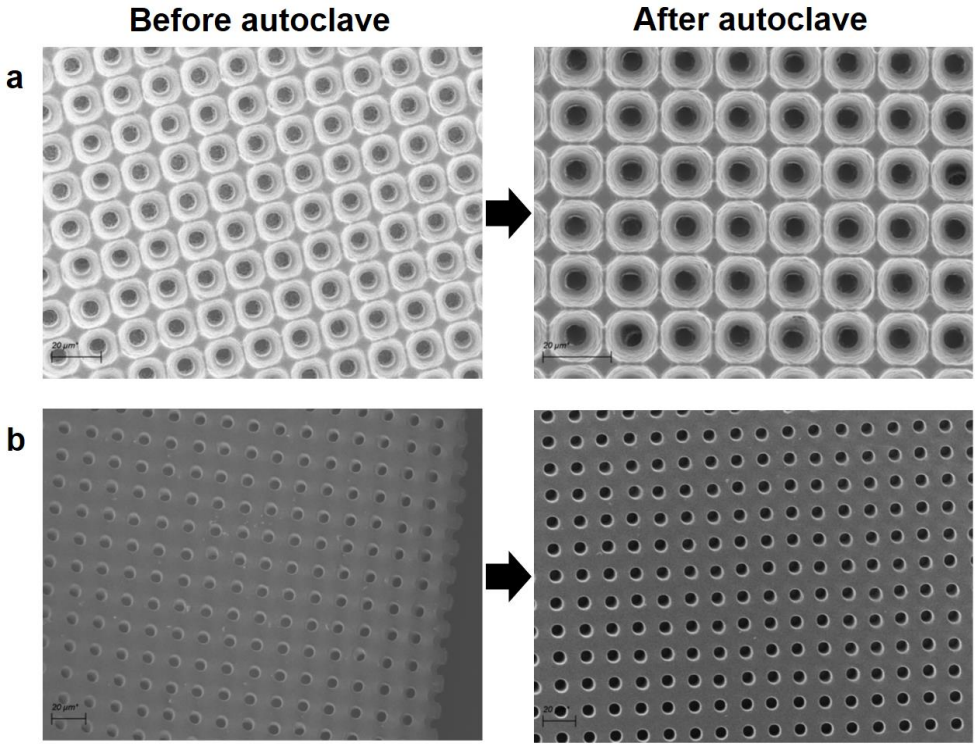

Figure 7.7. *Scanning electron microscope images comparing the micro-structured scaffold before and after the autoclave process. (a) compares the top surface and (b) compares the bottom surface of the scaffold.*

7.3. Cell preparation and seeding on scaffold

We have generated and purified hPSC-derived optic vesicle (OV) structures that consist of a pure population of retinal progenitor cells (RPCs) [4, 8-10]. Figures 7.8a-f show the images of this preparation process, where a high yield of PR precursors was observed at day 80. Briefly, between days 20-30, OVs were mechanically selected based upon their distinct morphology (Figure 7.8a and 7.8c), including a phase bright ring and pseudostratified epithelium. At this stage, all RPCs were positive for VSX2, a specific marker of this cell type (Figure 7.8d). To monitor PR production in live cultures, we used a Cone Rod Homeobox (CRX) reporter line that expresses the fluorophore tdTomato at all stages of PR differentiation [11]. Following differentiation, RPCs gave rise to all

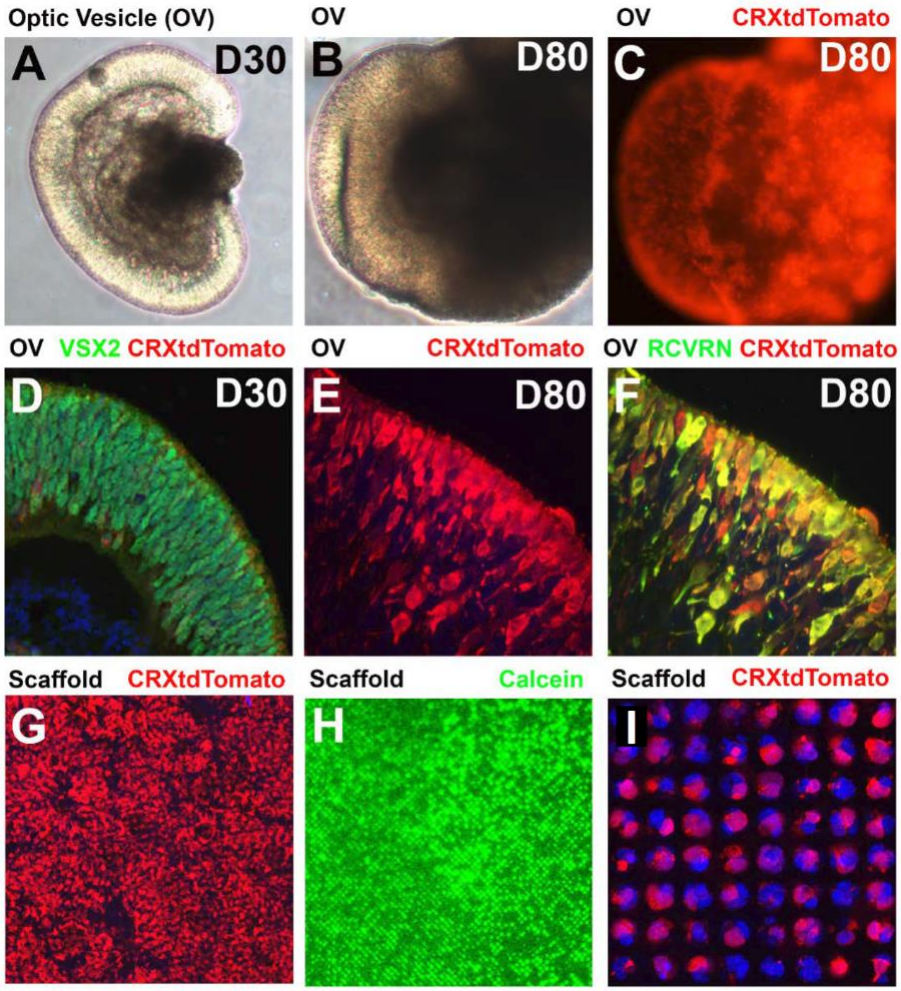

Figure 7.8. *Cell preparation and seeding on scaffold. Live tracking of photoreceptor production with optic vesicle (OV) at (a) day 30 and at (b) day 80. (c) At day 80, the OV expresses fluorophore tdTomato using Cone Rod Homeobox (CRX) reporter line. (d) Image of the OV where the retinal progenitor cells (RPC) were positive for VSX2 at day 80. (e) RPCs gave rise to all neural retinal cell types, (f) including 50%-80% PRs that also co-express the PR marker RCRVN at day 80. (g)-(i) Top view mages showing successful cell culture on the scaffold.*

neural retinal cell types, including 50%-80% PRs that also co-express the PR marker RCRVN (Figures 7.8e and 7.8f). For experiments, PR precursors (80 days of differentiation) were used as

this stage of PR differentiation has been shown to have the highest degree of integration in mouse allografts. Precursors are more plastic than fully differentiated PRs, and are more likely to integrate into the host. Single cells were obtained by dissociating OVs with papain. Such carefully generated PRs were then seeded onto the scaffold. Calcein labeling showed good cell survival at one week post plating (Figure 7.8g-i).

7.4. Post seeding results

The unique half sphere design of the wells provided excellent initial cell capture, however a substrate for the cells to form junctional complexes with was vital for cell adherence. For cell adhesion enhancement, laminin was chosen as an adhesion promoting polymer to encourage good binding of PRs to the scaffold. Wettability control becomes necessary at such micro-scale structures, due to the water-repellency effect that would leave bubbles on each reservoir without any surface treatment [12, 13]. In addition, because PDMS will present hydrophobic surface after hardening, it is essential to modify the surface chemistry so that polar solvents, like water and cell containing media will adhere well and wet the surface. Adding silanol (SiOH) groups to the surface can alter the surface chemistry, which can be achieved by either exposing ultraviolet light with ozone (UVO) or by activating via plasma oxidation. Figure 7.9 shows fluorescent imaging of the seeded cells and compares the plating conditions. For all three conditions, laminin was coated before cell seeding. Without any treatment, poor cell culturing was observed as the laminin itself could not be coated uniformly, as shown in Figure 7.9a. Under 2 min of UVO treatment, there was slight improvement in laminin adhesion, but the cells did not adhere well to the surface, as shown in Figure 7.9b. In contrast, a brief oxygen plasma (15 sec) activated the surface of the PDMS-based scaffold and ensured thorough coating of laminin and uniform culturing of cells, as shown

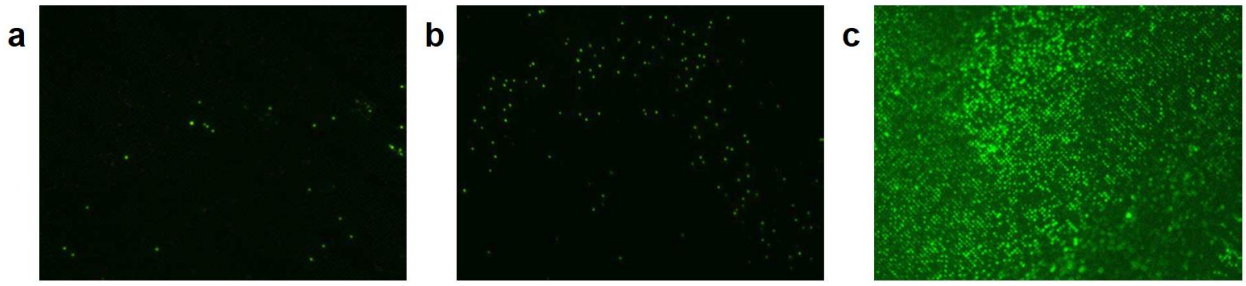

Figure 7.9. *Comparison images showing the cell culture density with different surface conditions of the PDMS scaffold. Calcein labeling of the seeded scaffold with (a) no treatment, (b) ultraviolet light and ozone treatment, and (c) oxygen plasma treatment.*

in Figure 7.9c. While UVO is an excellent method to activate or clean a surface and introduce hydrophilic treatment, it is less aggressive (in terms of terminating CH_3 groups) and slower than plasma oxidation. Moreover, the surface treated PDMS scaffolds were sterilized for 24 hours in ethanol solution, followed by high-temperature autoclaving process. As a result, the poor laminin/cell adhesion for UVO treated scaffold is attributed to the loss of hydrophilicity after the sterilization processes, whereas the stronger plasma treated scaffold could maintain hydrophilicity even after the sterilization process was completed. As seen from the comparison, without surface activation, laminin did not adhere well to the scaffold, resulting in a loss of most of the seeded cells.

Figure 7.10 shows the polarization of cells in the scaffold. Single plane confocal images were taken 9 days post seeding from different angles to observe the cell density. A high-density of cells was observed from the top view. Imaging the cells at the level of wells, it is clear that the cells have been captured into an array format. Bottom view confirms the cells have not sagged down and escaped through the vertical through-holes, and confirms the extension of axonal processes down the through-holes. A seeding density of 1.8×10^4 mm^2 was deemed optimal for cell capture.

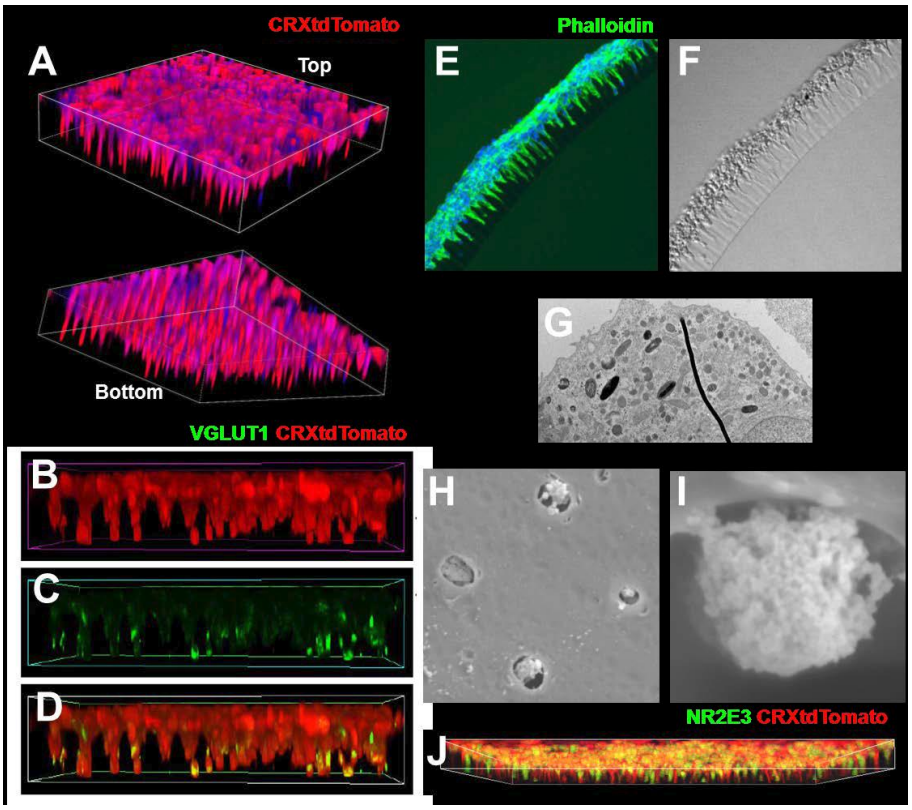

Figure 7.10. *Images showing the polarization of seeded cells on the micro-structured scaffold. (a) 3-D top and bottom views of the scaffold with seeded cells. (b)-(d) Cross-section view of the seeded cells showing the axons primed for synapse formation via the expression of VGLUT1 at the axon tips. (e),(f) Phalloidin labels cytoskeleton F-actin thin filaments that are present in PR axon terminals. (g) Transmission electron microscope image of the seeded scaffold showing the generation of mitochondria rich outer segments along the apical surface of the scaffold (h),(i) Scanning electron microscope images of the bottom of the scaffold showing the axon extending out of the through-holes. (j) Cross-section view of the seeded cells after 3 months.*

Figure 7.10a shows 3-D top and bottom views of the scaffold. These images demonstrate axon extension through the micro-c hannels of the scaffold. Many of the axons were primed for synapse formation as shown by the expression of VGLUT1 at the axon tips (Figure 7.10b-d). Phalloidin

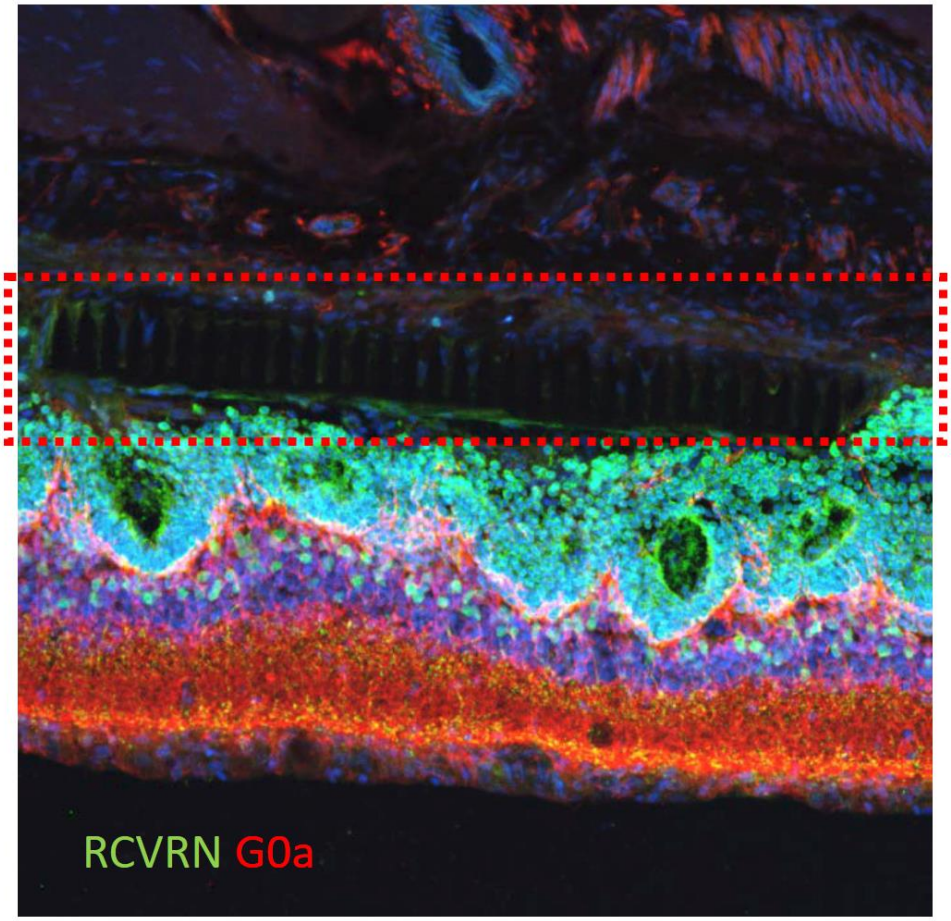

Figure 7.11. *Image of the transplanted scaffold with seeded cells in a rat, taken at 2 weeks post transplantation. Dotted line shows the position of the scaffold.*

labels cytoskeleton F-actin thin filaments that are present in PR axon terminals (Figure 7.10e and 7.10f). Transmission electron microscope (TEM) analysis shows the generation of mitochondria rich outer segments along the apical surface of the scaffold (Figure 7.10g), while scanning electron microscope (SEM) demonstrates axon extension out of the through-holes (Figure 7.10h-i). Importantly, PRs can survive long-term (3 months) on scaffold *in vitro*, as shown following three months of culture in Figure 7.10j. Furthermore, PR differentiation can occur in vitro on the scaffolds, as shown by rod-specific NR2E3 expression (Figure 7.10j).

Initial transplantations of the scaffold alone into the rat retina suggests tolerability of the scaffold in the subretinal space of WT rats (Figure 7.11). The scaffold can be inserted into the rat subretinal space and had minimal impact on the host retina. Some glial activation was noted with GFAP labeling, however no thick glial scar was noted around the transplant at 2 weeks. Some host PR disruption was noted in the WT retina (RCVRN labeling), however second order neurons were intact (GOa). Further testing is underway to evaluate transplantation of PR seeded scaffolds in degenerate rat models.

7.5. Conclusion

A scaffold that promotes PR organization and is biocompatible and readily transplantable into the subretinal space is achieved using cutting edge microfabrication techniques. This PR scaffold constitute the first product capable of organized PR delivery and replacement. The findings achieved from the experiments establish important advances in the behavior of retinal cells that could not be understood before and aid in modelling the tissue-level retinal structure for future implantable artificial systems. In addition, the utilization of microelectronics manufacturing techniques that can create complex structures in micro- and nano-scale was highly advantageous for fabrication of scaffolds that mimic the structure of biological tissues or organs. Further combinations of diverse microfabrication techniques with biocompatible thin films would allow building of complex geometries in biomedical transplants for other parts of the body which were difficult to achieve with conventional strategies.

7.6. Reference

[1] H. Kamao, M. Mandai, S. Okamoto, N. Sakai, A. Suga, S. Sugita, *et al.*, "Characterization

of Human Induced Pluripotent Stem Cell-Derived Retinal Pigment Epithelium Cell Sheets Aiming for Clinical Application," *Stem Cell Reports,* vol. 2, pp. 205-218, Feb 2014.

[2] S. D. Schwartz, J. P. Hubschman, G. Heilwell, V. Franco-Cardenas, C. K. Pan, R. M. Ostrick*, et al.*, "Embryonic stem cell trials for macular degeneration: a preliminary report," *Lancet,* vol. 379, pp. 713-720, Feb 2012.

[3] S. D. Schwartz, C. D. Regillo, B. L. Lam, D. Eliott, P. J. Rosenfeld, N. Z. Gregori*, et al.*, "Human embryonic stem cell-derived retinal pigment epithelium in patients with age-related macular degeneration and Stargardt's macular dystrophy: follow-up of two open-label phase 1/2 studies," *Lancet,* vol. 385, pp. 509-516, Feb 2015.

[4] X. Zhong, C. Gutierrez, T. Xue, C. Hampton, M. N. Vergara, L.-H. Cao*, et al.*, "Generation of three-dimensional retinal tissue with functional photoreceptors from human iPSCs," *Nature Communications,* vol. 5, p. 4047, Jun 2014.

[5] V. P. Shastri, "Non-degradable biocompatible polymers in medicine: past, present and future," *Current pharmaceutical biotechnology,* vol. 4, pp. 331-337, 2003.

[6] C. Sittel, W. F. Thumfart, C. Pototschnig, C. Wittekindt, and H. E. Eckel, "Textured polydimethylsiloxane elastomers in the human larynx: Safety and efficiency of use," *Journal of Biomedical Materials Research,* vol. 53, pp. 646-650, Dec 2000.

[7] T. W. Odom, J. C. Love, D. B. Wolfe, K. E. Paul, and G. M. Whitesides, "Improved pattern transfer in soft lithography using composite stamps," *Langmuir,* vol. 18, pp. 5314-5320, Jun 25 2002.

[8] J. S. Meyer, S. E. Howden, K. A. Wallace, A. D. Verhoeven, L. S. Wright, E. E. Capowski*, et al.*, "Optic Vesicle-like Structures Derived from Human Pluripotent Stem Cells Facilitate a Customized Approach to Retinal Disease Treatment," *Stem Cells,* vol. 29, pp. 1206-1218,

Aug 2011.

[9] M. J. Phillips, K. A. Wallace, S. J. Dickerson, M. J. Miller, A. D. Verhoeven, J. M. Martin, *et al.*, "Blood-Derived Human iPS Cells Generate Optic Vesicle-Like Structures with the Capacity to Form Retinal Laminae and Develop Synapses," *Investigative Ophthalmology & Visual Science,* vol. 53, pp. 2007-2019, Apr 2012.

[10] J. S. Meyer, R. L. Shearer, E. E. Capowski, L. S. Wright, K. A. Wallace, E. L. McMillan, *et al.*, "Modeling early retinal development with human embryonic and induced pluripotent stem cells," *Proceedings of the National Academy of Sciences of the United States of America,* vol. 106, pp. 16698-16703, Sep 29 2009.

[11] T. Furukawa, E. M. Morrow, T. S. Li, F. C. Davis, and C. L. Cepko, "Retinopathy and attenuated circadian entrainment in Crx-deficient mice," *Nature Genetics,* vol. 23, pp. 466-470, Dec 1999.

[12] M. Liu, S. Wang, and L. Jiang, "Nature-inspired superwettability systems," *Nature Reviews Materials,* vol. 2, p. natrevmats201736, 2017.

[13] H. J. Jo, H. S. Park, and M. H. Kim, "Single bubble dynamics on hydrophobic-hydrophilic mixed surfaces," *International Journal of Heat and Mass Transfer,* vol. 93, pp. 554-565, Feb 2016.

CHAPTER 8
Conclusion

In this thesis report, novel materials, designs and strategies were combined with conventional microfabrication technology to enable unusual fabrication of thin films, including thin film-based high-performance flexible and stretchable electronics, biodegradable electronics, and micro-structured scaffolds. With rapid advancements in information and health technology, conferring wearability and implantability is essential to enhance diverse types of scientific and technological applications. This allows conformal contact to surfaces with complex curvilinear topography and texture, like our skin and organs, offering biomedical engineering in the most non-invasive manner. On the electronics field, flexible and stretchable electronics have developed tremendously over the past decade. Especially, the performances have improved to reach those of state-of-the-art electronics; however, the development of high-frequency components, circuits and systems is still in its early stage as presented in Chapters 2 to 4. Promising enhancements led to achieve high-frequency flexible and stretchable electronics by utilizing various classes of materials. Another potential challenge expected as the electronics industry continues to develop is the demand of higher frequency operation. The restrictions in the number of bandwidths in wireless communication frequencies and bandwidth caps due to heavy usages make wireless service providers to demand even higher frequency operations. Only a handful of frequency bands are approved by the Federal Communications Commission (FCC) to be used in biomedical applications, in which the flexible and stretchable electronics are the most advantageous. Eventually, flexible and stretchable microwave electronics will be required to operate at extremely high-frequencies (EHF). Since high-speed devices consume much less power when operating well

below their f_T and f_{max}, devices with higher frequency responses are greatly desired. Such operation would not only enhance operation time in battery powered devices, but also generate less heat. These unfortunate facts pose additional challenges for high-frequency electronics engineers, requiring further improvements in device performance. Nevertheless, there is still plenty of room for performance improvements using novel materials and it will not be long before we can fully utilize the excellent electrical properties intrinsic to the materials. In addition to performance enhancement, other concerns that rise in these mechanically flexible electronics include the varying performance due to bending and stretching. This is especially crucial for high-speed electronics, where a slight variation in frequency response can alter the matching of an entire circuit. Thus, methods to minimize this variance by reducing the modulus mechanics applied to the devices and circuits should simultaneously be developed, in order to use them in practical applications. Being more convenient, accurate and safe, than existing bioelectronics, there is no doubt that next generation biomedical devices will be in conformal format.

In Chapters 5 and 6, the feasibility of green chip concept utilizing thin-film inorganic semiconductors, metals and insulators on biodegradable substrates are reviewed and demonstrated. Using wood derived cellulose nanofiber (CNF) as the substrate, high-performance electronic devices for both microwave and digital applications were fabricated in the same manner the flexible and stretchable electronics were fabricated. Electrical analysis on the CNF film used for the study showed that the film has suitable characteristics as substrates for high-performance electronics, in terms of thermal, mechanical and electrical properties. High-performance transistors and diodes using GaAs that have superior microwave-frequency operation were readily demonstrated on the CNF film, followed by Si-based logic devices for digital computing. Great amount of semiconductor materials could be saved by re-using the growth substrate after release.

With rapid technological advances leading to significant decrease in the lifetime of consumer electronics, such green chip technology with high-performance would be ideal replacement for future electronic chips where non-renewable resources are consumed.

For decades, numerous strategies have been proposed to create elastic devices in all fields, including soft robotics, stretchable electronics, scaffolds, drug delivery systems, and rehabilitation devices. In Chapter 7, it was shown that advanced microfabrication tools can be utilized for patterning complex micro-structures on elastomers. Whereas the scaffold introduced in Chapter 7 only consisted of the elastomer to guide the growth of photoreceptor cells, the methods and strategies presented in this thesis overall should allow the integration of thin film electronic components on the scaffold for further interesting studies. This would tremendously expand the applications of the scaffold; for instance, the cell growth behavior when electric fields are applied through attached electrodes could be completely different than without the electric fields. We can also print thin film electrodes or photodetectors on the scaffold to perform as various sensors after transplantation. As such, there are many encouraging future work to be tried by combining thin film elastomers and electronic devices.

Only a few of such research progresses have made commercial impact. The most critical drawback of thin film devices in flexible or stretchable format is durability and reproducibility, as thin films are fragile and difficult to replicate. New tools specifically designed for thin film microfabrication are essential to surmount such drawbacks, but microfabrication tools are often time-consuming and cost-intensive to develop. To accelerate time towards commercialization, not only new strategies should be focused on, but also the industrial equipment for producing the devices should be developed for mass production. Nevertheless, big players in the industries are investing billions of dollars in to this area. For instance, Google Inc. has announced a wireless

contact lens that can monitor diabetes by sensing the glucose level of the tears. Although it is not fully comprised of thin film components (a tiny rigid chip is attached for electronic circuits), the smart contact lens also utilizes circular shape wireless antenna, which transmits clinical data to a mobile device for continuous monitoring. The lens has a tiny hole to allow tear to be collected by the system and with ultra-miniaturized integrated circuit-based wireless controller chip connected to the sensor, the contact lens is able to read glucose level every one second. It seems that the technology of such kind is already mature enough to be commercialized; but in order for this smart lens to be get access to market, it must go through rigorous reviews, tests, and surveys, to be proven for safety. As such, there are more steps on these research-to-product process, before we complete this paradigm shift of converting electronics and biomedical implants/transplants from rigid to flexible/stretchable formats. Once these steps are completed, we should start seeing them in local pharmacies and hospitals in the near future.